# Constant temperature hot wire anemometry applied to the characterisation of a nozzle molecular beam source

Thesis submitted for the degree of Master of Philosophy
of the Australian National University

Benjamin Robert Powell

April 24, 2008

This thesis does not contain material previously submitted for academic assessment. To the best of my knowledge it contains my own work except where appropriate reference is made in the text.

Benjamin Robert Powell

April 24, 2008

**Abstract**

This thesis presents the hardware, software, and analysis involved in the development of a low density molecular beam source for the future investigation of high temperature, magnetically confined plasmas. The plasmas to be studied are produced as part of the ongoing H-1 stellarator at the Australian National University. The molecular beam source was characterised in a test tank to determine the flow rate, average velocity, and the flow density profile for a range of plenum pressure and piezo drive voltage configurations.

A constant temperature hot wire anemometer instrument using lamp filaments for probes was applied to diagnose the molecular beam. Data from test tank experiments was collected through an automated experiment controlled by a Labview program interfacing with a National Instruments DAQ system. The ensuing 60 gigabytes of data was stored in a dedicated MDSplus database and analysed using routines written in IDL. The stored data was sufficient to establish the required properties of the molecular beam and of the anemometer sensor. The beam angular density profile for a range of beam source parameters has been comprehensively characterised and the molecular beam source subsequently installed on H-1.

Early results show that the low density molecular beam is an effective means of modulating at 1kHz the light emitted from a localised region of a magnetically confined plasma.

# Acknowledgements

I thank my supervisor, Professor John Howard, for all the help, patience and freedom he provided me throughout my research. I also thank my adviser, Dr. Boyd Blackwell, for his help, patience, and advice about noise. I thank Scott Collis for his work designing the molecular beam system and for his help during my work. I thank S. A. Santhosh Kumar for his patience in considering my many, often-incomplete ideas. I thank David Oliver for his help with plasma physics and level-headed perspective. I thank David Pretty and Dr. Fenton Glass for keeping my LINUX system operating at its best and opening my eyes to a superior operating system. I thank Dr. Horst Punzmann for demonstrating to me exceptional rigour in conducting plasma research, and for highlighting to me the potential risk of approaching problems from outside the officially recognised context. I thank Professor Jeff Harris for providing access to the encyclopaedia of plasma facts which he carries in his head. I thank Dr. Matthew Hole for providing me a close-quarters demonstration of the finer points of lobbying governments for financial support. I thank Dr. Michael Shats for allowing me to attend his plasma physics course and for presenting the challenges facing fusion researchers from a turbulence perspective. I thank Dr. Frank Houwing for showing me the T3 shock tunnel and introducing me to members of the International Shockwave Institute. I thank John Wach for helping beyond the call of duty

with the design, construction, and cataloguing of the hardware required for my experiments. I thank all the technical staff involved in the mechanical and electronic fabrication of the various elements of the project. I thank the administration staff for doing a wonderful job dealing with people like me. I thank the cleaners for removing my waste. Everyone named has, at some point, provided me with valuable interactions which have left me wiser. I would finally like to thank my soon-to-not-be wife, Holly Williamson. Holly endured more physics than she ever hoped for, and did so with considerable albeit finite resilience and grace. I thank my parents for keeping me alive and for their continuing patience with my meandering and housing the considerable bulk of experimental apparatus I have rescued from the bins of various scientific institutions. Without this equipment, it would be impossible to continue the more creative aspects of my research unfunded. I thank the agencies of funding that allow research such as this to continue. Every dollar spent developing nuclear fusion technology is an investment toward the energy salvation of humanity. Finally, I hope the ridiculously unrealistic constraints of Occupational Health and Safety policy regarding experiment prototyping and direct access to workshops does not continue to succeed in preventing creative and novel research by students at the ANU in future.

# Contents

# Chapter 1

# Introduction

## 1.1 Thesis overview

This document details the modification of the supersonic fuelling system on the H-1 experiment. The existing converging-diverging nozzle with a 0.35mm throat diameter was replaced with a converging-diverging nozzle with a 0.19mm throat diameter. The molecular beam from the new nozzle was then characterised in a test tank using constant temperature hot wire anemometry. Average velocity was established by considering phase changes in the modulated beam with distance. The beams density profile was established by calibrating the anemometer signals to particles lost from the plenum of the delivery system. A range of plenum pressure and piezo drive voltage configurations were explored and characterised. Due to the low beam flux, a number of modifications to the approach previously used for characterisation of the fuelling molecular beam source had to be developed. The end result of this characterisation is the ability to generate detailed time- and space-resolved beam densities based on measurements from a single anemometer wire. A sample of the detail achieved is seen in figure 1.1. Shown is an example the information available in the output data files.

This chapter contains a brief summary of the rationale for nuclear fusion research. The context of the H-1 experiment in the development of technology relevant to nuclear fusion is summarised. My research is then discussed.

Chapter 2 presents a theoretical consideration of the diagnostic molecular beam. The development and implementation of the computer control and data acquisition system is described. A description of the molecular beam source and associated hardware is given. The anemometer instrument used to characterise the beam is described.

Chapter 3 details the calibration of the anemometer instrument and the analysis of experimental data.

Chapter 4 summarises results and concludes the results of the thesis.

Included as appendices is a detailed description of the use of output data files summarising the characterisation, a brief explanation of the Labview program controlling the beam source hardware, and a description of the method used to measure the H-1 plenum volume.

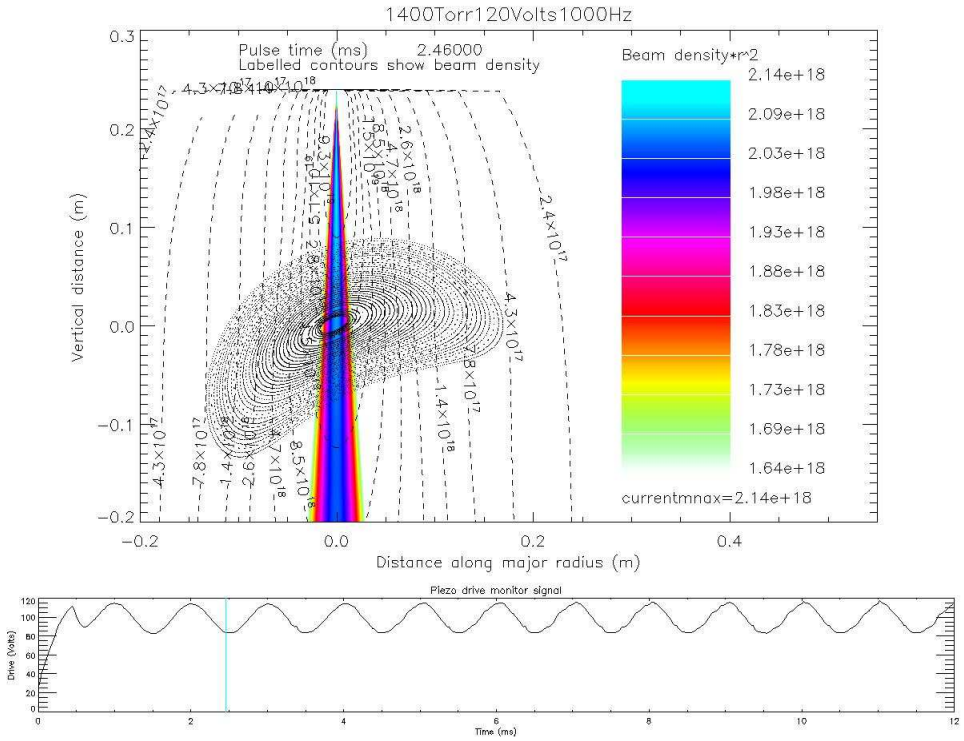


Figure 1.1: The upper plot is an example characterised beam properties for a molecular beam with plenum pressure of 1400 Torr, drive of 120 Volts, 1KHz modulation, 2.46ms into the pulse. The derivation of this plot is described in chapters 2 and 3 of this work. The lower plot shows the piezo valve drive monitor signal that will be used to time reference the beam on the H-1 experiment.

## 1.2 Nuclear fusion

Fossil fuels provide a ready source of energy for those who can afford them. As the finite reserves of these fuels decrease, the cost of energy will rise. Greenhouse gas emissions from fossil fuels also change the chemical composition of the atmosphere. The precise effect of this change on global climate is difficult to predict. Further, the possibility of consequent climate change implies an onerous responsibility for the nations that continue to pollute the atmosphere.

A non-polluting and abundant source of energy would alleviate the risk of future climatic and economic crises. In theory, nuclear power can achieve this goal, although to date only power plants relying on nuclear fission have been developed. Nuclear fission involves chain reactions of unstable and heavy nuclei, such as uranium-235. These reactions produce long-lived radioactive waste products, which pose a non-atmospheric pollution concern. The fuel and waste can be readily used to make nuclear weapons, making the fuel supply and waste disposal for nuclear fission power generation a considerable security concern. Nuclear fission is not the only type of nuclear reaction that could be used as an energy source. Instead, nuclear fusion, the reaction which heats the sun, may be a viable alternative.

Nuclear fusion (joining nuclei) is a fundamentally different process to nuclear fission (splitting nuclei). Due to technological challenges which remain unsolved to date, nuclear fusion power is not currently used. The difficulty experienced in initiating sustained nuclear fusion highlights a valuable characteristic of nuclear fusion power - the reaction can be stopped very easily. This means there will be no risk

of meltdown in a fusion power plant, as compared to a fission plant where risk of meltdown is relatively high. Further, as the fuels for nuclear fusion reactions are currently freely available, the security risk is low. The waste product is helium, which is not hazardous and is lost to space from the Earth's atmosphere, therefore causing little environmental concern.

The most obvious example of energy released from nuclear fusion reactions is the sun. Gravitational forces in the sun are strong enough cause trapped nuclei to fuse. Energy released from fusion reactions heat the sun, and in turn this thermal energy is radiated as light. Electromagnetic energy from the sun is the primary energy source for the biosphere of the earth.

On the Earth, nuclear fusion reactions cannot be initiated by gravity as they are in the sun. Many alternative approaches have been demonstrated to achieve controlled nuclear fusion without using gravity. To date, one of the most researched technologies for sustained and efficient nuclear fusion power relies upon magnetic plasma confinement.

## 1.3 Magnetically confined fusion plasmas

Nuclear fusion reactions do not occur on Earth due to the electrostatic repulsion that occurs between colliding nuclei. One way to overcome this is to increase the kinetic energy of the nuclei involved in collisions. This equates to increasing the

temperature of the nuclei. The easiest fusion reaction to initiate involves deuterium and tritium and requires temperatures above 5keV (58,000,000 degrees Celsius) for appreciable fusion rates to occur [5].

At temperatures this high, matter is in the plasma state. This is where collisions involving atoms are so energetic that electrons are knocked out of their atomic orbits. This results in a sea of free electrons and charged ions. To keep the plasma hot, it must be kept away from solid (and therefore colder) materials, such as the walls of a power plant. Magnetic plasma confinement exploits the fact that a charged particle moving in a magnetic field experiences a force perpendicular to both the field and the particle's motion. The 3-dimensional trajectory of a charged particle is a helix with axis aligned to the local magnetic field.

By creating a strong magnetic field parallel to the reactor walls, it is possible to reduce the plasma's interaction with the walls and achieve high plasma temperatures. To achieve even higher plasma temperatures, relevant to nuclear fusion reactions, it is also necessary to slow the drift of charged particle orbits across magnetic field lines towards the walls. The axis of charged particle orbits will drift across magnetic field lines as a result of variations in the magnetic field, collisions with other plasma particles, and a variety of electromagnetic forces.

Toroidal magnetic geometries were proposed as early as 1946 as a way to achieve high temperature plasma confinement for nuclear fusion [6]. The approach of G.P. Thomson [6] was to use a magnetic field resulting solely from currents inside the

plasma. Following this, improved confinement was achieved by using currents external to the plasma, along with internal plasma currents, to generate the confining magnetic field. An example of this type of device is the tokamak. The internal plasma currents are necessary to reduce the drift of charged particle orbits in a tokamak by twisting the magnetic field lines. Perturbing the internal currents may significantly degrade the magnetic confinement of the plasma. In a tokamak, variations in internal plasma current are responsible for a significant amount of the plasma drift towards the walls [7]. The negative confinement characteristics of instabilities from internal currents are offset by magnetic configuration design simplicity, as well as the advantage of ohmic heating of the plasma provided by the toroidal current. This makes the tokamak the design of choice for the proposed multi-billion dollar International Thermonuclear Experimental Reactor.

Magnetic confinement that does not require currents inside the plasma is possible. The stellarator proposed in 1951 by L. Spitzer [8] is an example of this. As plasma currents are not induced, heating in a stellarator is more difficult than in a tokamak. However, the strength of these devices is that magnetic structures are more predictable and better controlled. The predictability of magnetic structures allows systematic investigation of the interplay between high-temperature plasma instabilities and magnetic field geometry without complication from internal current-driven instabilities.

## 1.4 The ANU H-1 Heliac experiment

The H-1 Heliac stellarator permits the study of high-temperature, current-free plasmas in a flexible magnetic field geometry [12]. The top view of the H-1 Heliac is shown in figure 1.2. The top cover and some internal fixtures are removed to show the relative position of the plasma (shown in red). H-1 uses only external coils to generate the confining magnetic field structure, and allows the study of plasma energy and particle transport for a wide range of controlled magnetic field configurations. Research to understand the physics of current-free heating techniques is also possible. H-1 provides the opportunity to develop novel plasma diagnostic tools that can be used for any high-temperature plasma. H-1 is capable of achieving temperatures in excess of 100eV (around 1,000,000 degrees Celsius).

In the absence of drift processes, the plasma particle trajectories in H-1 are confined to magnetic flux surfaces. They form a set of nested surfaces [13]. The poloidal cross-sections of these surfaces at the molecular beam source installation port are shown in figure 1.3. The outermost flux surface is called the *last closed flux surface*. Complete flux surfaces do not exist outside the last closed flux surface.

Plasma heating in H-1 is achieved by injecting electromagnetic waves at two frequencies that couple to plasma particle motions. The two frequencies are supplied by systems named *Ion Cyclotron Resonant Heating* or ICRH (at around 7MHz) and *Electron Cyclotron Resonant Heating* or ECRH (at around 28GHz). The terminology of ICRH is misleading in the case of H-1 because heating does not occur solely as a result of ion cyclotron resonances [14], and some electron heating occurs. ECRH

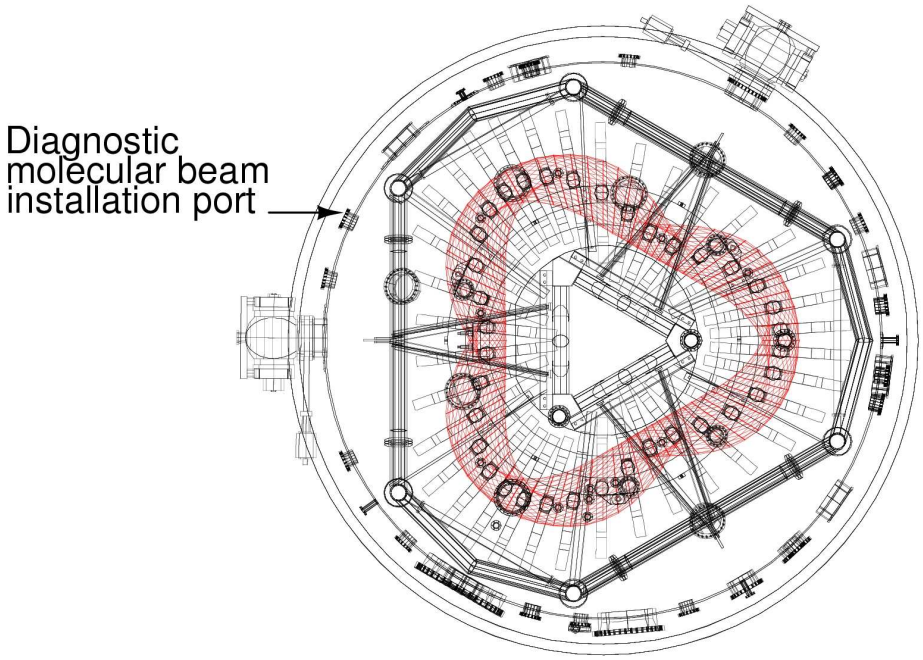


Figure 1.2: Top view of the H-1 Heliac with the top cover and some internal fixtures removed to show the relative position of the plasma (shown in red). The diameter of the vacuum vessel is 3.9 meters. Image courtesy of John Wach.

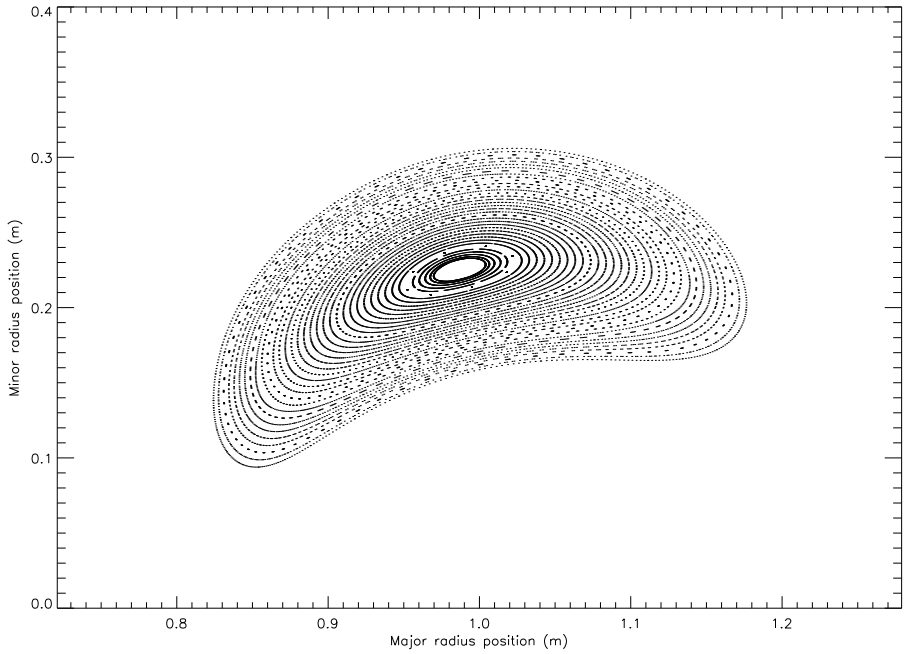


Figure 1.3: The poloidal cross-section of flux surfaces at the position of the molecular beam source for the standard magnetic field configuration. Data courtesy of S. A. Santhosh Kumar

heats the electrons more specifically through their cyclotron resonances [15]. In H-1 free electrons are generated by ICRH so that the ECRH can couple power to cyclotron motions.

A better understanding of how the plasma is heated and how instabilities cool the plasma requires parametrisation of the plasma. Ideally, key plasma properties are measured on flux surfaces and include electron temperature, electron density, ion temperature and ion density. At high plasma temperatures, diagnostic tools relying upon solid probes inserted into the plasma cannot be used. This is because they are damaged by high temperature particles and they significantly interfere with the parameters they are attempting to measure.

## 1.5 The need for a diagnostic molecular beam

Light emitted from an injected collimated and flux calibrated molecular beam source can be used for a number of spectroscopic and other plasma diagnostic applications. For example, the beam can inject helium into the plasma for helium-I line intensity ratio measurements of electron density and electron temperature [9] [10]. By using a low density helium beam, the plasma cooling due to increased radiation is confined to the region being spectrally analysed. A low density beam is required to minimise the perturbation of the plasma parameters being measured. Achieving the same spectral intensity with a non-localised helium density would perturb the plasma more, as the radiative heat loss occurs throughout the plasma volume.

Spectroscopy involves careful analysis of the frequency spectrum of light emitted by the plasma. Information can be obtained from spectroscopic studies to help determine diverse plasma parameters, such as the types of ions present, as well as their temperature, velocity, and density. For spectroscopy to be effective, sufficient light needs to be emitted from the plasma for analysis. High temperature hydrogen plasmas emit very little light, as ions are stripped of electrons. In order to emit a photon the ions must capture an electron or undergo charge exchange in a collision. By introducing helium into the plasma, spectral line radiation is retained at much higher plasma temperatures, as metastable electron states of higher energy are possible.

The use of a modulated molecular beam source also permits the perturbative study of plasma transport mechanisms [11]. By modulating the beam flux, periodic density and temperature variations can be generated in the plasma. The time evolution of these perturbations can be related to energy and particle transport processes across the magnetic flux surfaces.

Microwave interferometry can accurately determine variations in the electron density of the plasma. From the phase difference between microwaves passing through the plasma, and microwaves passing through a reference path with no plasma, the electron density in the plasma path is found. Electrons in the plasma advance the phase of the propagating microwave. Changes in phase delay indicate changes in electron density [5]. The power of the microwave beams used to probe the plasma is

typically 10-100mW. This makes any plasma perturbation caused by heating with the probe beam negligible when compared with the the ICRH and ECRH systems, each of which deliver hundreds of kilowatts of power.

To enhance the effectiveness of both these diagnostic uses of the molecular beam source, the fuelling molecular beam source on H-1 was modified to improve modulation capabilities and reduce the beam density. My research involved the set-up and characterisation of the diagnostic molecular beam source for use in plasma studies on H-1.

Similar work developing nozzle-based gas injection to diagnose high temperature, magnetically confined plasma has been conducted by V. A. Soukhanovskii *et. al.* [2] on the National Spherical Torus Experiment at the Princeton Plasma Physics Laboratory. The H-1 diagnostic molecular beam has a smaller throat diameter and a carefully characterised response to valve modulation.

# Chapter 2

# The diagnostic molecular beam

## 2.1 Basic theory

### 2.1.1 Nozzle flow

The molecular beam source consists of a converging-diverging nozzle assembly that replaces the valve seat in a modified Veeco PV-10 leak valve. The design is identical to that developed by Scott Collis [1] for molecular beam plasma fuelling, except for the dimension of the converging-diverging nozzle throat diameter. This modification was carried out in response to concerns that the flux from the fuelling nozzle was perturbing plasma conditions to such an extent that it was unsuitable for diagnostic use. By installing a nozzle with a smaller throat diameter (0.19mm), the mass flow through the nozzle was reduced, thereby diminishing the perturbation to the plasma. A sectioned view of the molecular beam source is shown in figure 2.1.

In this chapter, mathematical notation will be used such that the subscript 0 represents conditions in the plenum, superscript # represents conditions at the nozzle throat, and flow parameters without a subscript or superscript represent exit conditions of the nozzle.

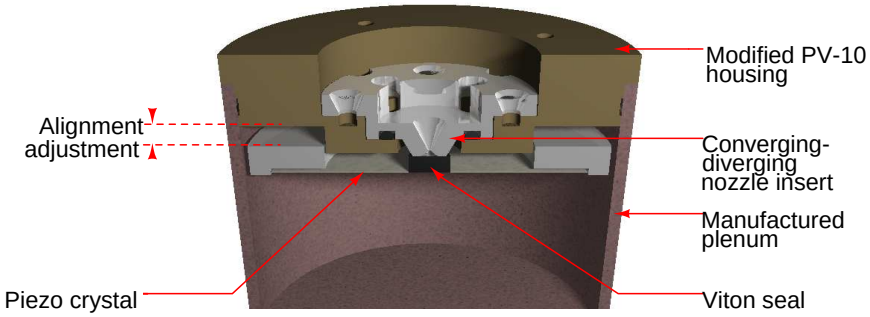


Figure 2.1: A sectioned view of the molecular beam source. The modified Veeco PV-10 valve housing is shown with the converging-diverging nozzle insert installed. The inlet to the nozzle forms the new valve seat for the viton seal. The position of the piezo crystal and viton seal is governed by three mounting screws at 120 degree intervals around the outside of the piezo crystal. These screws change the alignment dimension indicated. The plenum was manufactured to replace the original PV-10 valve cover. Image courtesy of Scott Collis.

The flow through the nozzle can be approximated using the governing equations of isentropic quasi-1-dimensional flow in a converging-diverging duct [3]. This serves as a theoretical approximation of ideal conditions as effects of irreversible processes are ignored. Flow through the nozzle in this case is independent of the pressure in the vessel into which the nozzle exhausts if the exit pressure is sufficiently low to allow sonic choking to occur in the throat. For pressures typical of the test tank, and H-1, sonic choking will occur. Sonic choking is a situation where the compressibility of the flow limits velocity in the converging part of the nozzle. When a nozzle is sonically choked at the throat, analysis of the flow through the nozzle is significantly simplified. The flow only depends on the throat area $A^{\#}$ and the conditions in the plenum.

The gas density in the plenum $\rho_0$ is determined using the plenum pressure $p_0$ and plenum temperature $T_0$ by:

$$\rho_0 = \frac{p_0}{RT_0} \tag{2.1}$$

where R is the engineering gas constant. For helium, this is a constant of 2076.8 $J/kg.K$ [19]. $p_0$ is in Pascals. For conversion, 1 Torr=133.3 Pa. The flow density at the nozzle throat $\rho^{\#}$ can be determined from the plenum density using:

$$\frac{\rho^{\#}}{\rho_0} = \left(\frac{2}{\gamma+1}\right)^{\frac{(1)}{(\gamma-1)}} \tag{2.2}$$

where $\gamma$ is the adiabatic exponent and is a constant dependent on the gas used. For helium $\gamma = \frac{5}{3}$. The temperature of the flow in the throat $T^{\#}$ is given by:

$$\frac{T^{\#}}{T_0} = \frac{2}{\gamma+1} \tag{2.3}$$

The Mach number at the throat of a sonically choked nozzle is 1. The flow speed is then equal to the speed of sound in the throat $a^{\#}$ given by:

$$a^{\#} = \sqrt{\gamma R T^{\#}} \tag{2.4}$$

Mass flow through the nozzle $\dot{m}$ in $kg/s$ is:

$$\dot{m} = \rho^{\#} A^{\#} a^{\#} \tag{2.5}$$

To convert kilograms per second to particles per second, $\dot{m}$ must be divided by the mass of a helium atom in kilograms. The mass of a helium atom is approximately $6.65 \times 10^{-27}$kg.

The flow through the nozzle can be estimated based upon the assumptions of isentropic quasi-1-dimensional flow in the converging section of the nozzle, and the flow

being sonically choked at the throat. In practice, a number of physical processes reduce flow through the nozzle. The design of the nozzle is not ideal for hypersonic flows as the diverging angle of 23.4° is well in excess of the typical limit of 7.5° to avoid boundary layer separation in the nozzle. The sharp transition at the throat may also result in boundary layer separation there and produce a vena contractor effect. Heat transfer and friction between the nozzle walls and the flow will result in departure from the isentropic conditions reducing flow. The nozzle throat had a tolerance of 2.5%. A reduction in the nominal throat diameter by this amount changes predicted mass flow through the nozzle by 5%. Figure 2.2 presents the nozzle flow for the ideal isentropic quasi-1-dimensional case for three values of $T_0$ and shows the experimentally determined flow at 293K for comparison. The departure of the experiment from the theoretical analysis is shown to be around 9%.

In the molecular beam source, the nozzle flow can be controlled by changing either the plenum pressure or the voltage driving the piezo valve. The interaction between the viton seal and the nozzle valve seat acts as a resistance to flow, which varies with the voltage applied to the valve. Increasing the resistance to flow into the inlet of the nozzle will reduce the nozzle inlet pressure in comparison to that of the plenum. It will also increase the temperature of the flow entering the nozzle. Measuring unknown parameters like the nozzle inlet temperature and pressure downstream of the viton seal, while the valve is operating, presents a considerable unsolved technological challenge. Therefore the physical properties of the molecular beam with a range of plenum pressures and valve drive voltages are explored empirically in this thesis.

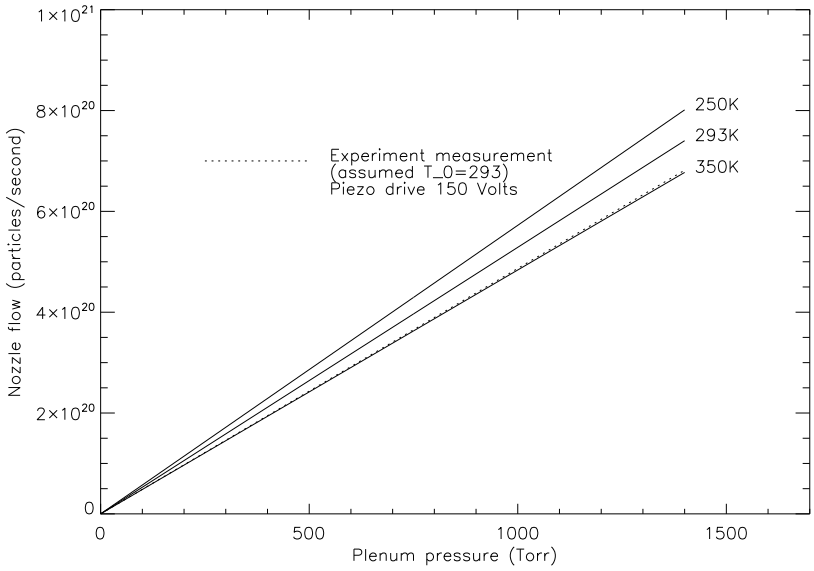


Figure 2.2: The isentropic quasi-1-dimensional prediction of flow through the nozzle for plenum temperatures of 250K, 293K and 350K. For comparison the dashed line shows flow through the nozzle measured by experiment for a plenum gas temperature of 293K with a piezo drive of 150 Volts.

### 2.1.2 Exit velocity

The exit velocity of particles through the converging-diverging nozzle can also be predicted if isentropic quasi-1-dimensional flow is assumed. The relationship between the nozzle throat area $A^{\#}$, the nozzle exit area $A$, and the exit Mach number $M$ is as follows:

$$\left(\frac{A}{A^{\#}}\right)^2 = \frac{1}{M^2}\left[\frac{2}{\gamma+1}\left(1+\frac{\gamma-1}{2}M^2\right)\right]^{\frac{(\gamma+1)}{(\gamma-1)}} \tag{2.6}$$

M is found by numerical inversion of equation 2.6 where A and $A^{\#}$ are determined by the shape of the nozzle. The exit Mach number can then be converted into an

exit velocity $v$ after determining the exit temperature $T$. This is done by evaluating:

$$T = T_0 \left(1 + \frac{\gamma - 1}{2} M^2\right)^{-1} \tag{2.7}$$

$$v = M\sqrt{\gamma RT} \tag{2.8}$$

The nozzle has a throat diameter of 0.19mm and an exit diameter of 4.0mm. The diverging section has a length of 4.4mm. The wall of the diverging section is at an angle of 23.4° to the beam axis. A schematic presentation of these dimensions is shown in figure 2.3. Using these dimensions and assuming isentropic quasi-1-dimensional flow, the flow velocity in the nozzle can be calculated. The cross-sectional area of the nozzle some distance from the throat is defined as the effective exit area $A_{eff}$. By replacing A in equation 2.6 with $A_{eff}$ a velocity profile is established. $A_{eff}$ is determined using the distance from the throat d along the nozzle axis, as the diverging part of the nozzle is conical. $A_{eff}$ is then:

$$A_{eff} = \pi((d + 0.22)\tan(23.4°))^2 \tag{2.9}$$

The theoretical flow velocity profile in the diverging section of the nozzle can then be calculated as shown in figure 2.4.The exit velocity in the ideal case is predicted to be 1742m/s. In reality the velocity will be less due to non ideal processes in the nozzle like momentum transfer between the boundary layer and the nozzle wall. The beam velocity will be determined by modulating mass flow and measuring the change in anemometer signal phase with displacement from the source.

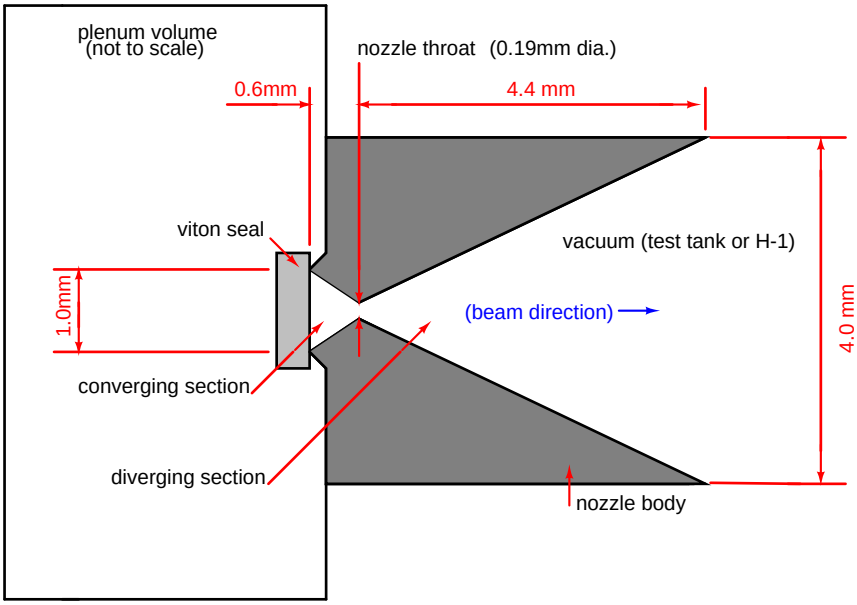


Figure 2.3: A schematic presentation of the important nozzle dimensions.

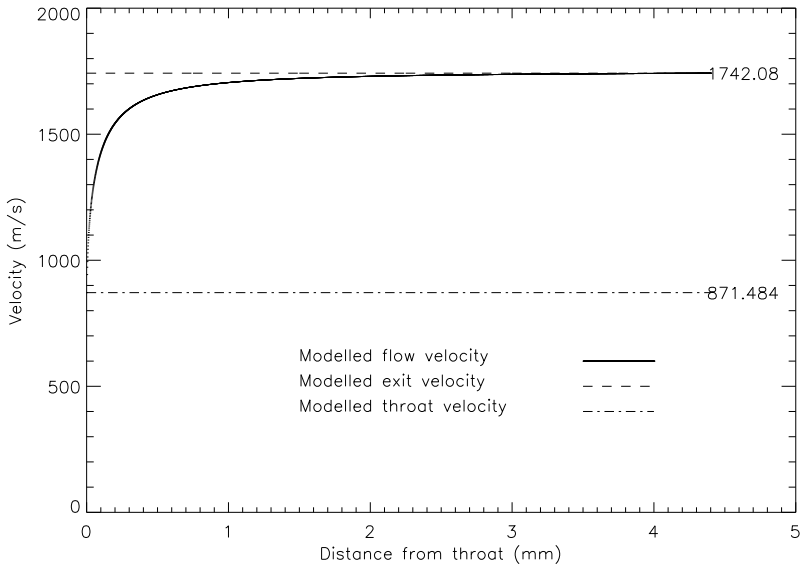


Figure 2.4: Theoretical prediction of nozzle flow velocity based on isentropic quasi-1-dimensional assumptions. Throat velocity and theoretical exit velocity are also shown. In this plot an effective exit area based on the distance from the throat is used to establish the velocity profile along the diverging section of the nozzle.

### 2.1.3 Beam density profile

In discussing beam density all references relate to the number of particles (specifically helium atoms) per unit volume rather than the more conventional sense of mass per unit volume. In an ideal converging diverging nozzle the expected beam density profile is uniform with edges approximated by a hypersonic continuum flow's ability to turn as it exits the nozzle. To determine this boundary the Prandtl-Meyer function $\nu(\mathrm{M})$ is evaluated at the exit, then the difference between the maximum Prandtl-Myer function value $\nu_{\max}$ and $\nu(\mathrm{M})$ gives the maximum angle the flow can turn isentropically[24]. The Prandtl-Meyer functions are:

$$\nu(\mathrm{M}) = \sqrt{\frac{\gamma+1}{\gamma-1}}\tan^{-1}\left(\sqrt{\frac{\gamma-1}{\gamma+1}(\mathrm{M}^2-1)}\right) - \tan^{-1}\left(\sqrt{(\mathrm{M}^2-1)}\right) \tag{2.10}$$

$$\nu_{max} = \frac{\pi}{2}\left(\sqrt{\frac{\gamma+1}{\gamma-1}}-1\right) \tag{2.11}$$

For helium $\nu_{\max} = 90°$. From equation 2.6 the exit mach number M is found to be approximately 19 giving $\nu(\mathrm{M}) = 81°$. It is therefore reasonable to assume the flow does not bend more than 9° on leaving the nozzle. As the angle of the diverging nozzle section is approximately 23° the ideal beam can be bounded by an angle of 32° from the centerline referenced to the nozzle throat.

Using hot-wire anemometry the beam density profile was found to be centrally peaked. The specific mechanism for this could not be determined. It is likely though that the sharp throat transition and large diverging angle contribute in some way to non-ideal behavior. Professor Beric W. Skews, in an informal discussion at the Third International Symposium of Interdisciplinary Shock Wave Research, suggested that the non-ideal nozzle shape will likely result in shock waves in the diverging part of

the nozzle. Unfortunately the complexity of the physical situation prevents further refinement of this hypothesis beyond the suggestion that the position of these shocks could be responsible for the observed variations in the molecular beam angle with changing plenum pressure. The data presented on page 45 shows anomalous signals that may be a result of time-varying shocks in the diverging part of the nozzle. The 230 Hz oscillation observed by the middle anemometer probe has a phase dependent on angular displacement of the anemometer array about the beam axis and is of unknown origin. An untested hypothesis is that the anomalous oscillation is caused by time-varying shocks occurring in the diverging part of the nozzle. The oscillation is observed in many shots. Further experiments on H-1 are required in order to determine if the oscillation is a real property of the beam. The signal may be an artifact of the test tank hardware.

## 2.2 Setup of the molecular beam source

To control flow through the nozzle, the piezo element and modified housing from a PV-10 leak valve was used. In order to accommodate the converging-diverging nozzle, the original PV-10 valve seat was machined out to allow the insertion of the nozzle assembly. The inlet end of the nozzle was prepared as a valve seat for the original viton seal mounted centrally on the circular piezo crystal disk. Upon applying a voltage to the piezo crystal, it deforms and lifts the viton seal from the nozzle valve seat. Increasing the drive voltage on the piezo valve causes the viton seal to lift further from the valve seat.

After modifying the PV-10 valve body, the position of the valve seat was different to the original configuration. As a consequence of the modification, the viton seal required re-alignment with the valve seat. Three alignment screws adjust the plane of the viton seal face. Documentation was not available regarding the workshop alignment of the viton seal, which led me to devise an alignment procedure using the electrical properties of the piezo crystal. Contact between the viton seal and the valve seat can be detected as a voltage step measured across the crystal, with its polarity dependent on the direction of crystal displacement. Oscillations indicate a vibration rather than contact with the valve seat.

Crucial to obtaining correct alignment was adjusting the plane of the viton seal to coincide with the plane of the valve seat. In order to achieve this, each mounting screw was tightened until contact with the valve seat was detected and then the alignment screw was backed off. This process was reiterated with decreasing displacement sizes until a small similar displacement of each of the mounting screws resulted in a similar voltage step. Each of the mounting screws were then tightened a quarter of a turn to ensure the valve sealed reliably with no drive voltage.

The original specifications of the PV-10 valve indicated a maximum drive potential difference of 100 Volts DC to be used. After alignment, the valve was found to deliver approximately 85% of its peak flow, with a driving potential difference of 100 Volts. For a performance comparison, the fuelling molecular beam - which had not been aligned by this method - was yet to open at 100 volts, as seen in figure 2.6.

The nozzle flows shown in figure 2.5 and 2.6 were calculated based upon plenum pressure changes, as discussed later in chapter 3.

In order to enhance the system response to a modulated signal, a high voltage amplifier with a fast rise time was constructed to drive the piezo element. This, in conjunction with alignment of the viton seal, has allowed the maximum modulation frequency to be increased from around 250 Hz in the fuelling nozzle to 1200 Hz in the diagnostic nozzle. Above 1200 Hz the visibility of flow modulation decreases markedly. To achieve good flow modulation at these frequencies, drive voltages well in excess of the maximum specified in the PV-10 operating guide are required. Consequently the piezo element may be damaged.

## 2.3 Computer interface

The control software was written with the aim of automating the experiment to allow large amounts of data to be acquired and stored with little effort. By doing this, statistical noise reduction was possible in the analysis of data. An MDSplus database [18] was set up to manage experimental data for the nozzle characterisation. The data was saved as a series of shots with information stored in a tree structure. The settings for each shot were read from a spreadsheet file. This spreadsheet also provided a detailed log of the experimental conditions for use during later analysis. In the analysis software, error handling algorithms were included to avoid using unreliable data.

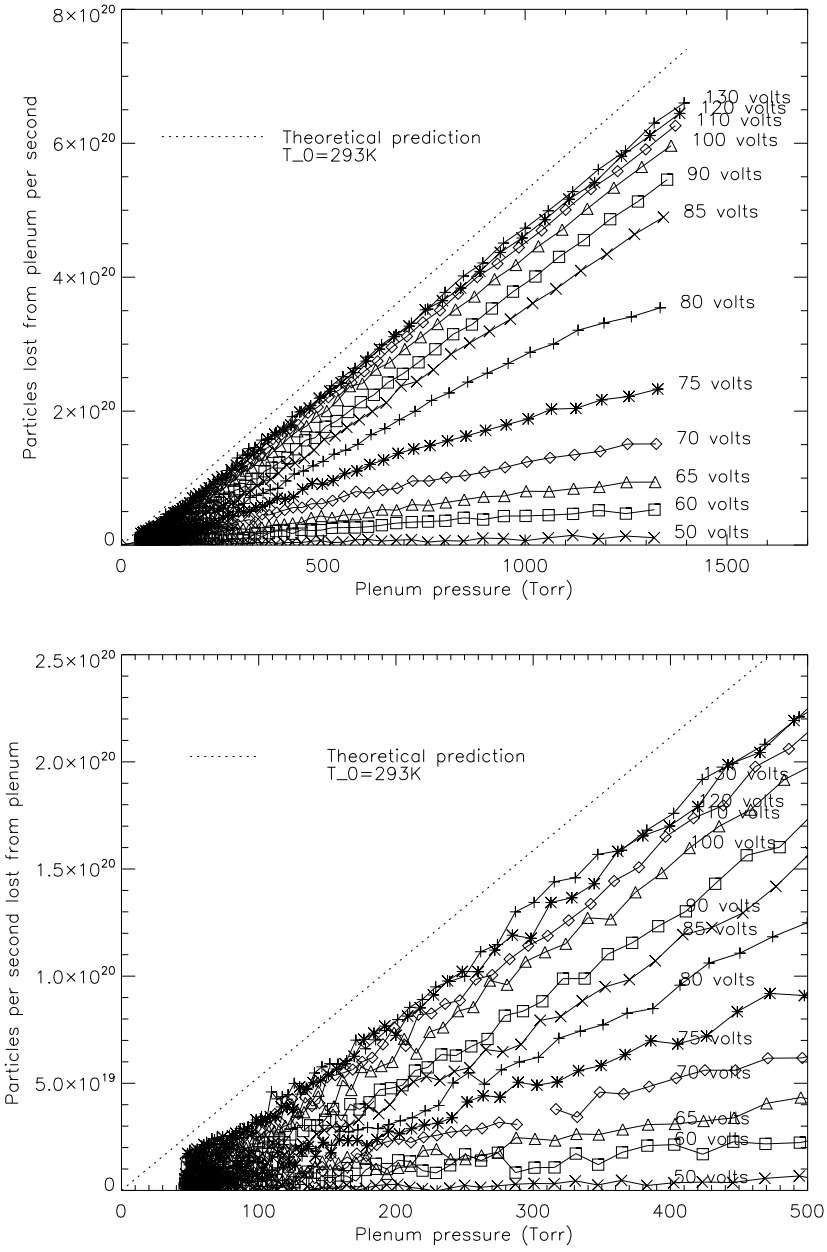


Figure 2.5: Diagnostic nozzle flow for 100ms pulses of varying voltages for a single scan through the pressure range. The upper plot shows the flow for 100ms pulses of varying voltages for high range plenum pressure values and the lower plot shows an expansion of the nozzle flows for low plenum pressures. The data was recorded in the test tank.

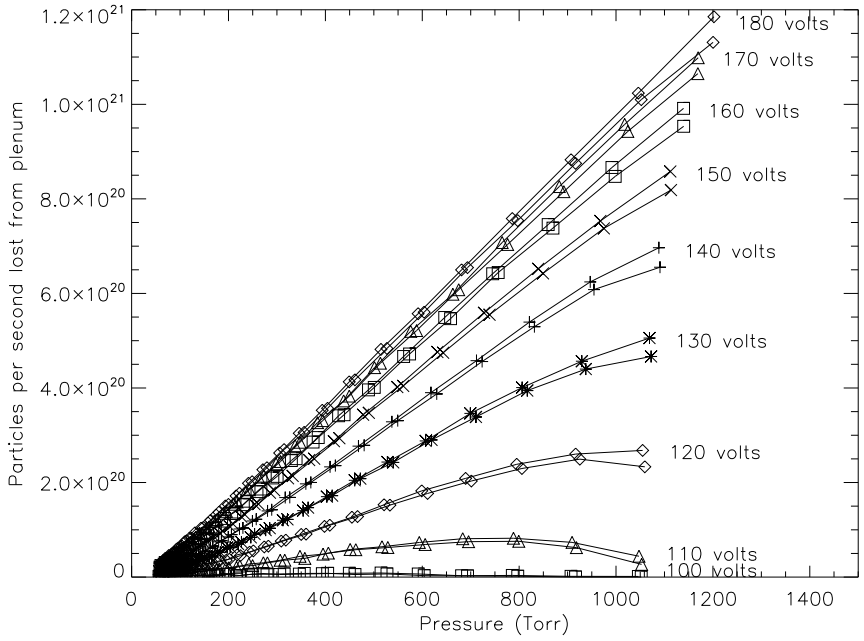


Figure 2.6: Fuelling nozzle flow for 100ms pulses of varying voltages for two pressure scans. The data was recorded on H-1.

Software was also developed to operate the molecular beam source on H-1. This allows control of the molecular beam source settings through the H-1 MDSplus model shot. Using a simple control interface the diagnostic beam settings are automatically recorded in the H-1 MDSplus data structures. A description of this system is included in appendix B.

In order to implement automation of the experiment, some modification of the existing MDSplus to Labview interfacing routines were required. This was to prevent system crashes resulting from memory leaks, which occurred after around 400 shots. This was alleviated by modifying the Labview codes to explicitly close all data references generated to interface with MDSplus. Doing so allowed the system to complete

experimental runs in excess of 2000 shots without difficulty.

The database holding recorded data was found to have short error 'bursts' where every second shot was missing. The missing data is likely to have been a result of conflicting resource requests between the Labview control program and the Windows ME operating system. The impact of these bursts on the experiment was reduced by making repeat measurements at similar conditions. By repeating each measurement 5 times, the number of valid shots at any condition was always greater than 2. Of the total database, around 2% of the shots were lost due to these error bursts.

The final database used to characterise the nozzle was over 60 gigabytes in size. This presented a challenge in terms of data analysis. As it was not possible to manually manipulate the entire data set, IDL routines which scanned through the database were written to explore the physical meaning of the acquired data.

## 2.4 The anemometer system

Density and velocity of the molecular beam were measured using a four channel hot wire constant temperature anemometer. The anemometer was constructed for the characterisation of the fuelling molecular beam source by Scott Collis [1]. The design of this system was similar to an instrument used in the diagnosis of high density hydrogen gas jets [16]. Some modification to this existing system was required for the successful application of the instrument to the low beam densities of the diagnostic

molecular beam source.

The anemometer measures particle fluxes by determining the power required to maintain a probe wire at constant temperature. Heat is lost from the probe through particle flux, electromagnetic radiation, and conduction to the mounts of the probe wire. Constant temperature anemometry employs feedback control of the heating current through the probe wire to maintain a target probe resistance. If the probe is cooled uniformly, then the feedback circuit maintains a constant probe temperature; the power lost through radiation and conduction to the mounts is constant. The extra power required to heat the probe while the probe is in a flow is then a measure of the particle flux [17].

The functional relationship between the particle flux to heat lost from the probe depends on the physical processes dominating heat transfer in the beam. The functional dependence can be simplified to considering the exponent m of the relationship between the Nusselt number Nu and the Reynolds number Re[25]. That is:

$$\mathrm{Nu} \propto \mathrm{Re}^{\mathrm{m}} \tag{2.12}$$

In slow moving continuum fluids $\mathrm{m} = \frac{1}{2}$ This relation is termed King's Law and in this situation it is expected that:

$$\mathrm{H} \propto (\rho \mathrm{v})^{\frac{1}{2}} \tag{2.13}$$

where H is heat lost from the probe, $\rho$ is the fluid density, and v is fluid velocity [26]. If fluid density is reduced sufficiently molecular motions alone need be considered and hence the regime is called free-molecular flow. In this situation the amount

of heat removed from the probe by a molecular interaction has no dependence on density and m = 1. A free-molecular flow is typified by a high Knudsen number Kn on the order of 10 or more[25]. The Knudsen number is found by:

$$\mathrm{K_N} = \frac{\lambda}{\mathrm{L}} \tag{2.14}$$

where $\lambda$ is the mean free path between inter-molecular collisions, and L is a characteristic scale length of the problem being considered. The nozzle exit diameter was used for L. $\lambda$ is found by[22]:

$$\lambda = \frac{1}{\sqrt{2}\pi(r_{He})^2 n} \tag{2.15}$$

where $n$ is the beam particle density local to the anemometer probe and $r_{He}$ is the van der Waals radius of helium of 140 picometres reported by A. Bondi [23].

If a uniform beam density is assumed the outer anemometer probe with the probe array 32mm from the nozzle throat will intersect a very similar beam density to the center anemometer probe with the difference in signal only due to the slightly larger distance over which the beam diverges. The center probe is 32mm from the nozzle throat while the outer probe is 35mm from the nozzle throat. Considering beam divergence alone and assuming that the measured beam density has an inverse square dependence on distance the two beam densities should vary by around 20%. If it is assumed $m = \frac{1}{2}$ then the variation of anemometer signals should be around 10%. From the recorded signal attributed to these anemometer probes (described fully in chapter 3) the variation in signals recorded for the most dense beams (1400Torr plenum pressure and 150 volts DC piezo drive) is close to 95%. This demonstrates that the observation of a centrally peaked density profile is real and can not be an

artifact of the assumed value of m.

The beam density must be approximated to establish Kn while Kn is required to establish the functional dependence m of the anemometer signals and subsequently determine beam density. As an approximation the beam density profile is calculated based on the assumption that m=1, and then Kn at each of the probe positions calculated for the most dense beam conditions. The table on page 65 includes the minimum Knudsen values calculated. As each Kn is on the order of 10 the assumption that all the used probes have an m=1 functional dependence is justified and adopted.

The circuit used to maintain constant probe resistance and to determine the power dissipation by the probe is shown in figure 2.7. It uses a resistive bridge that includes the probe resistance. If the resistance of the probe is too high, the feedback circuit reduces current through the bridge. This, in turn, lowers the power dissipated by the probe, causing its temperature to fall and resistance to decrease. Conversely, if the probe resistance is too low, the feedback circuit increases current through the bridge. This increases power dissipated by the probe, as well as its temperature and resistance.

The ratio of resistances in the reference arm of the bridge determines the quiescent temperature of the probe. The voltage dropped across the known resistor, in series with the probe, determines the current passing through the probe. As the probe resistance is being held constant by the feedback circuit, the power dissipated

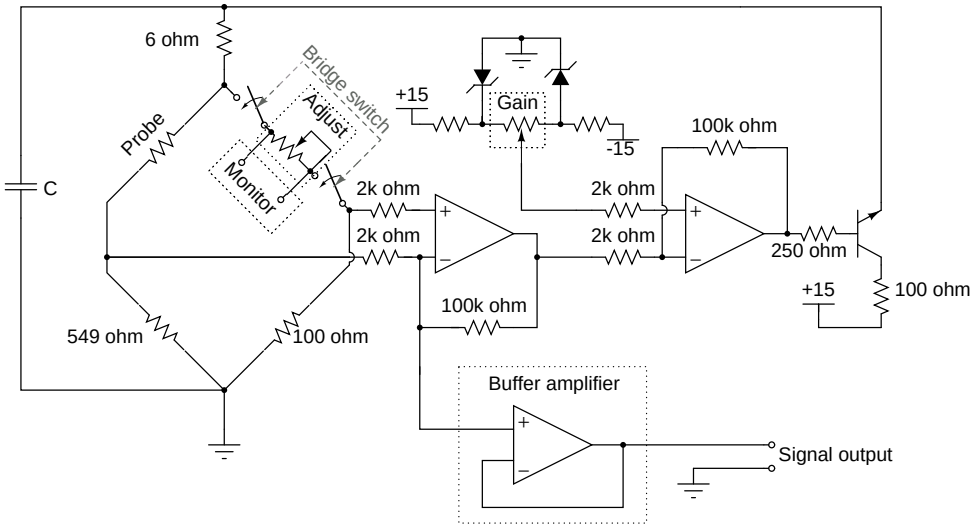


Figure 2.7: The circuit used for constant temperature anemometer measurements. The capacitor C was installed across the bridge to reduce noise from oscillations. The buffer amplifier was installed to prevent digitiser noise from the National Instruments DAQ card from disturbing the anemometer feedback loop.

by the probe is calculated using Ohm's law.

The "adjust" resistor changes the quiescent temperature of the probe. By opening the bridge switch and measuring the resistance between the monitor terminals, $R_{adj}$ is measured and the ratio of the resistors in the reference arm of the bridge is determined. The probe resistance R is then given by:

$$R = \frac{549 \times R_{adj}}{100} \tag{2.16}$$

The gain resistor is adjusted as a compromise between maximum sensitivity to signals and stability. In practice, the gain is set as close as possible to the threshold of feedback oscillation. Large anemometer signals can initiate feedback oscillations if the gain is too close to the oscillation threshold.

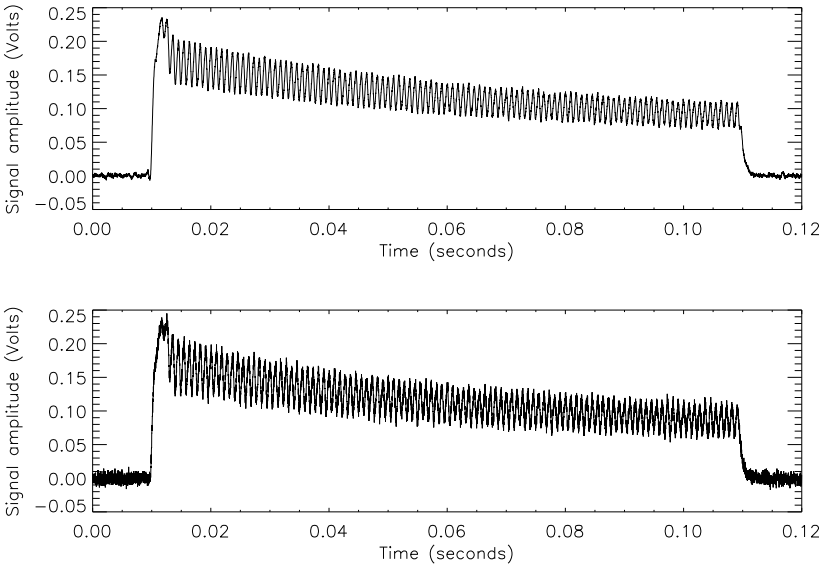


Figure 2.8: Both plots show the anemometer response to the flux from the molecular beam source modulated at 1kHz. The upper plot shows the system response with a 4.7$\mu$F capacitor installed across the bridge (C=4.7$\mu$F). The lower plot shows the system response without a capacitor across the bridge (C=0$\mu$F). The capacitor can be seen to reduce the noise in the anemometer instrument without compromising the response to modulated signals.

The capacitor C in figure 2.7 was inserted to suppress high frequency noise in the anemometer circuit. The effect of introducing a capacitor across the resistive bridge was investigated by comparing the system response with and without the 4.7$\mu$F capacitor installed. Figure 2.8 shows the recorded signal for both cases in response to the flux from modulating the valve at 1kHz. The capacitor is shown to reduce noise in the anemometer circuit without significantly changing the response to modulated signals.

To increase the anemometers sensitivity to low fluxes, lamp filaments were used instead of straight, fine tungsten wire. This decision was made after attempts to

fabricate reliable probes with tungsten wire were unsuccessful. It is difficult to wet tungsten with tin-lead solder, especially when using 10 micron wire. A close inspection of the attempts to solder-mount tungsten wires suggested that they were fixed in place by encasement in the solder. This method requires the tungsten wire to be wrapped around the copper mounting wires and then soldered. The nature of the electrical connection between the tungsten wire and the solder introduced variations in resistance of up to 50% for wires of a similar length. Such a variation in the probe resistance makes uncertainties difficult to quantify. A further complication of this method was the complexity in handling fine tungsten wires. It was difficult to produce taut, fixed-length wires reliably. Loose wires wobble considerably in the beam, and can strongly couple mechanical vibrations into the measurements. By displacing the copper mounts and therefore tensioning the wires, a variation in wire length is introduced. As a consequence, having to replace a wire in the middle of a scanned experiment meant the required systematic analysis parameters are changed. This becomes impractical to account for when a large volume of data is intended to be analysed and compared. It is very easy to over-tension the fine wires, thereby breaking them and requiring the tedious mounting process to begin again. Lamp filaments provided a solution to all of these problems.

Lamp filaments as manufactured are already mounted to solder-wettable posts by crimping. This gives a reliable electrical and mechanical connection. The mounting posts used in lamp's are easily soldered to the copper mounting wires. The helical lamp filaments become self-tensioned spring-like probes which can be mounted with determined spatial characteristics and considerable tolerance to over-tensioning.

Low-voltage switch illumination lamps were widely available and had less than a 2% variation in resistance at room temperature. The characteristics of the lamp filaments guided the selection of the best lamp type to be used. Higher voltage, low-wattage globes were found to have the finest filaments, thereby offering the best sensitivity to low density gas variations. Sometimes higher voltage ratings are achieved in lamps by using long filaments rather than fine filaments. This increases problems associated with departure from constant temperature of the probe as a result of the beam flux profile. 24 Volt 20ma lamps were selected for use, as they had short coils of the smallest diameter wire of all the globes tested. The resistance of these lamp filaments at room temperature is approximately 150Ω.

One complexity introduced by using lamp filaments instead of fine tungsten wire was the increased difficulty in considering the interaction between directed beam particles and the helical geometry of the filament. By using an anemometer channel for background measurement, no geometric comparison between the beam and background components need be made, as the background component is independently determined and subtracted. The precise interaction with the beam and the coil is then combined with the other unknown coefficients of proportionality and are determined in the anemometer instrument calibration.

To establish the flux profile of the molecular beam, the position of the anemometer array was varied. Figure 2.9 shows the range of angles measured by the outer anemometer probe with the anemometer array in the positions indicated. By combining data from shots with a range of anemometer array positions, the flux profile

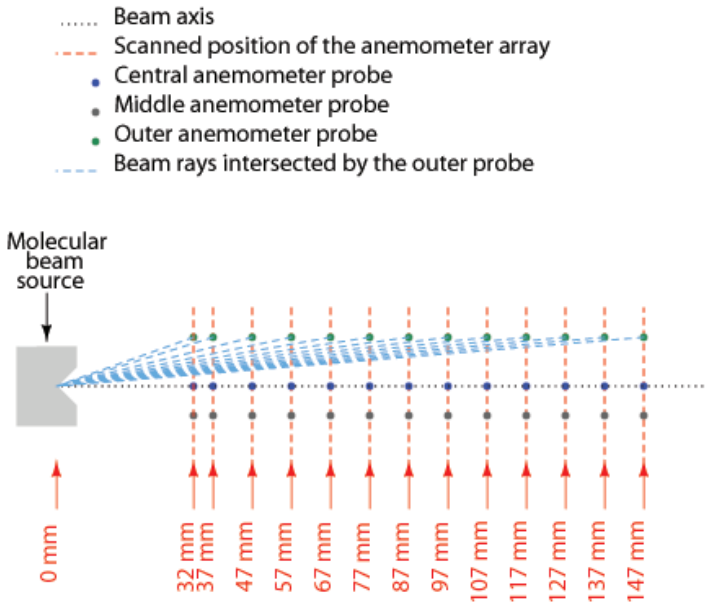


Figure 2.9: The angular dependence of the beam flux is explored by varying the distance between the nozzle and the anemometer array holding the probe wires. The beam angles intersected by the outer anemometer probe for a range of anemometer array positions is shown. In a single shot only 3 data points are obtained corresponding to a single anemometer array position.

can be determined using more data points than the number of anemometer channels available for a single shot.

A catastrophic cooling of the central probe element occurs when then anemometer array is too close to the nozzle. When this occurs it is observed that the most central part of the heated probe darkens (cools) and the ends become brighter (hotter). The characteristics of catastrophic probe cooling is an apparent signal saturation, as well as the probe signal persisting after the shot has ended. Catastrophic cooling is likely to be a result of overloading the power capabilities of the anemometer feedback circuit. To demonstrate a catastrophically cooled probe, figure 2.10 shows the signal on the central and middle anemometer channels with the anemometer array

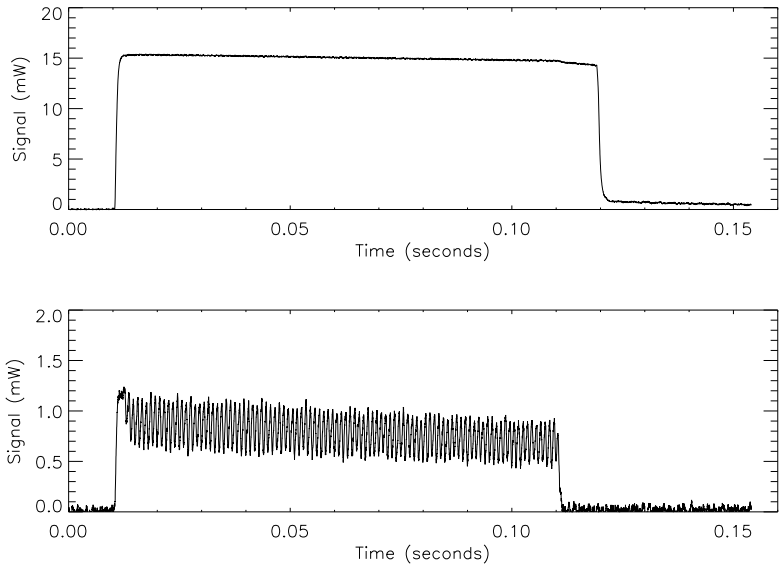


Figure 2.10: The upper plot shows the signal from the central anemometer probe 17mm from the nozzle with a plenum pressure of 1400 Torr and the piezo drive modulated at 1kHz. The lower plot shows the middle anemometer probe data for the same shot. Due to a catastrophic cooling of the central probe it appears to saturate. Typical of catastrophic probe cooling, the central anemometer signal persists after the pulse has ended and takes more time to return to quiescent conditions than the adjacent anemometer probe.

17mm from the nozzle. The middle anemometer probe shows what the beam should look like. The persistence of the central anemometer signal after the end of a shot is used as an indication of a catastrophic probe cooling in later analysis.

## 2.5 Vacuum test tank

The test tank was rescued from a rubbish heap 15 years ago, and since then has been used for a variety of applications in the Plasma Research Laboratories. It is a cylindrical vessel with its axis aligned to that of the beam. In the direction of

the beam, the tank is approximately 1 meter long and has a diameter of 370mm. The precise volume also includes the volume of the plumbing to the vacuum pumps, less the displacement of fixtures inside the tank. The tank can be isolated from the vacuum pumps, however to allow automated experiment regimes, the isolation valve was not used. The introduction of a background anemometer wire removed the need to manually isolate the tank between experiment shots. The tank provided mounting fixtures for the molecular beam source with feed-through connections for gas supply, piezo drive, and anemometer probes mounted on a removable flange, as shown in figure 2.11. The design of the anemometer array mounting attempted to minimally interfere with the flow being measured. By keeping the array frame perpendicular to the beam and scanning it the downstream disruption caused by the frame is not measured and can be neglected. The tank vacuum was established by a turbomolecular pump backed by a rotary vane pump and were connected to the main tank volume throughout data collection.

The test tank was used previously for characterisation of the fuelling nozzle, and already included mounting hardware for the nozzle to be tested. The volume of the plenum and included plumbing in the test tank is 177mL as measured by Scott Collis by filling it with ethanol. The ethanol was then poured into a measuring cylinder to determine the volume. Two rods on a rotatable collar allow the array of anemometer wires to be traversed through the molecular beam. The plane of the anemometer array can be displaced between 15mm to 150mm from the nozzle.

To change the position of the anemometer array on the mounting posts, the vacuum

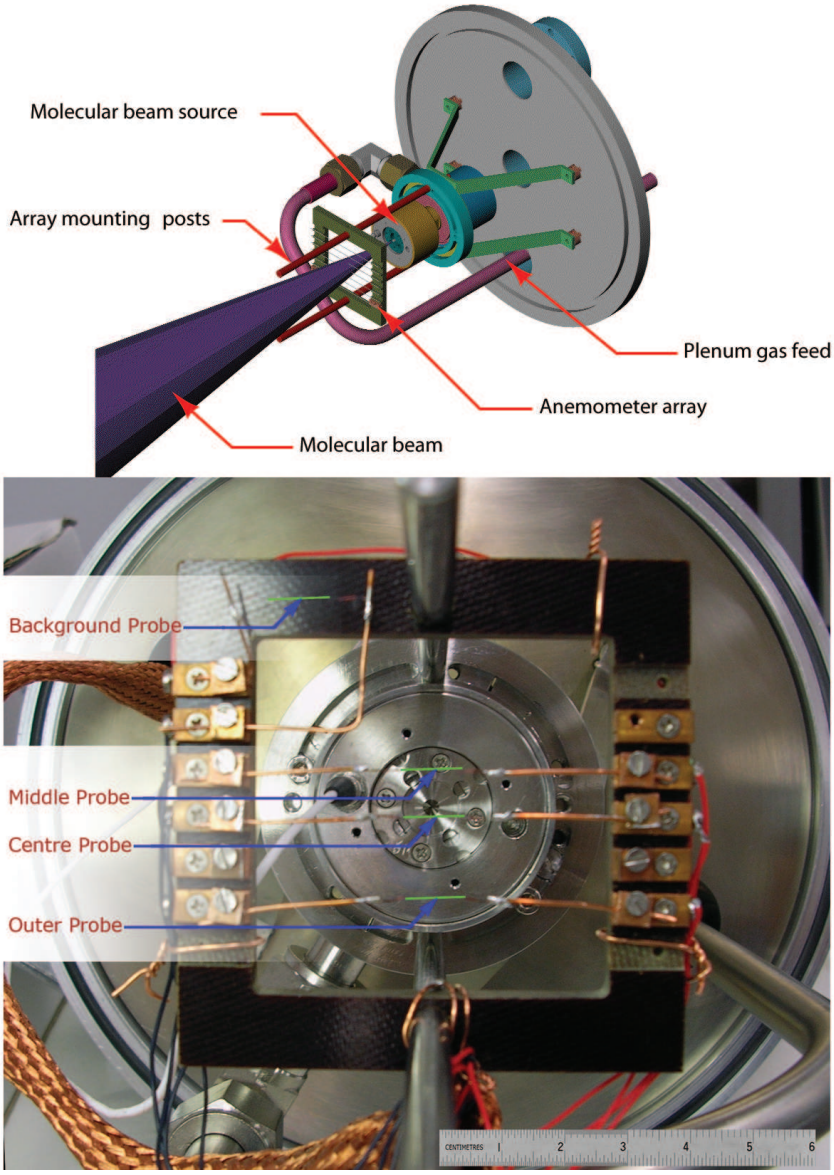


Figure 2.11: Upper image is a CAD drawing of the removable flange of the vacuum test tank holding the molecular beam source and anemometer probe array courtesy of John Wach. The molecular beam has been included to clarify the arrangement. The anemometer array can be moved on the mounting posts to change the distance between the probes and the beam source. The lower image shows a photograph of the actual anemometer array.

in the test tank must be broken. A series of automated experiments were conducted to minimise the number of vacuum-breaks required. These involved scans of drive voltage, plenum pressure and modulation frequency, with the anemometer array at fixed distances from the molecular beam source. This distance was changed between each series. Gas feed to the nozzle was also broken in order to adjust the anemometer array's position. By doing so, the plenum needed to be purged of air before filling with helium.

It was found that by opening the valve once the tank was at low pressure, the mechanical interaction between the beam and the probe wires was enough to break the probes when positioned close to the nozzle. This did not occur during short beam pulses characteristic of the experiment. Failure only occurred during sustained flow typical of a plenum purge. The filaments were most likely broken due to a vibrational mode which fatigued the tungsten. The hypothesis that vibrational modes were excited in the anemometer probes is supported by the observed anemometer signals during beam pulses. Anemometer signal oscillations observed close to the beam source are not present further away, and are assumed to be a result of such filament vibrations. To prevent probe damage occurring during plenum purging, the piezo valve was opened prior to initiating the vacuum pumps. By doing so the nozzle flux was greatly reduced during the plenum purge and the filaments were protected.

## 2.6 Plenum pressure control

Changing the plenum pressure is an effective way to modify the density of the beam. The plenum filling valves and pressure measuring hardware are unchanged from those used in the fuelling nozzle system. The plenum pressure is measured by a VRC capacitive manometer. The instrument's time response prevents the accurate discernment of rapid pressure changes. Further, digitiser noise makes it difficult to resolve the pressure signal accurately enough to allow pressure differences typical of a 10 ms diagnostic beam pulse without time averaging the signal. Due to both of these considerations, time averaging was used to attain higher pressure resolution, with a further reduction of time resolution of pressure transitions. A voltage ranging from 0 to 1.5 volts taken from the pressure gauge head represents pressures ranging from 0 to 1500 Torr.

The gas pressure in the plenum is reduced by opening the piezo valve of the molecular beam source. This bleeds plenum gas to the vacuum. Care was required to ensure that that the vacuum pumps could remove these bled particles prior to taking data.

The plenum pressure is increased using the hardware shown in figure 2.12. The National Instruments DAQ card generates a 5 volt logic high to fill the plenum. The 5 volt signal is converted to a 24 volt signal and then fed to the coil of the solenoid valve. The solenoid valve then allows compressed air into the control port of the pneumatic valve, causing it to open. When the pneumatic valve opens, the volume of the system on the molecular beam side of the needle valve increases. At the same time, a surge of gas enters the plenum when the pneumatic valve first opens. This is

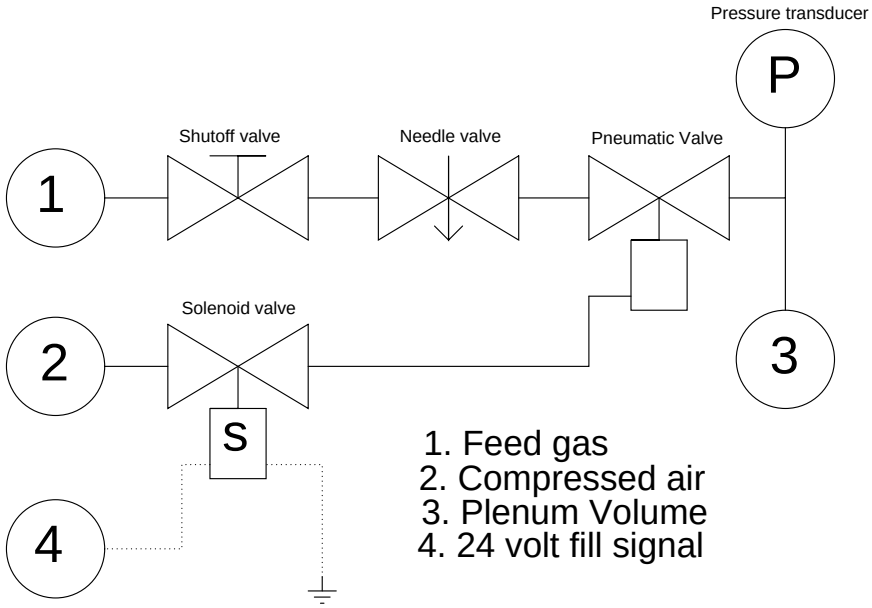


Figure 2.12: A schematic representation of the hardware involved in filling the plenum with feed gas. 24 volts fed to the solenoid valve ports compressed air into the pneumatic valve which connects the fill gas supply to the plenum through a shutoff valve and a flow limiting needle valve.

a consequence of the dead space between the needle valve and the pneumatic valve inlet port. The size of the surge depends upon the plenum pressure and the fill supply pressure. After the surge, the rate at which the plenum fills depends upon the fill supply pressure, the plenum pressure, and the restriction to flow the needle valve offers. When the control voltage on the solenoid valve coil returns to 0 volts, the solenoid valve and the pneumatic valve close. As the pneumatic valve closes, the volume of the line decreases slightly and the pressure in the plenum increases.

# Chapter 3

# Beam characterisation in the test tank

In this chapter a simple empirical model of the molecular beam is proposed and tested. The approach used to model the beam was motivated by the expectation that the anemometer signal from an appropriate position in the beam is sufficient to roughly approximate the beam shape regardless of the plenum pressure and valve opening voltage. Given this supposition it is shown that parameters describing the beam shape are simple monotonic functions of the specified signal intensity alone. This model takes into account the errors resulting from background particles in the test tank and the anemometer instrument's response to non-uniform cooling of the anemometer probes. The chapter begins by considering how to calibrate the anemometer instrument.

## 3.1 Calibrating the anemometer signals

In order to relate the measured anemometer signals to a beam flux local to the anemometer probes the signals measured must be calibrated to reflect a known quantity. The molecular beam is considered to have a flux density referenced to a surface 1mm from the nozzle of $\Gamma(t, \theta)$ dependent on time t and angle $\theta$ relative to the beam axis. The beam is assumed to be symmetric in rotation around the beam axis. This is justified by the similarity in anemometer signals measured with the array rotated about the beam axis, as shown in figure 3.1. Apart from the oscillations observed in the middle-radius anemometer probe data, the signals support the assumption that the beam is symmetric about the beam axis.

The loss of particles from the plenum can be determined by the plenum pressure difference $\Delta p$ for the shot. The number of particles N in the beam is assumed to be equal to the number of particles lost from the plenum. The absolute change in plenum pressure for a shot never exceeds 1%. The temperature change of plenum gas is considered to be of similar absolute value and accordingly negligable. N is found by calculating:

$$N = \frac{\Delta p\, V}{R\, T} \tag{3.1}$$

For the specific case of the molecular beam in the test tank the relationship is then:

$$N = \Delta p \times 5.833 \times 10^{18} \tag{3.2}$$

Where $\Delta p$ is in units of Torr and N is in units of particles. To use the N value to calibrate the anemometer signals in terms of flux, an algorithm is required. To allocate N to time t and angle $\theta$ coordinates of the as yet unknown $\Gamma(t, \theta)$, a functional

relationship is established such that:

$$N = 2\pi \, \mathrm{t_s} \sum_{\text{all times}} \int_0^{32} \Gamma(\mathrm{t}, \theta) \, \sin(\theta) \, \mathrm{d}\theta \tag{3.3}$$

where the integrand is a summation of flux over a spherical surface. The summation is done for all times in the shot where the beam is operating and $\mathrm{t_s}$ is the time between samples of the $\Gamma(t, \theta)$ data. $\theta$ is only considered to range between 0° and 32° as per the discussion presented in section 2.1.3. $\Gamma(t, \theta)$ can be considered to describe the nozzle flux for a beam angle $\theta$ and time t for a specific point on the reference surface. $\theta = 0$ is the beam axis. The nozzle flow $\dot{\mathrm{N}}$ is then:

$$\dot{\mathrm{N}} = 2\pi \int_0^{32} \Gamma(t, \theta) \, \sin(\theta) \, d\theta \tag{3.4}$$

To turn $\Gamma(t, \theta)$ into a beam density the velocity of the beam must be determined.

Determining $\Gamma(t, \theta)$ from anemometer data is not trivial, as data collected depends upon beam angle variations with time, plenum pressure, and valve drive voltage. Background particles interact with the anemometer probe. Also they are entrained into the beam dependent on the background pressure and the anemometer element's displacement from the nozzle. In addition to these experimental effects, the anemometer instrument's response to beam fluxes that vary over the length of the probe is uncertain. The signals need to be scaled to a flux reference. Before an approximation of $\Gamma(t, \theta)$ can be made, all of these issues need to be addressed.

The beam and background gas dynamics inside the test tank are considered to be of a free molecular type for the probes shown to have Kn on the order of 10. That is, for these probes collisions between the directed beam and the isotropic background

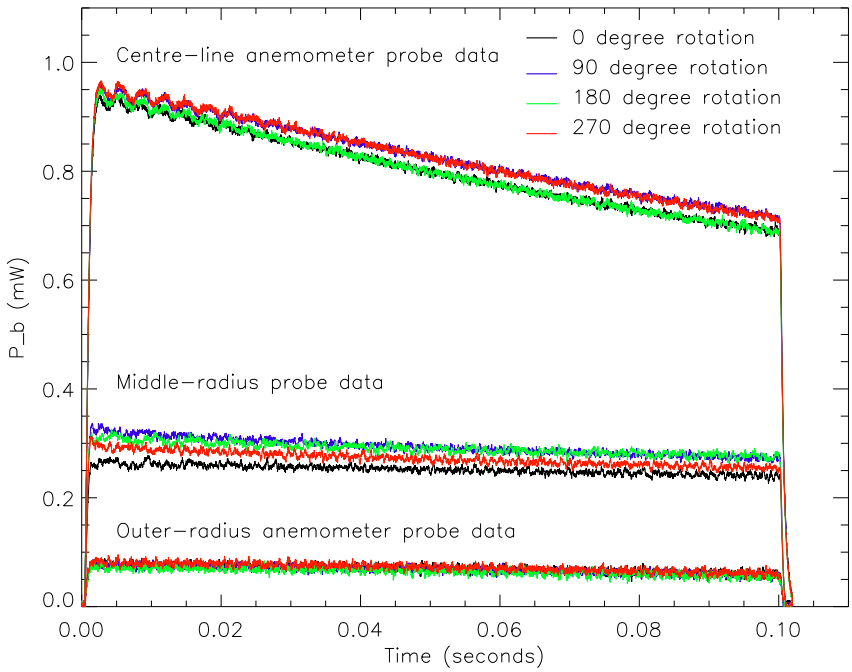


Figure 3.1: Shown is the variation in anemometer signals observed when the anemometer array is rotated about the beam axis. The colours indicate the angular position of the anemometer array. The observed 320 Hz oscillation on the centre-line anemometer probe has a phase that is independent of angular position of the anemometer array and is considered to be a filament wobble. Unlike the oscillation on the centre-line anemometer wire, the 230 Hz oscillation on the middle-radius anemometer wire has a phase that is dependent on the array alignment. It is hypothesised, but not proven, that these oscillations are a consequence of shocks forming in the diverging part of the nozzle. Observation of the beam in H-1 will help determine if this anomaly is a property of the beam or the test tank. Apart from this oscillation, the signals support the assumption that the beam can be considered symmetric about the beam axis.

are considered to act independently on the anemometer probe and are consequently separable by subtraction.

## 3.2 Separating the beam flux signal from the background

The power dissipated by the probe P, is found using the current through the probe I and the probe resistance R (from equation 2.16). The dissipated power P is then

$$P = I^2 R \tag{3.5}$$

The voltage measured across the bridge resistor in series with the probe V and the series bridge resistance value of 549Ω determine I, making P:

$$P = \left(\frac{V}{549}\right)^2 R \tag{3.6}$$

The quiescent power $P_Q$ is defined to be the power dissipated by the probe prior to initiating the beam pulse. The signal contains radiated and conducted power loss terms that, based upon assumed constant temperature of the probe, will not change during the shot. Using equation 3.6 $P_Q$ is determined from the quiescent voltage on the bridge resistor in series with the probe $V_Q$. $P_Q$ is then:

$$P_Q = \left(\frac{V_Q}{549}\right)^2 R \tag{3.7}$$

$P_s$ is defined as:

$$P_s = P - P_Q \tag{3.8}$$

$P_s$ is now independent of power lost by conduction through the probe mounting posts and radiation from the probe filament. Only power lost to the beam flux and background flux components remain in $P_s$. $P_s$ is separated into the power lost to the beam flux $P_b$ and the power lost to the background flux $P_{bg}$ related in the form:

$$P_s = P_b + P_{bg} \tag{3.9}$$

$P_{bg}$ is obtained from the dedicated background measuring anemometer probe which is shielded from the beam. Shielding prevents direct interaction between the beam and the probe. In this case $P_b$ must be zero, and $P_s$ directly gives $P_{bg}$. Once $P_{bg}$ is determined for a shot it is used to remove the background component from the signals of the beam measuring probes for that specific shot. $P_b$ is calculated by:

$$P_b = P_s - P_{bg} \tag{3.10}$$

The centre-line anemometer raw probe data V for a sample shot is shown in figure 3.2. Four key stages in the process are presented: the centre-line anemometer signal V, the centre-line anemometer combined background and beam flux power loss $P_s$, the background flux power measurement $P_{bg}$, and the power lost to beam flux $P_b$. It can be seen that $P_b$ returns to zero as expected at the end of the beam pulse.

## 3.3 Beam interaction with the background

As the background pressure in the test tank increases, the anemometer signals reduce if the anemometer array is far away from the nozzle. It is proposed that the observed signal variations are due to the beam's interaction with the background

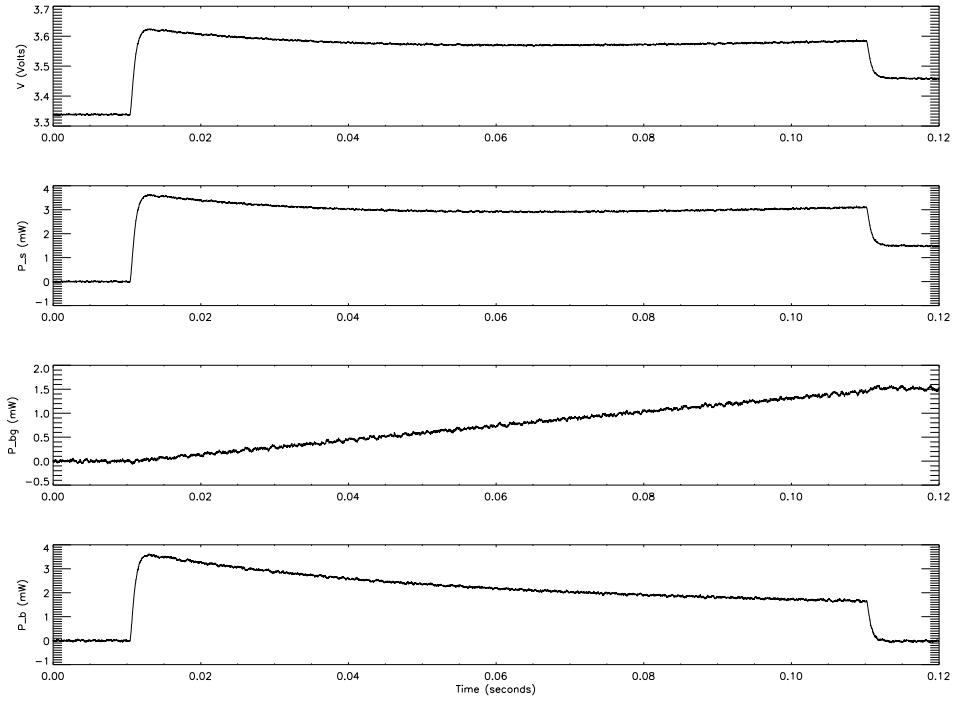


Figure 3.2: Example of the anemometer signal processing for a sample shot. Shown are four stages in the process: the centre-line anemometer signal V, the centre-line anemometer combined background and beam flux power loss $P_s$, the background flux power measurement $P_{bg}$, and the power lost to beam flux $P_b$.

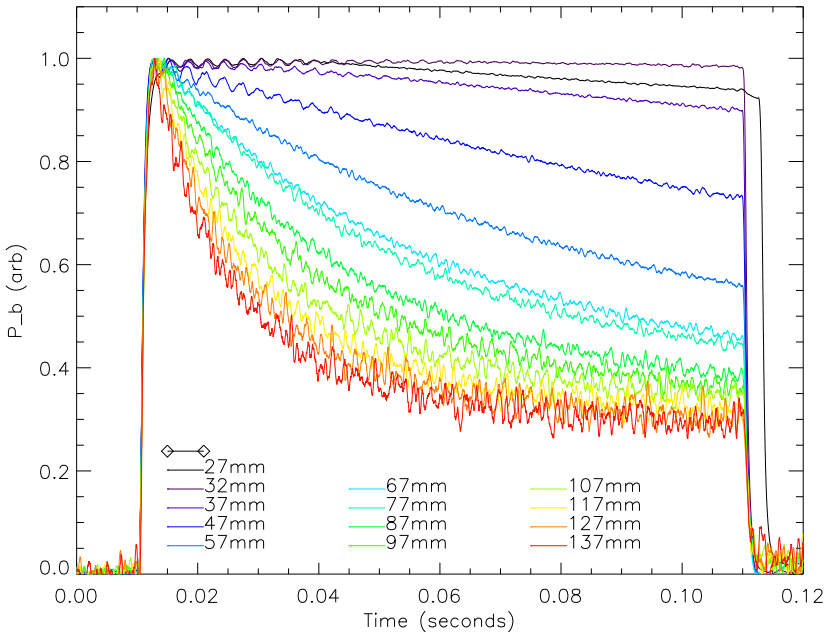


Figure 3.3: Shown is a collection of centre-line anemometer signals with various distances between the anemometer array and the nozzle. The $P_b$ values have been scaled to have a value of 1 at the beginning of the pulse to highlight beam interactions with the background. A catastrophic cooling of the probe is seen when the anemometer array is 27mm from the nozzle.

particles. To explore the beam's interaction with the background gas a series of shots at fixed plenum pressure and drive voltage were collected over a range of anemometer array positions. The magnitude of the power signals was scaled so that each had a peak value of 1.0 at the start of the pulse where the background gas interaction is negligible. Centre-line anemometer data for shots with a 1400 Torr target plenum pressure and 150 Volts piezo drive are shown in figure 3.3. The signal measured 27mm from the nozzle demonstrates a catastrophic cooling of the probe.

Using a 'mean free path' based model of the beam particle and background interactions, $P_b$ should decay exponentially in time and distance from the nozzle if

it is assumed each measurement is made at a fixed distance from the nozzle with the background density increasing linearly in time. In the data plots of figure 3.3 this exponential decay is seen to be partially true. Although a component of the exponential decay is observed, a non-zero asymptote is also present, most clearly seen in data taken furthest from the nozzle. This is considered to be a result of the background gas and beam particles interacting through collisions.

To duplicate the measured signals a simple heuristic model of beam scattering by the background is constructed. In this model $P_b(t)$ values at the available anemometer array positions z millimeters from the nozzle will be predicted by the array $\mathbf{C}(z, t)$. $\mathbf{C}(z, t)$ is then defined as the predicted signal at a distance r from the nozzle at time t with the intensity scaled to unity at the start of the pulse. The shot has been selected so that the background density rises linearly with time. As the signals have already been scaled to unity at the start of the shot, no z-dependent terms for signal magnitude are required and the model needs to have a value of 1 at t=0. It is assumed the beam is attenuated by scattering off background particles, with attenuation length $\lambda$, the mean free path (a function of background density and hence time). The value of $\lambda$ is time dependant and later will be replaced with a time dependent function to achieve a time dependence in the model. The non-scattered portion of the beam $U(z, \lambda)$ is given by:

$$U(z, \lambda) = \exp\left(\frac{-\kappa_1 z}{\lambda}\right) \tag{3.11}$$

where $\kappa_1$ is a constant to reconcile distance scaling. The forward scattered signal $S(z, \lambda)$ is defined as some fraction $\epsilon(z)$ of the scattered beam and background

particles still appearing as part of the beam. $\mathrm{S}(\mathrm{z}, \lambda)$ is assumed to be:

$$\mathrm{S}(\mathrm{z}, \lambda) = \epsilon(\mathrm{z}) \left(1 - \exp\left(\frac{-\kappa_1 \, \mathrm{z}}{\lambda}\right)\right) \tag{3.12}$$

The value of $\epsilon(z)$ depends upon the distance z to the nozzle, and an analytical determination of this function is beyond the scope of this thesis. Instead a fixed value $\epsilon$ is assumed, and determined from the observed asymptote from figure 3.3 to be approximately 0.31. $\mathbf{C}(\mathrm{z}, \lambda)$ is then the combination of S and U such that:

$$\mathbf{C}(\mathrm{z}, \lambda) = \mathrm{U}(\mathrm{z}, \lambda) + \mathrm{S}(\mathrm{z}, \lambda) \tag{3.13}$$

$$\mathbf{C}(\mathrm{z}, \lambda) = \exp\left(\frac{-\kappa_1 \, \mathrm{z}}{\lambda}\right) + 0.31 \left(1 - \exp\left(\frac{-\kappa_1 \, \mathrm{z}}{\lambda}\right)\right) \tag{3.14}$$

From reference [22] $\lambda$ is inversely proportional to background density n. By experiment design n is linearly dependent on time such that:

$$\lambda \propto \frac{1}{\mathrm{n}} \tag{3.15}$$

$$= \frac{\kappa_2}{t} \tag{3.16}$$

where $\kappa_2$ is a parameter related to collision cross sections and adjusts the time evolution of the exponential decay in the model. $\kappa_1$ and $\kappa_2$ are both constants and are combined to form $\kappa$. Equation 3.14 can then be re-written replacing $\lambda$ with t:

$$\mathbf{C}(\mathrm{z}, \mathrm{t}) = \exp\left(\kappa \mathrm{z} \mathrm{t}\right) + 0.31 \, \left(1 - \exp\left(\kappa \mathrm{z} \mathrm{t}\right)\right) \tag{3.17}$$

Attempts to fit a $\kappa$ to match the observed data were unsuccessful. An example of a 'good' fit for this function is shown in the upper plot of figure 3.4 as model A with $\kappa = -0.55$. Although $\epsilon$ was approximated, errors from the approximation can not account for the considerable discrepancies between the measured and modeled signals. The top prediction curve should coincide with the 27 mm data but instead

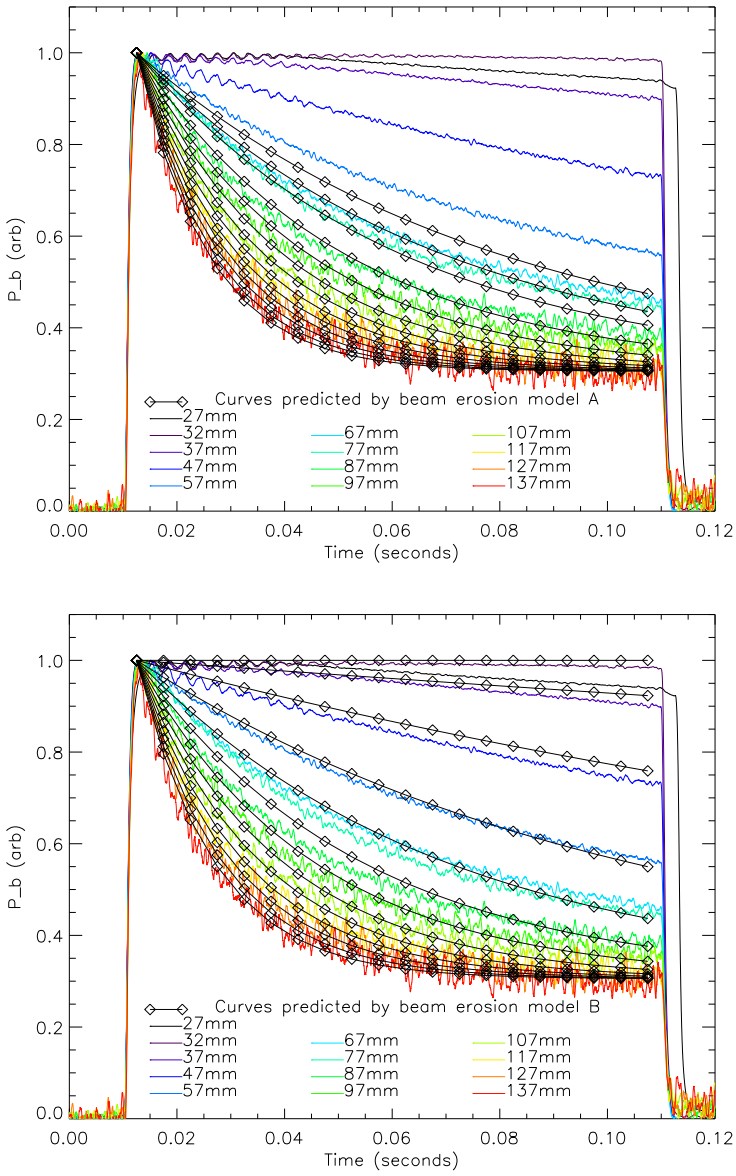


Figure 3.4: Both these plots show the same data from figure 3.3. The upper plot shows the best fit of model A overlaid as trend lines. The ability for model A to predict the signals is vastly improved if it is assumed no scattering takes place in the first 30 mm (model B). The lower plot shows the predictions of model B overlaid as trend lines. It is inferred from the improvement to the fit of the model that background particles are being excluded from the central part of the beam close to the nozzle.

better reflects the data expected at 60 mm. The model fits the data more accurately if there is considered to be a region devoid of background particles directly in front of the nozzle. By assuming that no scattering takes place in the beam for z less than 30 mm, then the model predicts the trend lines shown in the lower plot of figure 3.4 as model B with $\kappa = -0.65$. The fit of model B and to the measured data strongly suggests there could be a region devoid of scattering collisions directly in front of the nozzle. This finding is consistent with the hypothesis presented by one of the examiners that on the centre-line upstream of the 30mm point a continuum flow exists where background gas cannot penetrate the beam.

Local background density distortions are seen in the background signals collected with the anemometer array close to the nozzle. Figure 3.5 shows the background signal close to the nozzle steps up when the pulse has ended, an effect not seen further from the nozzle. The local background density appears to be reduced by the action of the beam near to the nozzle. This effect is observed more prominently in the outer-radius anemometer probe signal with the anemometer array near to the nozzle. The beam measurement appears to drop below the background level shown in figure 3.6. This is not a focusing of the beam as the central beam signal does not increase. The measured signal is considered to drop below the background signal due to the local background particle density being different for the background and outer-radius anemometer probes. It is proposed that this is a result of the beam distorting the local background particle density. This hypothesis is supported by the model's implication that close to the nozzle the scattering of beam particles by background particles is significantly less than expected.

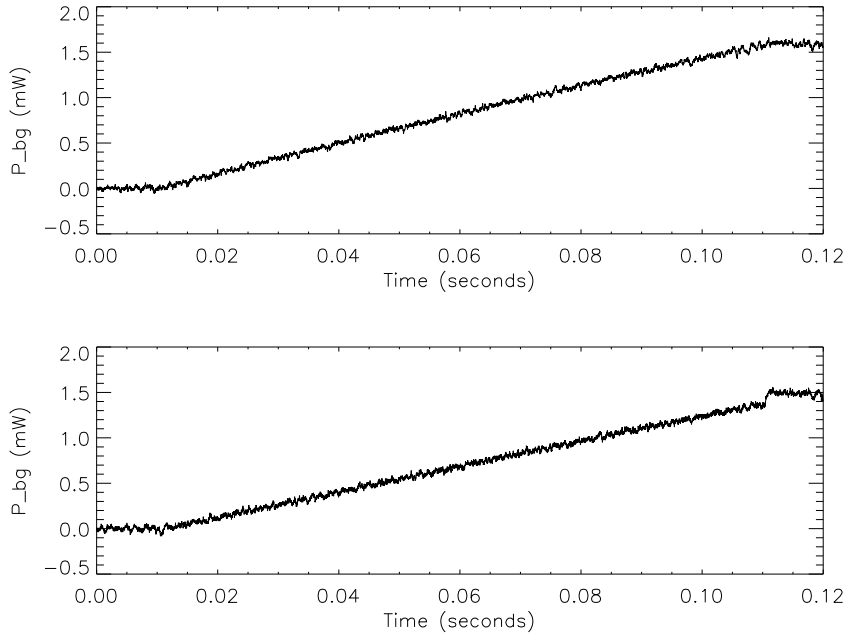


Figure 3.5: These plots show the background anemometer signal for shots with 1400 Torr plenum pressure and 150 Volt drive, with the anemometer array 147mm from the nozzle in the upper plot and 17mm from the nozzle in the lower plot. Close to the nozzle a step increase in background pressure is seen when the beam stops. This effect is not seen further from the nozzle. The observed flux step supports the hypothesis that the beam entrains background particles in the region near the nozzle.

An important difference between the test tank and H-1 is the volume into which the nozzle exhausts. The increase in background pressure in the test tank is far more rapid than in H-1. Scattering of the beam by background particles limits H-1 relevant results to the time interval where the test tank background density is low. To determine this period of time, signals with the anemometer array 147mm from the nozzle (the furthest) with 1400 Torr plenum pressure and a drive of 150 volts (maximum rate of background density increase) were assumed to represent the collected data most severely distorted by background interaction effects. Figure 3.7

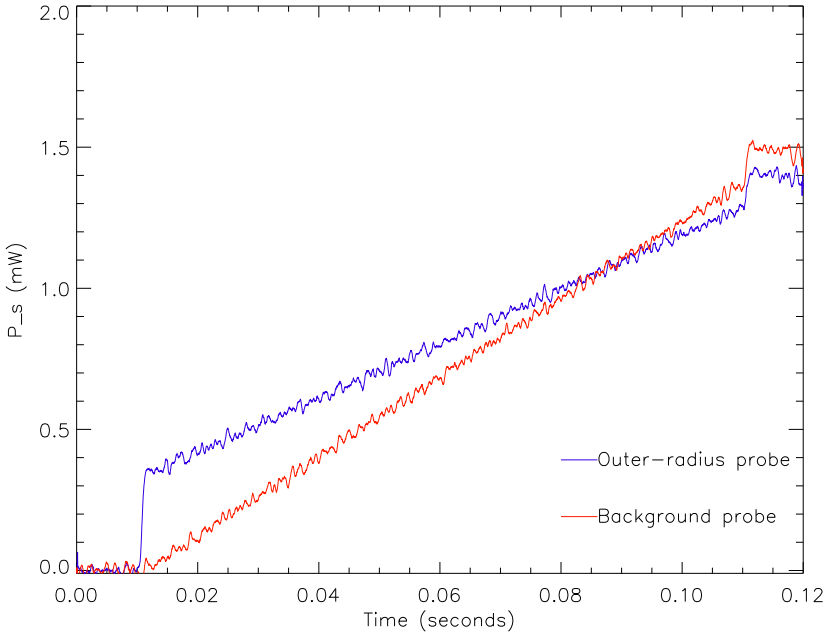


Figure 3.6: $P_{bg}$ and $P_s$ for the outer-radius anemometer probe with the anemometer array 17mm from the nozzle are shown. Notice that the outer-radius beam probe signal appears to fall below the background probe signal. This is attributed to distortion of the local background particle density by the beam. The arrangement of the probe wires is such that the background probe element is further from the beam axis than the outer-radius beam probe. Consequently the background probe measures a different background flux to the background flux local to the outer-radius beam probe. This effect is not seen with the anemometer array further from the nozzle.

shows the centre-line, middle-radius and outer-radius anemometer probe signals for this situation. The rise time of the centre-line anemometer probe signal is slower than the others due to lower gain in the centre-line anemometer amplifier. A time reference needs to be defined to describe the time interval to be used. 0 ms is defined as the point where the monitor signal for the piezo valve drive amplifier first exceeds 20% of the maximum recorded value. The analysis period was selected using the data shown in figure 3.7. Therefore, the time interval between 2ms to 5ms was selected to avoid risetime and background effects.

## 3.4 Using non uniformly cooled probe data

When the assumption that the probe filament has a constant temperature profile is not valid, subtraction of the quiescent conditions does not correctly account for the conducted and radiated heat during the pulse. An error is introduced which increases with the departure from constant temperature. The anemometer probes are heated using current driven by the feedback amplifier. If the anemometer probe is cooled non-uniformly, the rate at which heat is transferred to the probe via the current is also non-uniform along the length of the wire. The rate of heating for an element of the probe is linearly proportional to the element's resistance. Thus, if an element of the probe filament is cooled, the rate at which the driven current heats the cooled element is also reduced. As a consequence of the reduced filament resistance, due to lower temperature of the cooled elements, the feedback amplifier drives a heavier current through the probe.

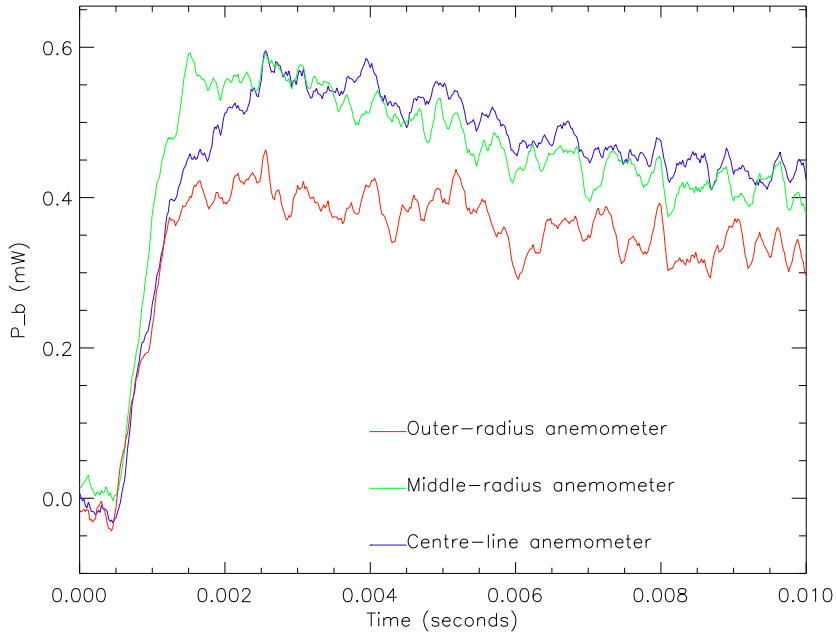


Figure 3.7: The centre-line, middle-radius and outer-radius anemometer probe signals are shown for a shot with 1400 Torr plenum pressure, 150 Volt drive, and with the anemometer array 147 mm from the nozzle. From inspection of data an analysis period starting 2ms after the monitor signal reference point (to avoid unreliable anemometer transient signals at the start of the pulse) to 5ms after the monitor reference point (to avoid background interaction effects) is selected. The 5ms point was selected as up to this time the signals show negligible variation with time.

This current delivers heat weighted to the temperature of each element of the probe. That is, the hot parts get hotter and the cool parts get relatively cooler. Conduction of heat along the probe filament stabilises this imbalance, so a new equilibrium condition will be reached. The probe filament will have a non constant temperature profile, having a temperature maximum where the particle flux is a minimum. If the maximum absolute change in temperature along the probe wire is small then the error can be ignored. In extreme cases of non- uniform cooling (close to the nozzle) situations like that shown in figure 2.10 occur where the probe is no longer sensitive to flux variations in the cooled regions. If $P_b$ is to be used to infer a particle flux accurately it is critical that only data from probes that are uniformly-cooled be considered. For non-uniformly cooled probe elements $P_b$ is influenced by radiated power variations, heat lost to the probe mounts, and the angle dependence of the beam flux. It is not in the scope of this thesis to analytically understand non-uniformly cooled anemometer probe data. Instead the amplitude of these anemometer signals will only be used if they can be individually calibrated. Probe signals partly effected are also discarded as no practical means of determining the degree of error was found.

To determine the probe positions that suffer from errors due to non-uniform probe cooling, the probe positions free from these errors are first determined. Figure 3.8 shows the position of the anemometer probes with the region of beam intersected by the probe highlighted. It can be seen that the outer-radius anemometer element lies closest to a region of constant angle to the beam axis. Assuming that the beam is symmetric about the beam axis, the outer-radius anemometer probe is effectively

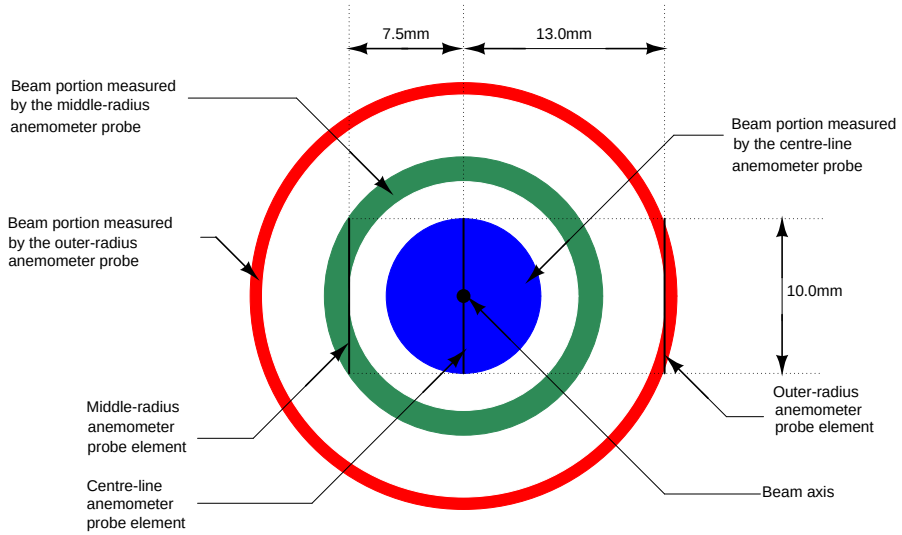


Figure 3.8: Shown are the anemometer probes overlaid with then regions of the beam measured by each probe. The beam-angles represented by these regions depend upon the distance of the anemometer array from the nozzle. The outer-radius anemometer probe measures the smallest range of beam angles and thus is closest to constant flux across the probe.

uniformly-cooled.

Anemometer probes with the anemometer array far enough away from the nozzle can be considered pseudo-uniformly cooled due to the smoothness of the beams central peak. The middle-radius and centre-line anemometer elements are pseudo-uniformly cooled 147mm from the nozzle throat as the probes measure the same signal amplitude (shown in figure 3.7) for the most peaked beam conditions. The remaining probe positions (the centre-line and middle-radius probes closer than 147mm) are considered to be non-uniformly cooled as the signals they record differ. These positions are not used to directly reflect beam interactions to minimise errors.

The process of calibrating signals from non-uniformly cooled probes is computa-

tionally intensive and in general not possible. The non-uniformly cooled anemometer signals also suffer varying degrees of background particle based errors. Close to the nozzle, perturbations due to scattering of the beam and the background particles is smallest. Data taken too close to the nozzle is corrupted as a result of catastrophic cooling of the probe as seen previously in figure 2.10. The non-uniformly cooled anemometer probe signal that is minimally affected by the increasing background pressure and still a valid representation of beam properties is then somewhere close, but not too close to the nozzle. Revisiting figure 3.3, the anemometer probe data taken with the anemometer array 32mm from the nozzle conforms best to these constraints. A time series of data $\Upsilon(t)$ (where $\Upsilon$ is pronounced 'Upsilon') is defined to be $1821 \times \mathrm{P_b}$ measured by the centre-line anemometer probe 32mm from the nozzle.[1]

$\Upsilon(t)$ is a background density independent measure of the beam subject only to the errors resulting from non-uniform cooling of the probe. $\Upsilon(t)$ is used to extrapolate the beam profile characterisation beyond the 2ms to 5ms analysis period. The beam profile is modeled using parameters of on-axis beam flux, and the angle where the beam flux is half the on-axis flux. The magnitude of these parameters was then related to values of $\Upsilon(t)$ for times when the measured beam profile parameters are valid (i.e. the 2ms to 5ms analysis period). By inverting this relationship it is then possible to generate beam profile parameters at later times using $\Upsilon(t)$ when their direct measurement is no longer possible due to the increased background density. At these times $\Upsilon(t)$ has no dependence on the background density. $\Upsilon(t)$ then allows

[1]The factor of 1821 converts $\mathrm{P_b}$ from units of Watts to arbitrary units. This is an artifact of early analysis using $\Upsilon(t)$ values that were not scaled to SI units. As $\Upsilon(t)$ will be eventually related to beam properties without reference to power units the factor is removed in later signal scaling steps.

the integration of the uniformly-cooled anemometer probe data for the entire shot and allows these signals to be scaled using N determined by the plenum pressure change.

A source of uncertainty in $\Upsilon(t)$ is the disparity between the target plenum pressure for a shot and the actual plenum pressure the filling system achieves. This uncertainty can be accounted for if beam data for the target pressure is required. Figure 3.9 shows the actual start pressure for shots with a target pressure 1400 Torr and 400 Torr to show the variation. To correct for this, a linear scaling of the measured $\Upsilon(t)$ values will be performed on the signals using the actual starting plenum pressure $p_{\text{start}}$ and the target plenum pressure $p_{\text{target}}$ to obtain a scaled measurement $\Upsilon^{\star}(t)$ such that:

$$\Upsilon^{\star}(t) = \Upsilon(t)\,\frac{p_{\text{target}}}{p_{\text{start}}} \tag{3.18}$$

To demonstrate the effectiveness of this approach figure 3.10 shows $\Upsilon(t)$ values unscaled for start pressure variations and the corresponding $\Upsilon^{\star}(t)$ values. $\Upsilon^{\star}(t)$ values are seen to vary with drive voltage as would be expected from the plenum pressure difference data shown in figure 2.5. This method of scaling measured signals to the target plenum pressure will also be applied to the uniformly-cooled anemometer probe data before establishing the angular beam flux profile. To simplify annotation $\Upsilon(t)$ will be used to represent the start pressure scaled $\Upsilon(t)$ value in the rest of the thesis and the $\star$ superscript omitted. Note in figure 3.10 that 320 Hz and 1 kHz oscillations can be seen. The 1kHz signal is observable at all distances from the nozzle implying that it is a real property of the beam. The 320 Hz oscillation is only seen near to the nozzle. The cause of this oscillation is considered to be a mechani-

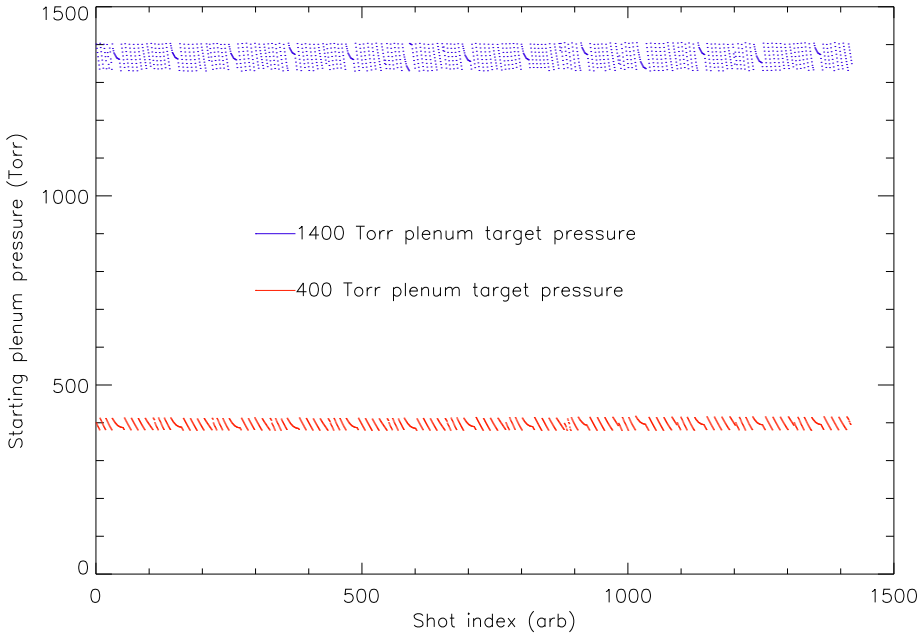


Figure 3.9: Start pressures for shots with 1400 Torr plenum pressure target and 400 Torr plenum pressure target. The variation is a result of hysteresis in the plenum filling system. These variations need to be accounted for to remove associated errors in later beam angle analysis.

cal oscillation in the lamp filament resulting from momentum transfer between the beam and the filament. This supports the hypothesis proposed in section 2.5 that plenum bleeds with the anemometer array close to the nozzle stimulated a vibrational mode in the probe. Mechanical fatiguing due to this vibration is considered the likely cause of probe failures.

The non-uniformly cooled probe data for positions other than the designated $\Upsilon(t)$ series are still of some use without scaling the signal magnitude. In order to determine the beam velocity, phase measurements of the modulated beam are required. It is possible that the signal perturbations due to the non uniform cooling of the

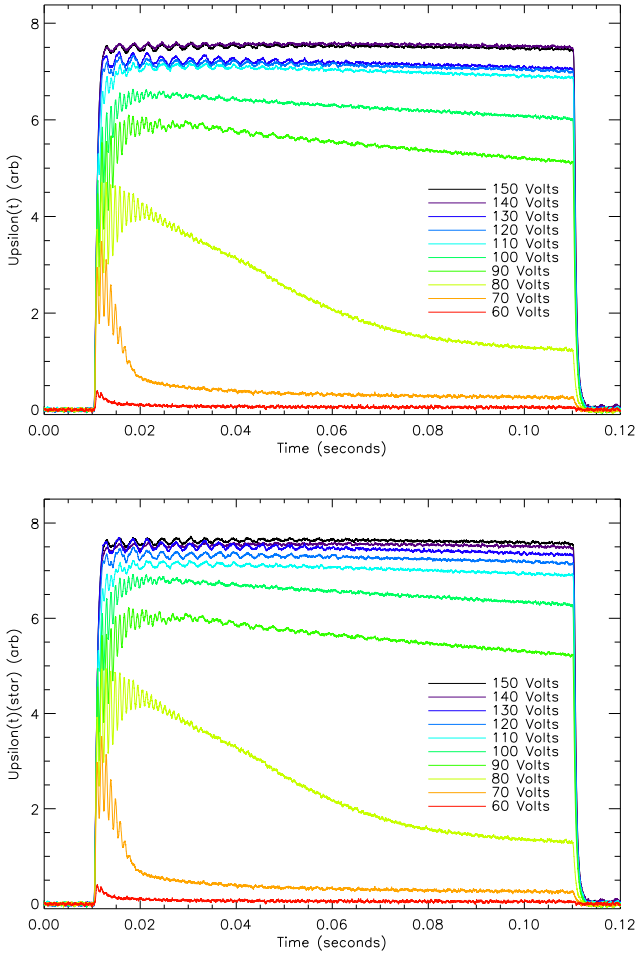


Figure 3.10: The upper plot shows $\Upsilon(t)$ measured with a target plenum pressure of 1400 Torr and various DC drive voltages. The lower plot shows the corresponding scaled $\Upsilon^{\star}(t)$ values. Note that the variation of $\Upsilon(t)$ with increasing drive voltages is unclear due to uncertainties in the starting plenum pressure. The $\Upsilon^{\star}(t)$ values, once scaled to account for these uncertainties, show clearly a more regular increase with drive voltage as expected. The 320Hz oscillation seen at higher drive voltages appears to be filament vibrations and not a real part of the beam flux. At lower drive voltages an oscillation around 1kHz is observed that appears to be a real feature of the beam. 1 kHz is an audible mechanical resonance in the valve. As this method of scaling is now justified the $\star$ superscript will be omitted in the rest of the thesis.

anemometer probes will not significantly distort the detected phase of the beam modulation. To determine if distortion of the detected phase due to non-uniform cooling can be ignored, a velocity determination based upon the centre-line anemometer probe signals (maximally susceptible to possible non uniform cooling distortions of measured phase) and the middle-radius anemometer probe signals (less susceptible to possible non-uniform cooling distortions of measured phase) will be conducted and compared. If non-uniform probe cooling effects do not change the determined velocity, the distortion of measured signal phase due to non-uniform cooling of the probe will be considered to be negligible.

## 3.5 $\theta$ dependence of the beam flux

To determine the $\theta$ dependence of the beam flux $\Gamma(t, \theta)$ a function that establishes the flux profile based upon uniformly-cooled anemometer probe data is required. Before the determined profile can be scaled to a beam flux this profile must first be mapped to $\Upsilon(t)$ so that the profile can be generated for all times in the pulse. The $\theta$ dependence is explored by varying the distance between the anemometer array and the nozzle $d_a$. Table 3.1 shows the available uniformly-cooled probe data representing beam angles $\theta$ as shown. This table includes the outer-radius anemometer probe data at all the anemometer array positions, as well as the centre-line and middle-radius anemometer probe data measured with the anemometer array 147mm from the nozzle.

| $d_a$ (mm) | $d_p$ (mm) | $\theta$ (degrees) | Probe Position | Minimum Kn |
|---|---|---|---|---|
| 32 | 13 | 22.11 | outer-radius | 14.2 |
| 37 | 13 | 19.36 | outer-radius | 13.6 |
| 47 | 13 | 15.46 | outer-radius | 11.6 |
| 57 | 13 | 12.85 | outer-radius | 10.4 |
| 67 | 13 | 10.98 | outer-radius | 9.92 |
| 77 | 13 | 9.58 | outer-radius | 10.0 |
| 87 | 13 | 8.50 | outer-radius | 10.5 |
| 97 | 13 | 7.63 | outer-radius | 11.3 |
| 107 | 13 | 6.93 | outer-radius | 12.3 |
| 117 | 13 | 6.34 | outer-radius | 13.4 |
| 127 | 13 | 5.84 | outer-radius | 14.6 |
| 137 | 13 | 5.42 | outer-radius | 16.0 |
| 147 | 13 | 5.05 | outer-radius | 17.6 |
| 147 | 7.5 | 2.92 | middle-radius | 13.9 |
| 147 | 0 | 0.00 | centre-line | 12.1 |

Table 3.1: The available uniformly-cooled probe data to investigate the $\theta$ dependence of the beam flux. The Knudsen values relate to the anemometer signals functional dependence discussed on page 30.

A decrease in detected beam flux occurs with increasing distance between the anemometer array and the nozzle. This is due to the interplay between the area over which the probes measures particle fluxes, and the increasing surface area over which the beam flux is spread. The detected signal is a ratio of areas, having an inverse square relationship to the distance between the probe and the nozzle. Comparison of signals at different angles (and consequently measured at different distances from the nozzle) requires the product of the beam probe signal and the square of the distance between the probe and the nozzle in millimeters to be used. This scales the detected signals so $\theta$ dependencies are preserved while removing variations due to the distance from each probe to the nozzle $d$. The centre of each probe is taken to be the probe position reference point for the measurement of $d$. $d_p$ is defined to be the distance between the intersection point of the beam axis with the plane of

the anemometer array and the probe position reference point (see figure 3.8 for the required dimensions). $d$ is then:

$$d = \sqrt{(d_a)^2 + (d_p)^2} \tag{3.19}$$

The distance corrected power signal $\mathrm{P_C}$ is then:

$$\mathrm{P_C} = 1821 \times \mathrm{P_b} \times d^2 \tag{3.20}$$

$\mathrm{P_C}$ can then be attributed to a beam angle $\theta$ shown in table 3.1.

The $\mathrm{P_C}$ profile is used to create a profile fitting function $\gamma(\theta)$. The function $\gamma(\theta)$ is assumed to have either a Gaussian type profile $\gamma_g(\theta)$, a Lorentzian type profile $\gamma_l(\theta)$ or a hybrid of both the Lorentzian and Gaussian functions $\gamma_h(\theta)$. The Gaussian type profile is defined to be:

$$\gamma_g(\theta) = A_g \, e^{\left(-\frac{1}{2}\left(\frac{\theta}{\theta_g}\right)^2\right)} \tag{3.21}$$

and the Lorentzian type profile is defined as:

$$\gamma_l = \frac{A_l}{\left(\frac{\theta}{\theta_l}\right)^2 + 1} \tag{3.22}$$

where $A_g$ and $A_l$ are the on axis beam fluxes for each type of fit, $\theta_g$ and $\theta_l$ determine the width of the profiles. Normalising constants of these profiles are not required as the final time and angle integral of the profile functions will be scaled using N from the plenum pressure data. $A_g$, $\theta_g$, $A_l$ and $\theta_l$ were found using the IDL curvefit routine. Comparing the fitted profiles to the data demonstrates some undesirable features of the Gaussian profile and the Lorentzian profile. The Gaussian profile drops away too rapidly with large beam angles, and the Lorentzian profile

over-estimates the on-axis value. A hybrid function was created by averaging the determined Gaussian and Lorentzian profiles. The equation of this hybrid function is:

$$\gamma_h(\theta) = \frac{\gamma_g + \gamma_l}{2} \tag{3.23}$$

The profile $\gamma_h$ is shown in figure 3.11 to fit the measured data better than a Lorentzian profile or Gaussian profile alone. Fitting the hybrid profile to data from shots with a range of plenum pressures and 150 Volts drive is shown in figure 3.12 to demonstrate the veracity of the hybrid fitted profile for a range of conditions. As the drive voltage is lowered the accuracy of the fit of the hybrid function is reduced. For a drive of 70 Volts shown in figure 3.13 the beam angle profile appears to be a little more Lorentzian in nature compared with profiles for 150 Volt drive. However the fit of the hybrid profile and the Lorentzian are seen to have comparable accuracy, so to simplify analysis the hybrid profile will be used for all drive voltages.

By fitting hybrid functions to a single time point 2 ms from the monitor reference point for shots with DC drive, the angle where flux is half the on axis value can be tabulated. Figure 3.14 shows these angles for various DC drives and plenum pressures. From the hybrid fit function the flux within a given beam angle can also be determined. To do this the profile must be rotated around the axis to form a surface, and $\gamma_h$ integrated over this surface. The beam is assumed to be circularly symmetrical in rotation. The relationship between $\gamma_h(\theta)$ and $\Gamma(t, \theta)$ at a specific time t is:

$$\Gamma(t, \theta) = \alpha\, \gamma_h(\theta) \tag{3.24}$$

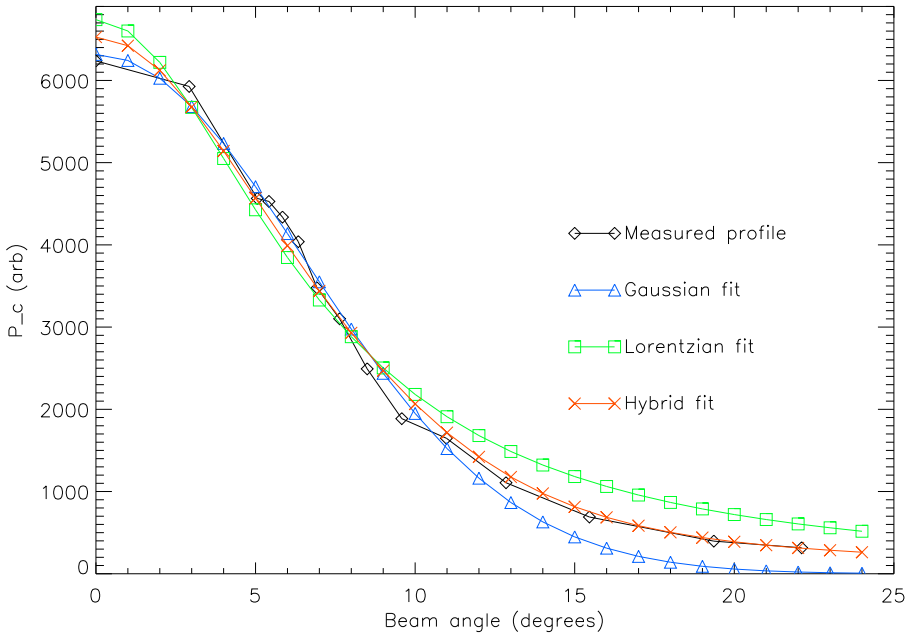


Figure 3.11: $P_C$ profile for a plenum pressure of 1400 Torr and a drive of 150 Volts. The Lorentzian and Gaussian fit functions are shown. The average of these fitted functions labeled 'hybrid' approximates the measured data the best.

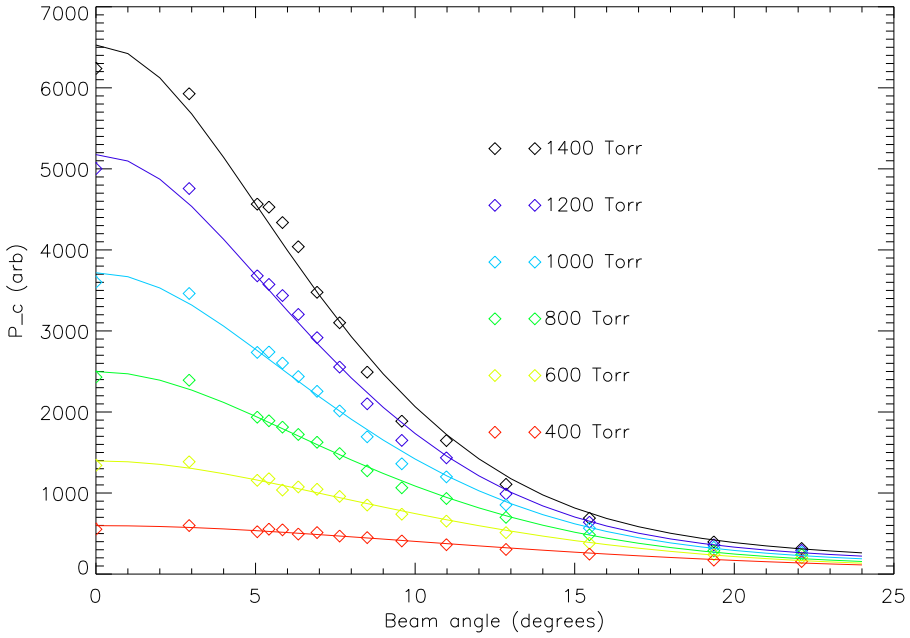


Figure 3.12: $P_C$ profiles for 150 volt drive and a range of plenum pressures. The fitted hybrid functions are overlaid on data points as trend lines.

Where $\alpha$ is a constant scaling $\gamma_h(\theta)$ to a flux as discussed in section 2.4. The time dependence of $\Gamma(t, \theta)$ is achieved by time varying the coefficients of $\gamma_h$. The $\alpha$ value cannot be determined until $\gamma_h(\theta)$ values can be generated free from errors due to increased background densities for the entire pulse. This is because the number of particles N is only known for the entire pulse. Defining a parameter $\beta(\theta)$ as the fraction of the beam flux enclosed by a cone with axis aligned to the beam axis and apex at the nozzle throat provides some insight into the beam density profile. The angle $\theta$ is the angle at which the conical surface intersects with the beam axis. $\beta(\theta)$ can be calculated without knowing $\alpha$, as it is a ratio of integrals with equivalent constants. The value of $\beta(\theta)$ was calculated using a ratio of the RHS of equation

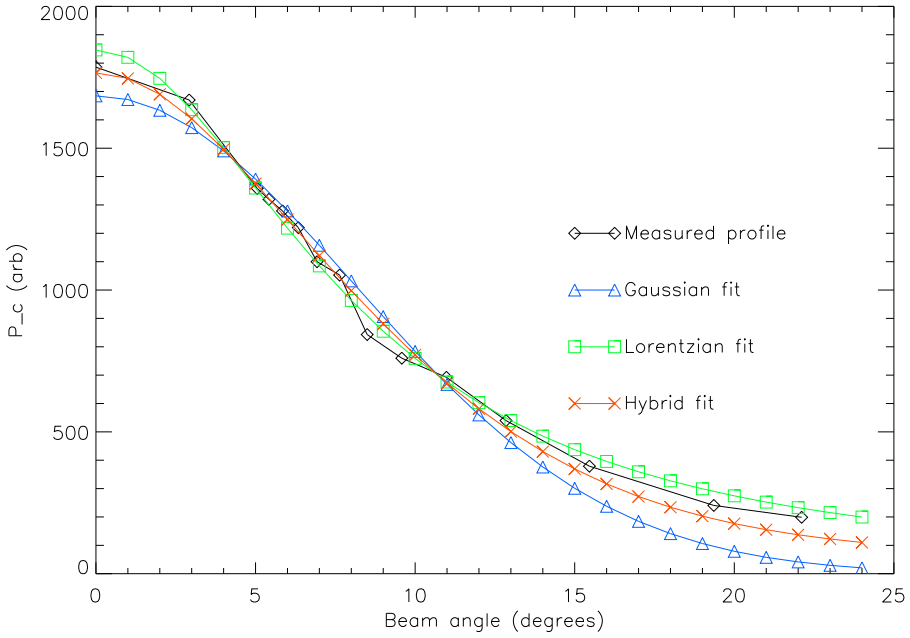


Figure 3.13: $P_C$ profile for 1400 Torr plenum pressure with 70 Volts drive. As the drive is reduced the profile becomes more Lorentzian. The accuracy of the hybrid profile and Lorentzian profile to match measured data for low drive is considered to be comparable.

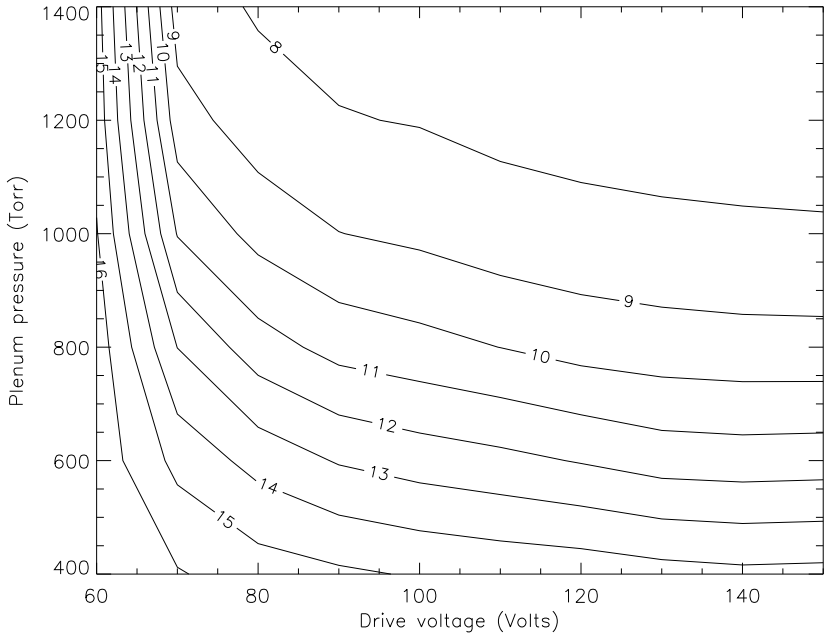


Figure 3.14: Shown is the $\theta$ values on contour lines where $\gamma_h(\theta)$ is half the on axis value at the start of the analysis period for DC shots with a range of plenum pressures and drive voltages.

3.3 with the numerator integral performed from 0 to $\theta$. That is:

$$\beta(\theta) = \frac{\int_0^\theta \gamma_h(\phi) \sin\phi \, d\phi}{\int_0^{32} \gamma_h(\phi) \sin\phi \, d\phi} \tag{3.25}$$

For the specific case of 1400 Torr plenum pressure and 150 Volts DC drive, figure 3.15 shows $\beta(\theta)$.

Approximating the beam flux profile for times when the hybrid functions are contaminated by background particle interactions requires assumptions to be made about the physical system. One approach (which I do not do) is to assume that $\Upsilon(t)$ needs to be related to $\gamma_h(\theta)$ for each plenum pressure and drive voltage condition in order to generate $\gamma_h(\theta)$ from $\Upsilon(t)$. Insufficient data is available to do this for some cases of drive voltage and plenum pressure (especially modulated shots) where

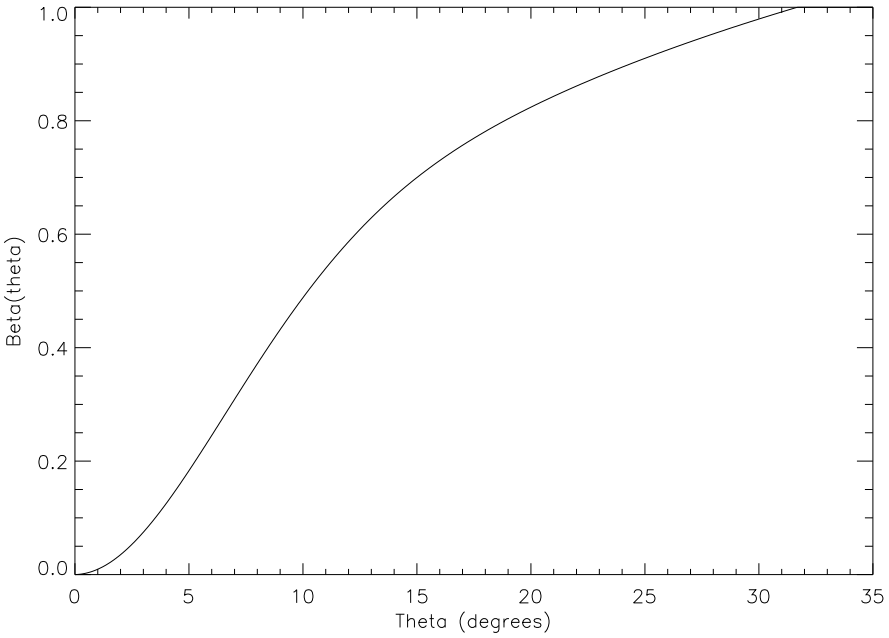


Figure 3.15: Shown is $\beta(\theta)$, the ratio of beam particles enclosed by the conical surface lying $\theta$ degrees from the beam axis, for 1400 Torr plenum pressure and 150 Volts drive.

a particular value of $\Upsilon(t)$ only occurs outside the analysis period. A more general approach (which I will use) assumes $\gamma_h(\theta)$ can be determined by the $\Upsilon(t)$ value without dependence on the plenum pressure and drive voltage. The validity of this assumption will effectively be tested by the linearity of the relationship between N (from the plenum pressure difference) and $2\pi \mathrm{t_s} \sum_{\text{all times}} \int_0^{32} \Gamma(t,\theta)\, \sin(\theta)\, d\theta$ derived from $\Upsilon(t)$ values without considering plenum pressure and piezo drive voltage.

Meaningful analysis using the hybrid fit functions requires limiting the analysis period to times where beam-background interactions are negligible. This is justified by a plot of $2\pi \int_0^{32} \gamma_h(\theta) \sin\theta\, d\theta$ (subject to errors) and the corresponding $\Upsilon(t)$ values (free from background errors) plotted against each other for all available times in the upper plot of figure 3.16. It is difficult to discern any meaningful trends from this data. By only considering the analysis period deemed to be free of beam-background interactions, the relationship is shown in the lower plot is achieved. Some structure is observed in this plot, suggesting that $\Upsilon(t)$ does not fully describe $2\pi \int_0^{32} \gamma_h(\theta) \sin\theta\, d\theta$.

## 3.6 Determining $\alpha$

To determine $\alpha$ a set of co-efficient equations need to be defined that generate the coefficients of $\gamma_h$ from $\Upsilon(t)$. The four functions required are $G_1$, $G_2$, $G_3$, $G_4$, all

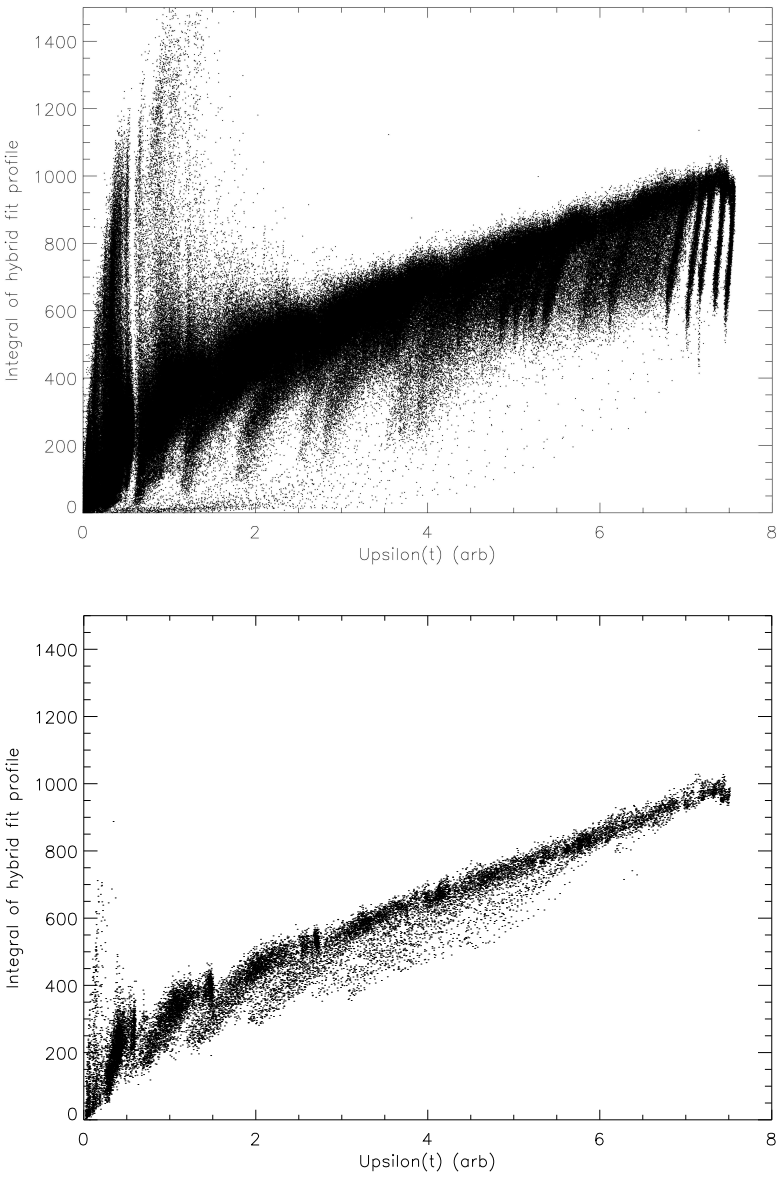


Figure 3.16: Shown in the upper plot is the relationship between $2\pi \int_0^{32} \gamma_h(\theta) \sin\theta \, d\theta$ and $\Upsilon(t)$ for all times over the 100ms pulses for all shot conditions recorded. This data includes the measurements determined to be subject to errors resulting from background particle interactions with the beam. The lower plot shows a truncation of data shown in the upper plot to only consider data for the 3ms analysis period deemed to be relatively free of beam-background interactions.

dependent on $\Upsilon(t)$ such that:

$$A_g(t) = G_1(\Upsilon(t)) \tag{3.26}$$

$$\theta_g(t) = G_2(\Upsilon(t)) \tag{3.27}$$

$$A_l(t) = G_3(\Upsilon(t)) \tag{3.28}$$

$$\theta_l(t) = G_4(\Upsilon(t)) \tag{3.29}$$

For the fitted flux to be determined from equation 3.23 scaling between the anemometer signals and the beam flux must be determined. Modelling of the hybrid function coefficients based upon $\Upsilon(t)$ when background effects are negligible allows $\Upsilon(t)$ to be used to generate the hybrid fit coefficients when background interactions prevent their direct measurement. To do this each of the hybrid fit coefficients is plotted against $\Upsilon(t)$ and a functional relationship determined. Figure 3.17 shows the functional fit for $\Upsilon(t)$ versus $A_g$. Similarly figures 3.18, 3.19, 3.20 fit arbitrary functions to the observed trends in $A_l$, $\theta_g$, and $\theta_l$ respectively.

Now that functions have been attained to derive the hybrid fit coefficients based upon the $\Upsilon(t)$ value, evaluating $2\pi \int_0^{32} \gamma_h(\theta) \sin\theta \, d\theta$ based upon $\Upsilon(t)$ values can be compared to the measured values of the lower plot in figure 3.16. This allows an estimation of the errors present in $2\pi \int_0^{32} \gamma_h(\theta) \sin\theta \, d\theta$ based on $\Upsilon(t)$ values. In the upper plot of figure 3.21 the measured integral of the profiles in the valid analysis period is shown with the $\Upsilon(t)$ based profile integral overlaid as a trend line. The error envelope shown is derived from the mean of the absolute error between values of $2\pi \int_0^{32} \gamma_h(\theta) \sin\theta \, d\theta$ based on $\Upsilon(t)$ values and the 100 adjacent measured values of $\int_0^{32} \gamma_h(\theta) \sin\theta \, d\theta$ referenced to $\Upsilon(t)$ values. The lower plot shows this error envelope

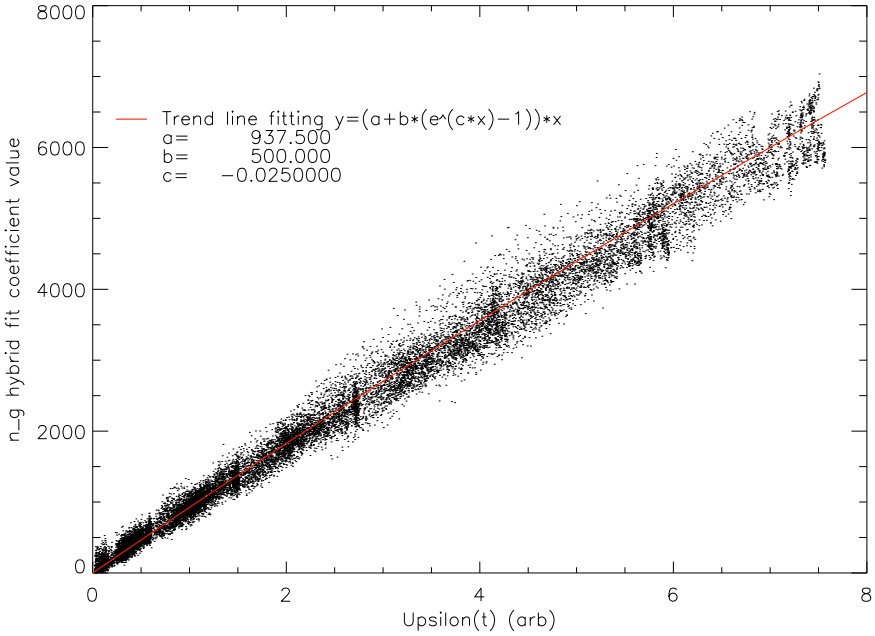


Figure 3.17: The $\Upsilon(t)$ value plotted against the hybrid fit coefficient $A_g$. An arbitrary function is fitted to be used in modeling the hybrid function based upon $\Upsilon(t)$.

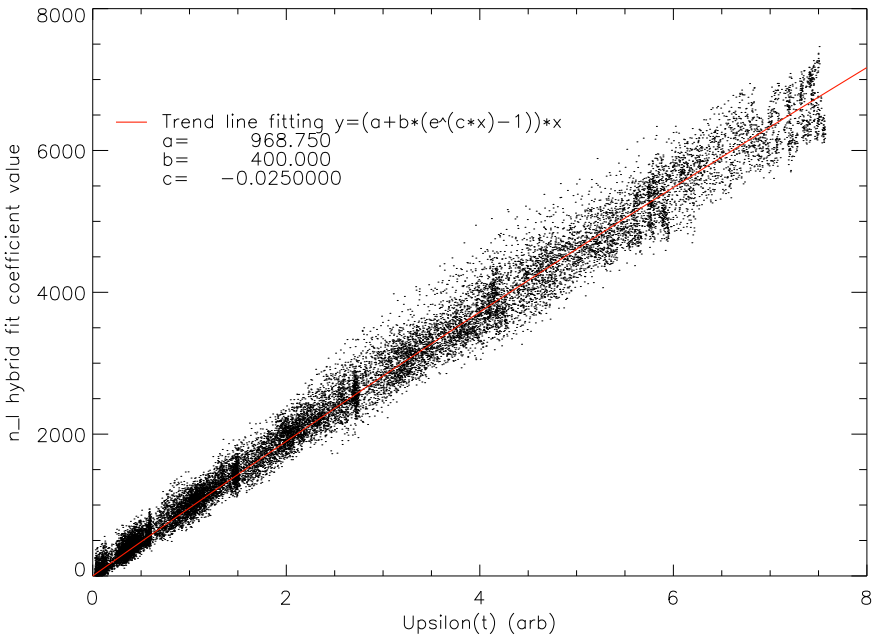


Figure 3.18: The $\Upsilon(t)$ value plotted against the hybrid fit coefficient $A_l$. An arbitrary function is fitted to be used in modeling the hybrid function based upon $\Upsilon(t)$.

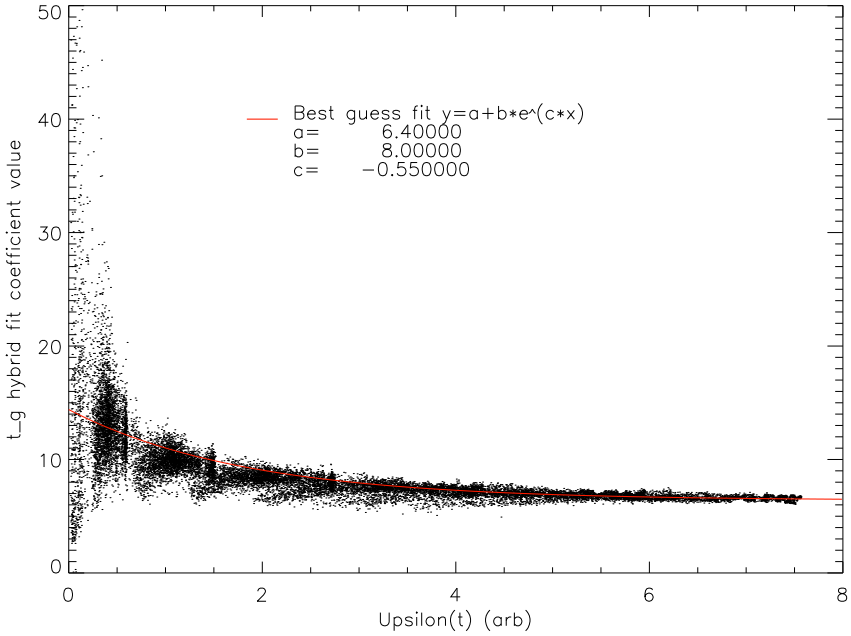


Figure 3.19: The $\Upsilon(t)$ value plotted against the hybrid fit coefficient $\theta_g$. An arbitrary function is fitted to be used in modeling the hybrid function based upon $\Upsilon(t)$.

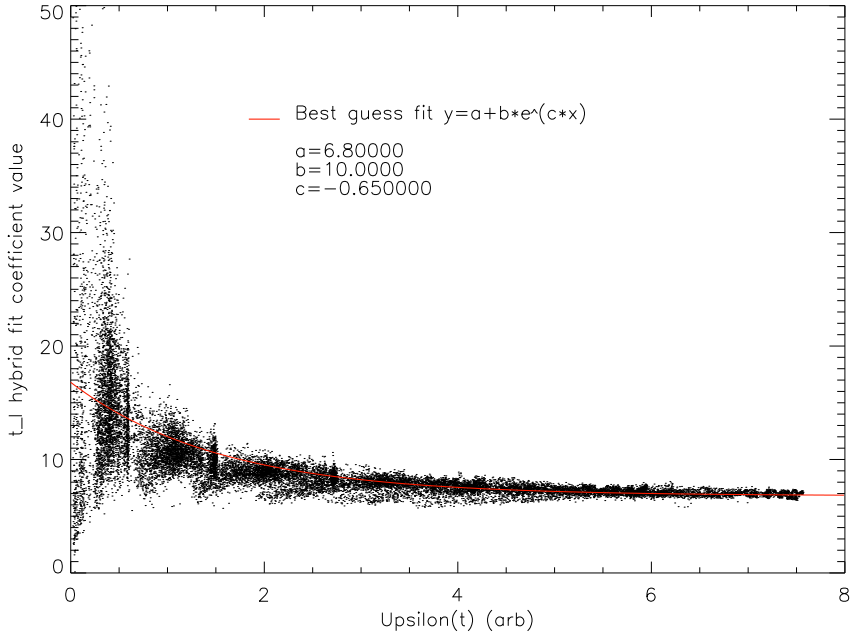


Figure 3.20: The $\Upsilon(t)$ value plotted against the hybrid fit coefficient $\theta_l$. An arbitrary function is fitted to be used in modeling the hybrid function based upon $\Upsilon(t)$.

as an absolute error plotted against the $\Upsilon(t)$ values.

The $\Upsilon(t)$ based integrals of the modeled hybrid function can now be compared to the measured plenum particle loss N. This establishes the veracity of the approach. Error estimations are included by averaging the absolute errors of the $\Upsilon(t)$ values for each shot from the error values in the lower plot of 3.21. The scaling coefficient $\alpha$ is determined from the linear relationship between $2\pi \mathrm{t_s} \sum_{\text{all times}} \int_0^{32} \gamma_h(\theta) \sin\theta \, d\theta$ and the measured N value. Figure 3.22 shows this relationship. From equation 3.4 and equation 3.24 the value of alpha can be approximated using the gradient of the least squares fitted trend line in figure 3.22 of $1.035 \times 10^{-18}$. The value of $\alpha$ is the inverse of this gradient:

$$\alpha = 9.663 \times 10^{17} \tag{3.30}$$

The determined $\alpha$ is required to scale the time series of $\gamma_h$ values to establish $\Gamma(t, \theta)$. $\Gamma(t, \theta)$ then represents a particles flux. To convert this flux into a beam density the beam velocity must be determined. This section is concluded by summarising the functional relationships between $\Upsilon(t)$ and the hybrid fit coefficients found to be:

$$A_g(t) = 937 + 500\,(e^{(-0.025*\Upsilon(t))} - 1)\,\Upsilon(t) \tag{3.31}$$

$$\theta_g(t) = 6.4 + 8\,e^{(-0.55\,\Upsilon(t))} \tag{3.32}$$

$$A_l(t) = 969 + 400\,(e^{(-0.025*\Upsilon(t))} - 1)\,\Upsilon(t) \tag{3.33}$$

$$\theta_l(t) = 6.8 + 10\,e^{(-0.65\,\Upsilon(t))} \tag{3.34}$$

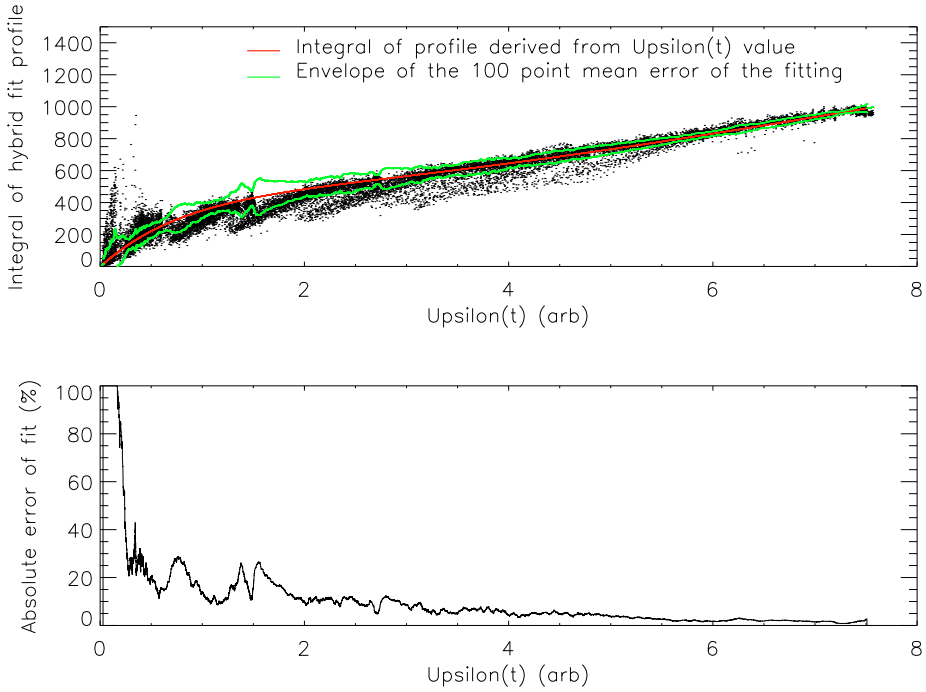


Figure 3.21: The upper plot shows the relationship between $2\pi \int_0^{32} \gamma_h(\theta) \sin\theta \, d\theta$ and $\Upsilon(t)$ for the analysis period. Overlaid as a trend line is the $2\pi \int_0^{32} \gamma_h(\theta) \sin\theta \, d\theta$ values based upon $\Upsilon(t)$. The error envelope shown is derived from the mean of the absolute error between the $\Upsilon(t)$ based values of $2\pi \int_0^{32} \gamma_h(\theta) \sin\theta \, d\theta$ and the 100 adjacent measured values of $2\pi \int_0^{32} \gamma_h(\theta) \sin\theta \, d\theta$. The lower plot shows this error envelope plotted against the $\Upsilon(t)$ values.

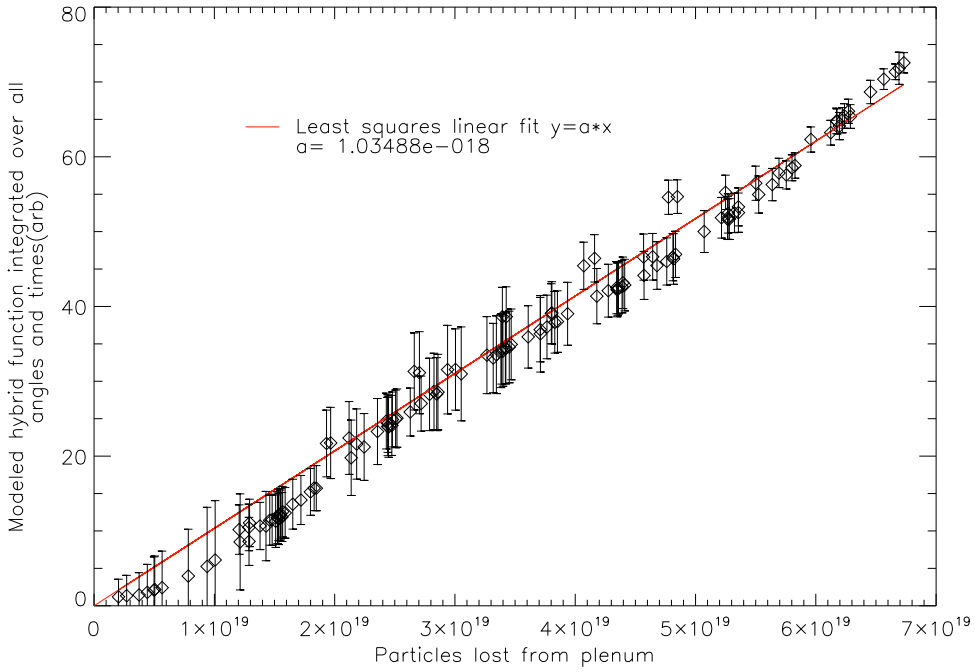


Figure 3.22: The integral of the beam profile over the duration of the shot $2\pi t_s \sum_{\text{all times}} \int_0^{32} \gamma_h(\theta) \sin\theta \, d\theta$ using the $\Upsilon(t)$ modeled hybrid fit coefficients plotted against the total number of particles lost from the plenum N for all of the characterised shot conditions. The inverse of the fitted gradient gives the value of $\alpha$.

## 3.7 Beam velocity

Beam velocity is required to determine the beam density. The approach used to determine beam velocity exploits the ability to modulate the molecular beam. By modulating the beam with a sinusoidal drive voltage the beam flux is likewise modulated. By measuring the phase of beam modulation at different distances from the nozzle the average velocity of the beam is found. The natural 1kHz ring of the beam at low drive voltage was not used for velocity determination as there was no reference 1kHz signal on the monitor signal. Instead the 1kHz modulated shots were used as the measured 1kHz modulation of the beam can be referenced to the piezo drive modulation and a phase delay can be determined for a single shot. The velocity of the beam is considered to be relatively unchanged by valve modulation as the observed anemometer signal at 147mm from the nozzle has a similar shape to the signal at 32mm. If modulating the beam introduced a significant variation in beam velocity then the observed signal shape would have a dependency upon the displacement of the anemometer array from the jet. No evidence of this was observed.

For velocity determination the modulation frequency must be as high as possible in order to avoid contaminating the phase measurements with beam-background interactions. The maximum visibility of beam modulation occurs at 1kHz corresponding to the mechanical resonance of the valve. Driving the valve at higher frequencies than this results in a considerable reduction in the visibility of the beam modulation. Unfortunately when recording data I did not optimise the phase of the modulated drive voltage to be in phase with the ringing response of the valve due to the initial opening square wave. As a result the period of valid analysis was further

restricted by phase variations resulting from the valve modulation shifting from the ringing phase at the instant of opening to the phase of the modulated drive voltage. The interference between these out of phase drives can be seen as a reduction of modulation amplitude at the beginning of the pulse in figure 3.23. The analysis of the signals was restricted to the time period following the decay of the ringing response, and before the onset of background perturbations in the test tank. To determine the optimum time period to use for velocity measurements the signals for 1400 Torr plenum pressure and 85-120 Volts 1kHz modulated drive at a range of anemometer array positions were acquired. Shown in the upper plot of figure 3.23 is the piezo valve drive monitor signal and an anemometer signal as an example of data acquired at each position. A slice of time with length equal to the period of modulation was taken simultaneously from the monitor signal and the anemometer signal. The IDL Fast Fourier Transform algorithm was then used to determine the phase of 1kHz signal present on each. By subtracting the phase of the anemometer signal from the phase of the drive monitor signal a phase difference is obtained. By scanning the start point of the time slice to be analysed, the phase difference can be calculated over a range of points in the available data. The result of this calculation of phase difference is shown in the lower plot of figure 3.23.

Based upon data in figure 3.23 an ideal analysis period was determined for velocity calculations and data from this period displayed in higher time resolution in figure 3.24. This data highlights the uncertainty in phase difference determination.

To increase the accuracy of velocity measurement, statistical methods were used

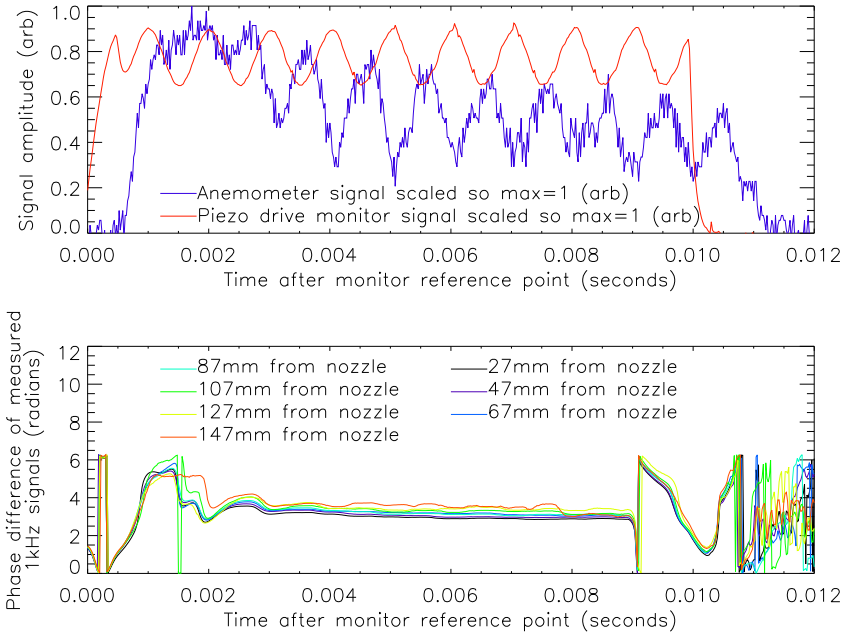


Figure 3.23: The upper plot shows a sample of the drive voltage monitor signal and anemometer signal for an arbitrary shot. The Fast Fourier Transform of these signals at a given time allows the phase of the modulated frequency on each to be subtracted. The lower plot shows this phase difference plotted for anemometer probes at a range of distances from the nozzle with equivalent plenum pressure and drive voltage. Notice the interference between the valve's ringing response and the modulated drive reducing modulated signal visibility early in the pulse.

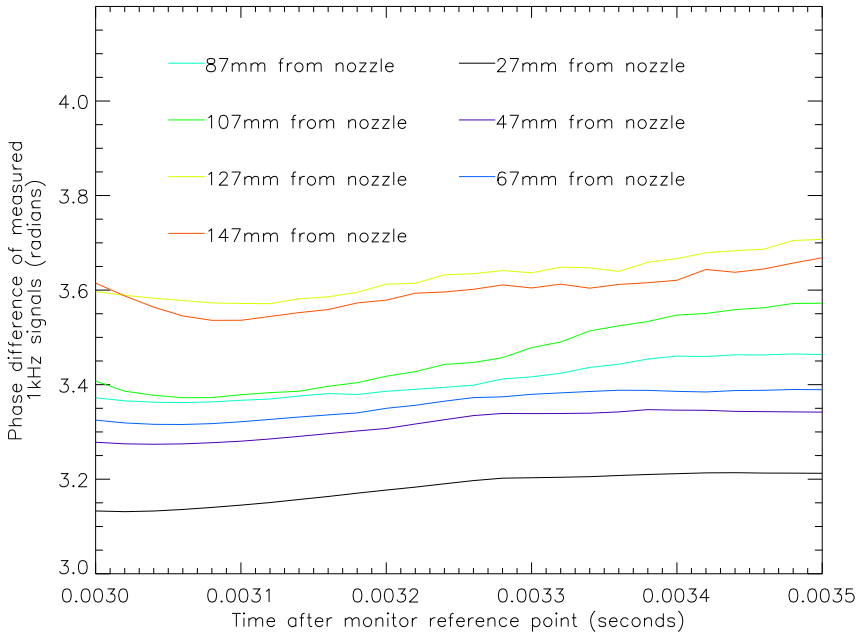


Figure 3.24: Shown is an expanded view of data from figure 3.23 in the time range to be used in the beam velocity determination. Even in this region significant phase noise is present, particularly in signals further from the nozzle.

to average out uncertainties in calculated phase differences. By automating the acquisition of data it was possible to statistically operate on large data sets. For the velocity determination alone 12000 shots containing 3 anemometer channels of data were collected. These shots were 10 ms long pulses and the plenum pressure was allowed to fall without filling between the shots. As a result a pressure scan was conducted where adjacent datum points had such similar plenum pressures that averaging was possible in the local region of a desired value for a large range of values.

Shown in figure 3.25 is the phase difference measured on the centre-line anemometer element during the analysis period for a range of plenum pressures and anemometer array positions. Each point in the middle of the graph represents the average of 100 local phase difference values. Note the tails of the graph where averaging data was no longer possible and the original uncertainty in the measured phase difference can be seen. The error bars on this graph represent the uncertainty in the determined local mean [21]. Note that the change in measured phase difference, with respect to the anemometer array position, is approximately linear.

The averaged phase difference between anemometer array positions was then used to estimate the average modulated beam velocity. The phase difference $\phi$ at a distance z from the nozzle includes both the signal delay from the beam time of flight and the inherent phase delays associated with the operation of the valve. By only considering the change in average phase difference between the array positions, the valve delay is effectively removed from the analysis. The predicted velocity $v$ is then calculated using the gradient m of a line that best fits to a plot of $\phi$ versus z. $v$ is

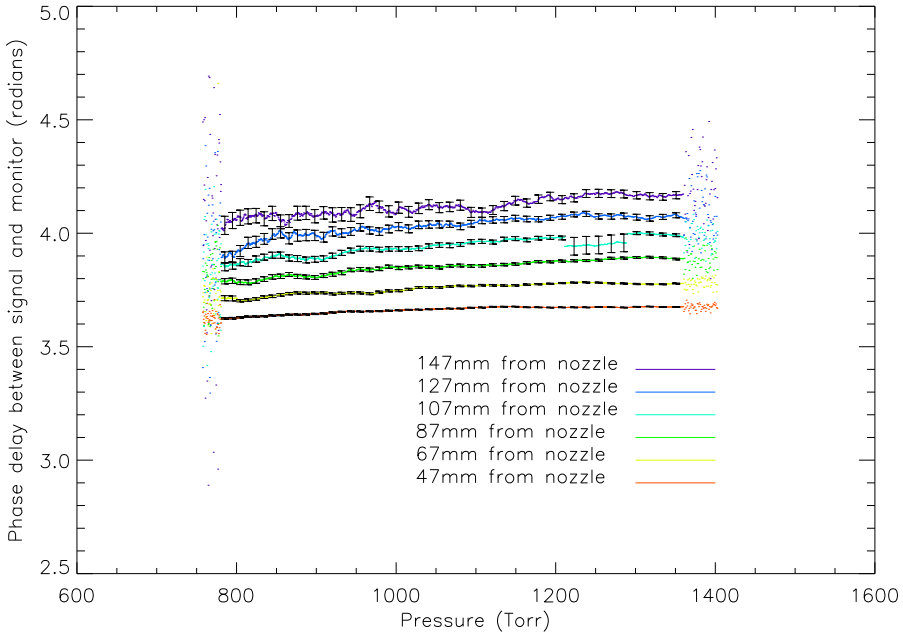


Figure 3.25: Shown is the measured phase difference on the centre-line anemometer probe for a range of anemometer array positions. The mean value of 100 shots about the reference pressure is shown. The error bars are calculated from the uncertainty of the mean over these shots. The tails of the plot have not been averaged and show the variation in raw data.

then given by

$$v = \frac{2\pi f}{m} \tag{3.35}$$

where f is the modulation frequency. Figure 3.26 shows the result of the velocity calculation based upon the gradient of the averaged phase difference data from figure 3.25. The error in the determined velocity was established using phases from 100 adjacent phase data points. These 'points' actually include six phase values associated with the phase data at each anemometer array position. For each point a velocity was determined. The phases were then averaged between the 100 data points, and the velocity again found. By averaging the absolute error between the phase-averaged velocity measurement and the 100 single point velocity measurements, the magnitude of the error bars were established. Figure 3.26 estimates the exit velocity of the beam to be $1250 \pm 50$ m/s. The error in the measurement, particularly at low plenum pressure, prevents investigation of the beam velocity dependence on plenum pressure.

Attempting to do a similar analysis with the middle-radius anemometer element highlights the detrimental effects of noise on this measurement. Figure 3.27 shows how the uncertainties in phase difference have increased and accordingly the velocity determined in the upper plot of figure 3.28 has much larger error bars. It is pleasing to note that in spite of the increased errors in the middle-radius anemometer derived velocity, the bounded value agrees with the velocity derived from the centre-line anemometer element, shown in the lower plot of figure 3.28. This implies that non-uniformly cooling the anemometer probes does not appreciably perturb the detected phase of the modulated flux.

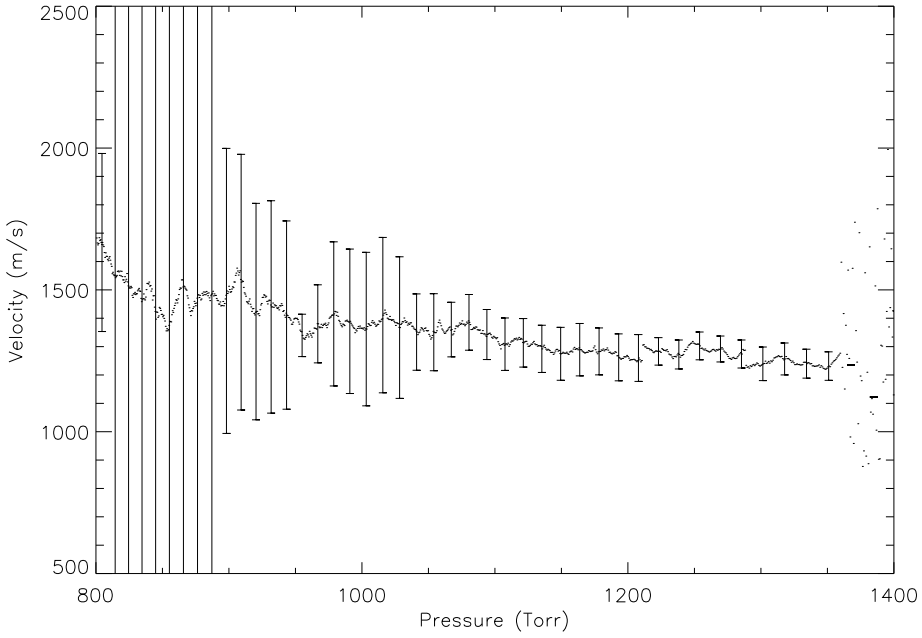


Figure 3.26: The beam velocity calculated from the averaged centre-line anemometer probe phase difference data shown in figure 3.25. The error bars show the uncertainty of the determined velocity based upon raw data in the range of phase differences used to determine the average value. A velocity of $1250 \pm 50$ m/s is measured. The error bars prevent conclusive comment to be made about the variation of beam velocity with plenum pressure.

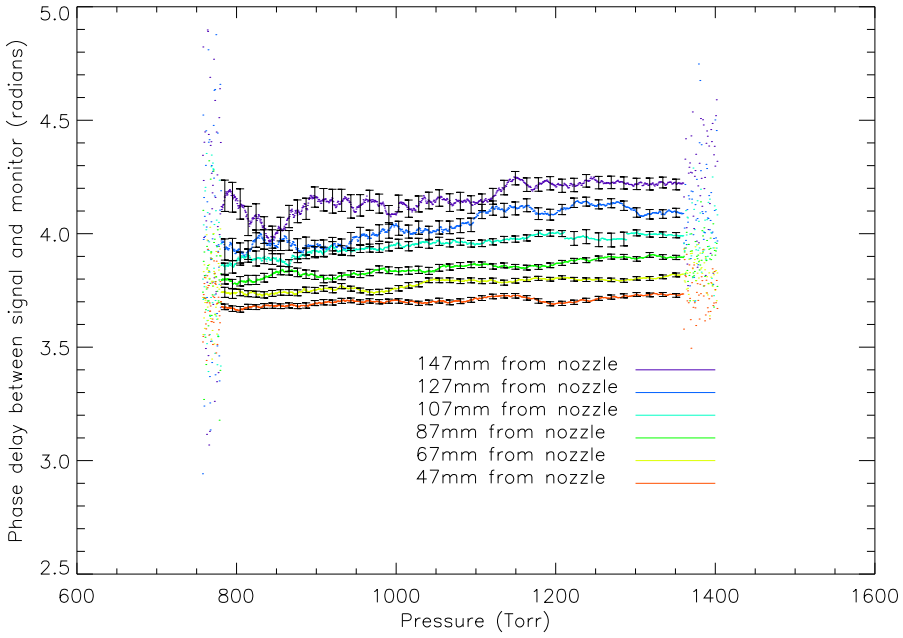


Figure 3.27: Shown is the measured phase difference by the middle-radius anemometer probe data for a range of anemometer array positions. Note the significant increase in uncertainties compared to centre-line anemometer phase difference data shown is figure 3.25.

## 3.8 Beam density

Now that the beam velocity has been measured, the flux $\Gamma(t, \theta)$ can be converted to a beam density $n(\theta, t, z)$, and this density determined for all times in the beam where $\Upsilon(t)$ data is available. $n(\theta, t, z)$ is determined by:

$$n(\theta, t, z) = \frac{\Gamma(t, \theta)}{1250 \times z^2} \tag{3.36}$$

Where z is the distance to the nozzle in metres and $n(\theta, t, z)$ has units of particles per cubic metre. The on axis beam density at the start of the analysis period for

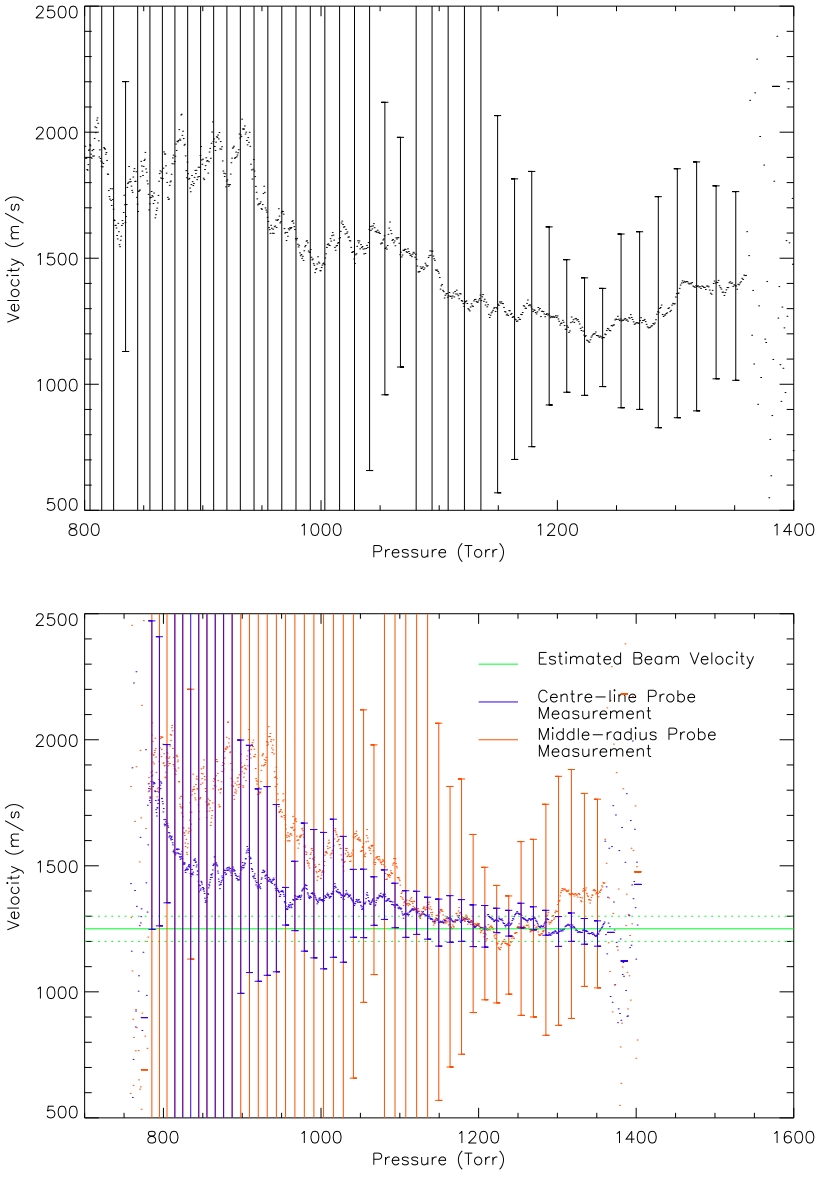


Figure 3.28: The upper plot shows the beam velocity calculated from the middle-radius anemometer probe phase difference data in figure 3.27. The error bars show the variation of the determined velocity based upon raw data in the range of phase difference values that were averaged. The lower plot shows the velocity derived from both the centre-line and middle-radius anemometer probes. The error bars for both bound the average velocity of $1250 \pm 50$ m/s determined from the centre-line anemometer probe.

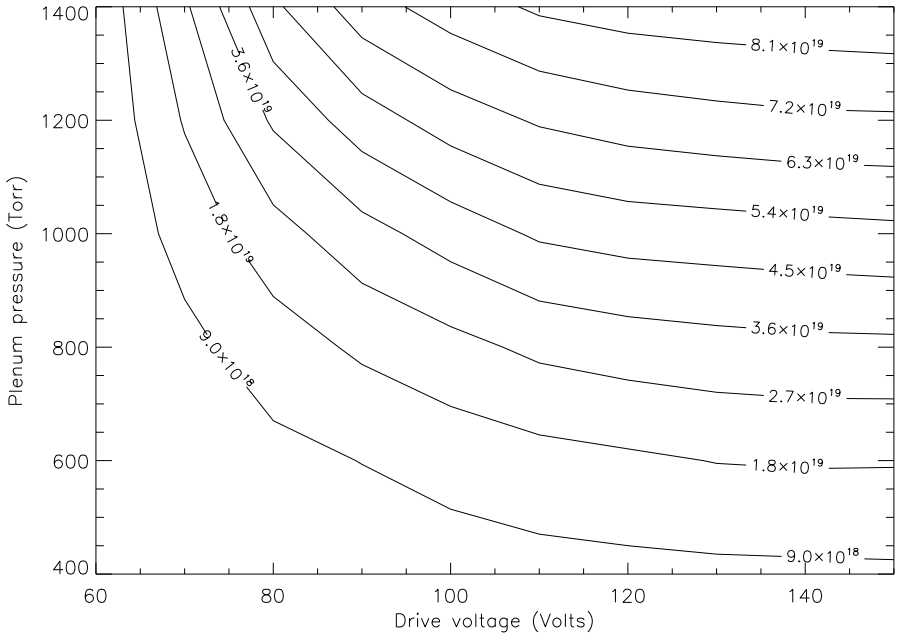


Figure 3.29: Shown is the on axis beam densities at the start of the analysis period at the approximate position of the H-1 magnetic axis (taken to be 0.240 metres from the nozzle). Only data for DC shots is presented.

available DC pulses is shown in figure 3.29. It is impractical to plot the time varying central beam densities for all times and all shot conditions characterised, so instead a set of output data files is included with this thesis. These contain the modeled hybrid fit coefficients for the range of characterised shots. Through these data files the beam properties of interest can be extracted if required. A detailed description of the output data files is included as an appendix to this thesis. By following the instructions it is possible to generate the beam densities for any beam angle, displacement from the nozzle, and characterised shot type.

# Chapter 4

# Conclusion

## 4.1 Beam source parameters

A database of test tank data has been collected and analysed to characterise the physical parameters of the diagnostic molecular beam source using helium gas. This will simplify the analysis of future data obtained from perturbative transport studies and spectroscopic analysis on the H-1 experiment.

The beam velocity was measured to be $1250 \pm 50 m/s$. The beam response to modulated signals was determined and a mechanical resonance around 1 kHz was noted. Varying piezo drive voltage as a means of molecular beam control was demonstrated and the effects determined. The diagnostic molecular beam source has been comprehensively characterised and the determined parameters readily available in included IDL .dat files to any researchers interested in utilising this unique plasma diagnostic tool.

## 4.2 H-1 installation

The diagnostic molecular beam has been installed on the H-1 experiment. Using the H-1 plenum volume determined in appendix C, the nozzle flow post installation has been cross-checked. The flow for 150 Volts DC piezo drive and a range of starting plenum pressures is shown in figure 4.1 with the theoretical flow prediction from figure 2.2 for $T_0 = 293\,\mathrm{K}$ overlaid as a trend line. The uncertainties shown for the data points are based on the uncertainty in the plenum volume only. There is an 8% difference between the measured H-1 injection rate and the injection rate measured in the test tank. In addition to this there is a leak of plenum gas into the H-1 volume. The molecular beam definitely did not leak in the test tank, so in the H-1 installation of the nozzle a leak has occurred. The origin of this leak is suspected to be the threaded region where the modified PV-10 housing is connected to the plenum used in H-1. The leak rate for helium is $3 \times 10^{16}$ particles per second for a plenum pressure of 1250 Torr (or 0.3 Torr per minute lost from the plenum). This leak should not be a problem in the operation of H-1 and may only be of concern when helium gas is used to leak check the H-1 vessel. If helium leaking from the plenum interferes with the leak detection procedures it may be necessary to flush helium from the plenum prior to leak checking.

## 4.3 First data from H-1

Using the molecular beam source in conjunction with short ECRH pulses on H-1 it was possible to resolve some of the beam's interaction with the plasma. A multi-

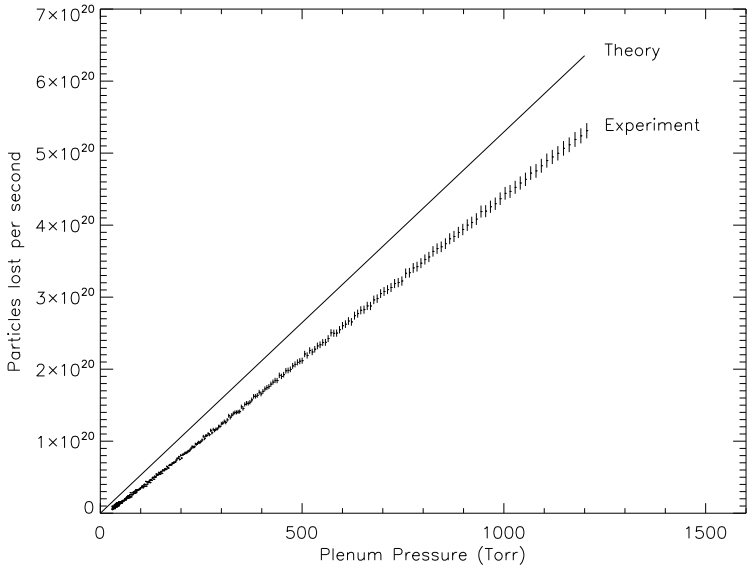


Figure 4.1: The flow for 150 Volts DC piezo drive and a range of starting plenum pressures with the molecular beam source installed on H-1 are shown as data points. Overlaid as a trend line is the theoretically predicted flow. The error bars shown as vertical lines on the data points are based on the uncertainty in the determined H-1 plenum volume.

anode array photomultiplier was used to image the plasma through a 492.2 nm filter. This measured light from a helium-neutral to helium-neutral emission line. Neither state is charged so that the magnetic field does not confine these energetic atoms. Analysis so far could not reliably determine a wave front moving through the plasma, so it was not possible to independently verify the anemometer based velocity measurements.

The $\Upsilon(t)$ series for the shot conditions (lower plot) and the light signals measured by the photomultiplier array (upper plot) are shown in figure 4.2. The interaction between the beam and the plasma is responsible for the increased light emissions. It is not a filling of the H-1 tank leaking more helium globally into the plasma as the DC component of the light signal (ie. not modulated) would increase throughout the shot. This is not observed. The upper plot presents data based upon H-1 shot numbers 59001 and 59002. Shot 59001 had no beam and was used as a background to be subtracted from the signal obtained from shot 59002 with a 5 ms pulse, 70 Volt piezo drive, and a plenum pressure of 400 Torr Helium. This shot condition has an 'a' reference (see page 105) in the characterisation database of 118. The $\Upsilon(t)$ value is shown in the lower plot. Observed light signals are clearly similar to the $\Upsilon(t)$ signal.

A video was taken of the molecular beam (with the same molecular-beam settings used to produce figure 4.2) interacting with a H-1 plasma using a Shimadzu HPV-1 high-speed video camera. The upper plot in figure 4.3 shows a CAD representation of the plasma and molecular beam to clarify the perspective of the high-speed video

data. The full movie is included in the output data files as “70V400Torr.avi” in the “highspeedvideo” directory. The stored images begin 19.9 ms after the formation of the H-1 plasma where the plasma is relatively stable. The molecular beam starts 20ms into the H-1 plasma. The timestamp on the bottom right hand frame is the time in microseconds since the first frame was recorded. A screen shot from the brightest frame in the video is shown in the lower plot of figure 4.3 to demonstrate the localisation of increased light emission in H-1. The temperature of the bright region has still not been determined precisely, however it is fair to claim that it is hotter than the surface of the sun.

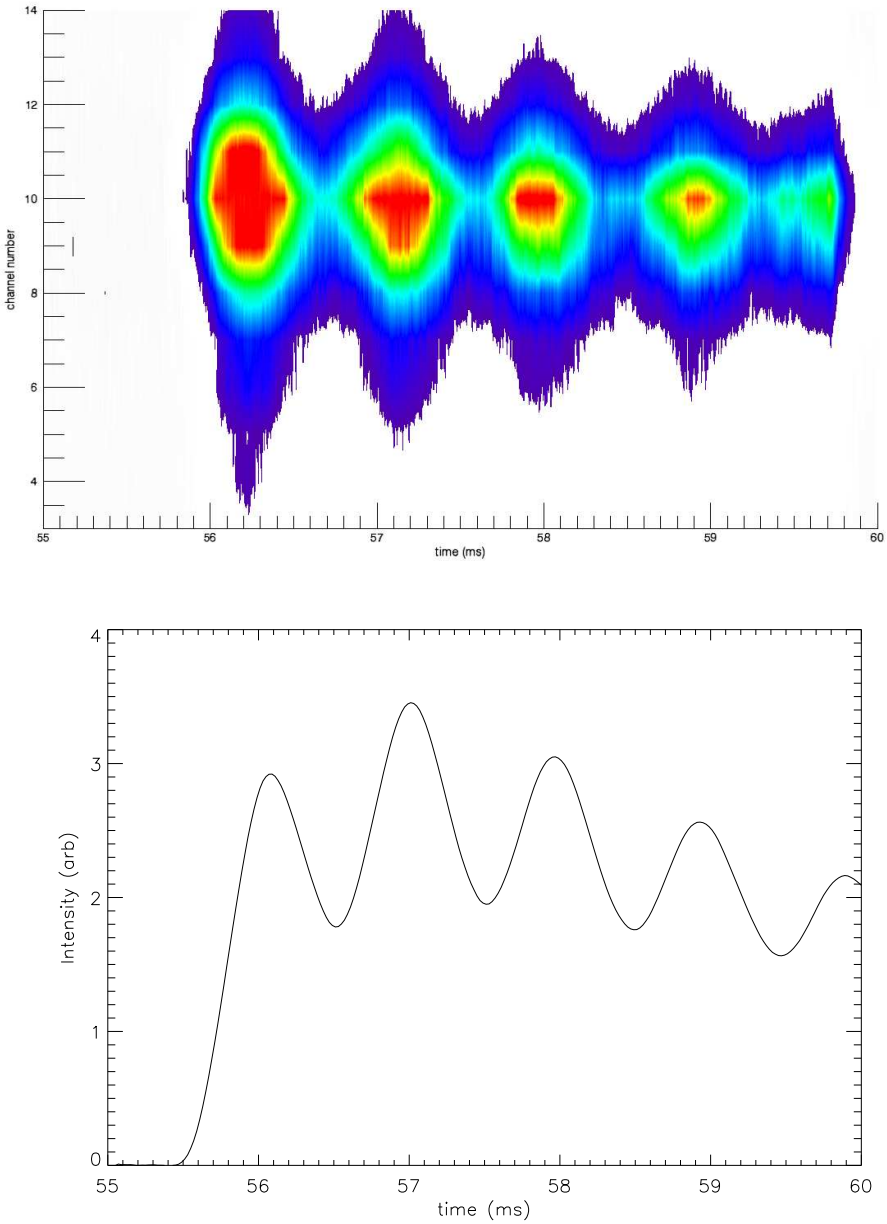


Figure 4.2: The upper plot shows the 492.2 nm neutral helium emission line intensity. The lower plot shows the corresponding $\Upsilon(t)$ signal from the output data files. The two are clearly related. Further refinement of the experiment is required to independently measure the beam velocity. On the contour the red regions represent the most intense light emission. Channel 0 is furthest from the nozzle.

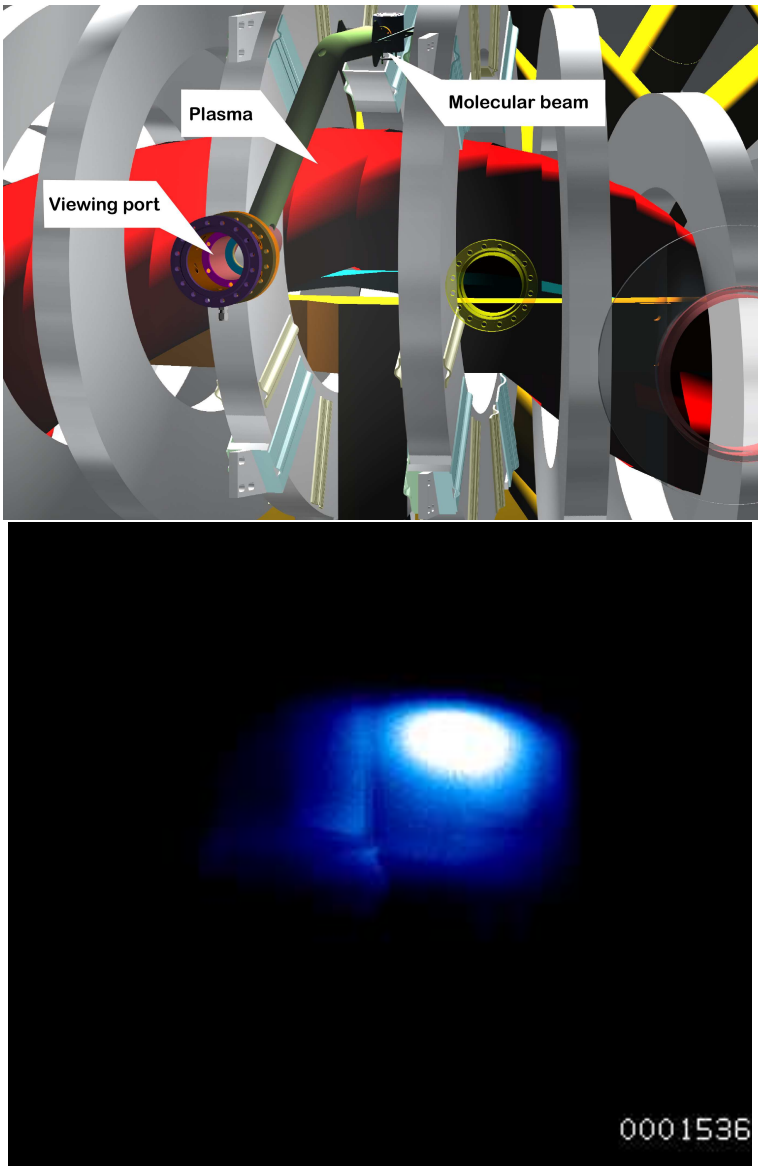


Figure 4.3: The upper image shows a CAD simulation of the experimental arrangement to give perspective to the high-speed video data. The lower image shows a screenshot from the high-speed video "70V400Torr.avi" included in the output data files. The movie clearly shows beam modulation and localised light emission from the H-1 plasma. The temperature of the modulating bright region is hotter than the surface of the sun. The colour of the lower image is a result of a colour-map conversion of the original grayscale data. The upper image is courtesy of John Wach.

# Bibliography


[1] Collis, S., Howard, J., Blackwell, B., Carlsson, P., Abelsson, M.,"A supersonic gas injection system for fuelling and probing fusion plasmas" *To be published in Plasma Sources and Technology*

[2] Soukhanovskii, V.A., Kugel, H.W., Kaita, R., Majeski, R., Roquemore, A.L. "Supersonic gas injector for fuelling and diagnostic applications on the National Spherical Torus Experiment" *Review of Scientific Instruments* **75** (p. 4320), 2004.

[3] Anderson, John D. Jr., *Modern Compressible Flow* McGraw-Hill, 1990.

[4] Krane, Kenneth S., *Introductory Nuclear Physics* Wiley, 1988.

[5] Chen, Francis F., *Introduction to plasma physics and controlled nuclear fusion. Volume 1: Plasma Physics* 2nd Edition. Plenum Press, New York, 1983.

[6] Carruthers, R., "The beginnings of fusion at Harwell" *Plasma Physics and Controlled Fusion* **30**(p. 1993), 1988.

[7] Stambaugh, R. D., "Stability, energetic particles, waves and current drive summary" *Nuclear Fusion* **45**(p. s32), 2005.

[8] Johnson, John L., "The evolution of stellarator theory at Princeton" *13th International Stellarator Workshop* 2002.

[9] Sasaki, S.,*et al.*, "Helium I line intensity ratios in a plasma for the diagnostics of fusion edge plasmas" *Review of Scientific Instruments* **67** (p. 3521), 1996.

[10] Hintz, E., Schweer, B., "Plasma Edge Diagnostics by atomic beam supported emission spectroscopy -status and perspectives" *Plasma Physics and Controlled Nuclear Fusion* **37** (p. A87), 1995.

[11] Cardoza, Lopez, "Perturbative transport studies in fusion plasmas" *Plasma Physics and Controlled Nuclear Fusion* **37** (p. 779), 1995.

[12] Hamberger, Sydney H., *et al.*, "H-1 design and construction" *Fusion Technology* **17** (p. 123), 1990.

[13] Shats, M., *et al.*, "Experimental investigation of the magnetic structure in the H-1 heliac" *Fusion Technology* **34** (p. 1653), 1994.

[14] Porkolab, M., *et al.*, "Recent progress in ICRF physics" *Plasma Physics and Controlled Fusion* **40** (p. A35), 1998.

[15] Lloyd, Brian, "Overview of ECRH experimental results" *Plasma Physics and Controlled Fusion* **40** (p. A118), 1998.

[16] Gross, D. A., Melissinos, A., "Production of a high density gas jet" *Nuclear Instruments and Methods* **130** (p. 1), 1975.

[17] Compte-Bellot, Genevieve, "Hot wire anemometry" *Annual Review of Fluid Mechanics* **8** (p. 209), 1976.

[18] Stillerman, J. A., *et al.*, "MDSplus data acquisition system" *Review of Scientific Instruments* **68** (p. 939), 1997.

[19] Vennard, John K., Street, Robert L., *Elementary Fluid Mechanics* 5th Edition. John Wiley and Sons, New York, 1976.

[20] Anderson, James B. "Molecular Beams" *Molecular beams and low density gas dynamics* Marcel Dekker inc., New York, 1974.

[21] Kirkup, Les *Experimental Methods* John Wiley and Sons, 1994.

[22] Halliday,D., Resnick, R., Walker, J. *Fundamentals of Physics* 4th edition(extended) Wiley, New York, 1993.

[23] Bondi, A., "van der Waals Volumes and Radii" *The Journal of Physical Chemistry* **68** (p. 441), 1964.

[24] Liepmann, Hans W., Roshko, A. *Elements of Gasdynamics* Dover, New York, 2002.

[25] Spina, E. F., McGingley, C. B., "Constant-temperature anemometry in hypersonic flow: critical issues and sample results" *Experiments in Fluids* **17** (p. 365), 1994.

[26] Ower, E., Pankhurst, R. C., *The Measurement of Air Flow* 3rd ed., Pergamon Press, Oxford, 1966.

# Appendix A

# Output data files

The perturbation of the plasma by the diagnostic molecular beam must be minor if diagnostic use is intended. In order to aid data analysis of small plasma perturbations, a condensed database of characterisation data has been provided. This allows correlation between the plasma perturbations and the molecular beam to be used in analysis of signals. This appendix catalogues the format of the output data files so that the analysis of experiments involving the diagnostic molecular beam source have accurate injection source terms available.

The beam properties are known for plenum pressures of 400, 600, 800, 1000, 1200 and 1400 Torr. At each of these pressures the molecular beam source's response to modulated and DC piezo drive voltages were recorded. DC driven shots have been characterised for 60, 70, 80, 90, 100, 110, 120, 130, 140, and 150 Volts piezo drive. The modulated shots had 120 Volts peak drive, and were modulated to a minimum of 85 volts in a sinusoid. This was the only modulation drive amplitude characterised. Unfortunately the phase of the modulation was not optimised. The phase of the drive voltage is out of phase with the ringing response of the valve. The

modulation frequencies characterised were 100, 200, 300,400, 500, 600, 700, 800, 900, 1000, 1100, and 1200 Hertz.

For each of these conditions, $\Upsilon(t)$ values and the corresponding piezo drive monitor signal are available for 100ms pulses. These values are stored in the 'upsilonref.dat' data file. The values of the hybrid fit coefficients, the on axis hybrid fit value, the angle where the beam density is half the on axis value, and the angle integral of the hybrid fit profile are available in the 'fullhybrid.dat' data file.

The shots are ordered by a shot reference number 'a' determining the shot conditions desired. To find the required 'a' value, select the desired conditions from the conditions characterised. For DC shots 'a' is found by:

$$a = (1400 - press) * 0.11 + (150 - volt) * 0.1 \tag{A.1}$$

For modulated shots 'a' is found by:

$$a = (1400 - press) * 0.11 + 10 + (modf - 100) * 0.01 \tag{A.2}$$

where press is the plenum pressure in Torr, volt is the max piezo drive in Volts, and modf is the frequency. Take care to select only characterised shot conditions. To demonstrate the calculation of 'a' value, two examples are provided: DC drive and modulated drive. Example 1; the shot with 1200 Torr plenum pressure and 70 Volts drive and 0 Hz modulation would have an 'a' value of 30. Example 2; the shot with 400 Torr plenum pressure, 120 Volts drive, and 600Hz modulation shot has an 'a' value of 125.

'upsilonref.dat' when restored in IDL defines the array upsilonref. The size of upsilon ref is [0:131,0:1,0:6000] where the first index is the 'a' value. The second index is 0 for $\Upsilon(t)$ values, and 1 for the piezo drive monitor signal. The third index is time, where 0 is the monitor reference point, and the position n represents the time position $2n \times 10^{-5}$ seconds into the shot.

'fullhybrid.dat' when restored in IDL defines the array fullhybrid. The size of the array is [0:131,0:8,0:5100] where the first and last index are the same as for upsilonref.dat. The second index contains a variety of values associated with the fitted hybrid profile: 0 gives the $A_g$ coefficients, 1 gives the $\theta_g$ coefficients, 2 gives the $A_l$ coefficients, 3 gives the $\theta_l$ coefficients, 4 gives the angle integral of the profiles, 5 gives the angles from the axis where the profile value is half the on axis value, 6 gives the on axis profile value, 7 gives the piezo drive monitor signal, and 8 gives the absolute error of the values. The constant $\alpha$ has not been included in these files. The profile integral includes the $2\pi$ factor.

For example, these output data files can determine the time resolved flow of particles from the plenum for 1000 Torr, 120 volt drive, modulated at 900 Hz. The 'a' value in this case will be 62. The syntax required to generate the desired data in IDL is:

IDL/ **restore, 'fullhybrid.dat'**

IDL/ **time=findgen(5101)*2e-5**

IDL/ **alpha=9.663e17**

IDL/ **plot, time, alpha*fullhybrid[62,4,*], xtitle='time(seconds)', ytitle='Particles per second'**

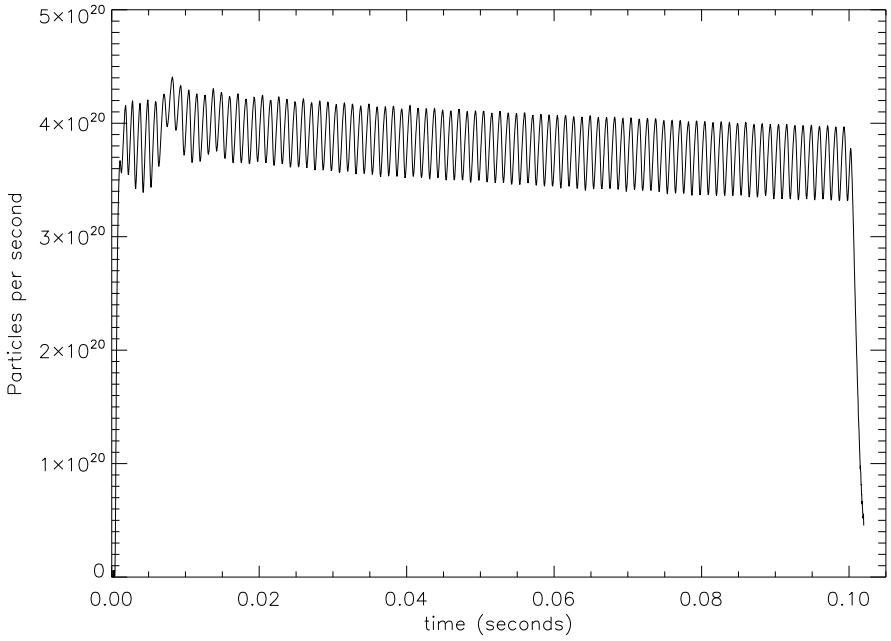


Figure A.1: Shown is a plot of the plenum particle loss rate generated by interrogating the fullhybrid array.

This will generate a plot of the time resolved plenum particle loss rate from the plenum, shown in figure A.1.

# Appendix B

# DISH system instructions

DISH is the name of the molecular beam source on H-1. A copy of these instructions are located on the desktop of PRL96 called "dishinstructions.doc". The two Labview *.vi's located on the desktop of PRL96 control the DISH system. DISH.vi runs automatically from start up and connects to the spectroscopy database on PRLAS2. DISHlocal.vi connects to the BEN database situated on PRL96 and allows the system to be run independently of the H-1 data system.

## B.1 Quick start

1.Reboot PRL96

2.Log in as administrator, password: *******

The system will now automatically operate in accordance with settings in the spectroscopy model shot.

## B.2 VNC connection

Remote connection to the desktop can be made via VNC. The address for the session is vnc:/prl96:0, password: *******

## B.3 Description of operation

The system will automatically connect to the H-1 spectroscopy database and load values from the model shot into the DISHSETTINGS cluster. The H-1 MDSplus dish data structure is shown in table B.1. Three basic modes of operation are possible based on the settings in the model shot. The three modes are:

**1. System in Manual mode.** The system is manually controlled. Without manual input commands to the .vi front panel the system is idle. Manual mode is initiated by placing any value other than True in the :AUTO node.

**2. System is in Auto collecting null shot data.** When the :AUTO node contains the value True, and :PULSEMAX is set to zero, the system will record start and end plenum pressures without the beam operating. This detects systematic errors in the system, such as magnetic induction as the H-1 magnetic field is turned on and off. Attempts have been made to reduce the effects of these errors, however the perturbations are still clearly visible on the plenum pressure chart around the time a shot fires. By establishing null shot errors for a particular configuration these systematic errors can be determined and considered.

**3. System is in Auto collecting experiment data.** When the system is in auto mode and the :PULSEMAX node contains a non zero value for maximum drive voltage (large enough to open the valve) the molecular beam injects into H-1.

| | | |
|---|---|---|
| :AMPGAIN | :AUTO | :COMMENT |
| :DELTAPRESS | :FLUXRATE | :MODDEPTH |
| :MODFREQ | :MONFACTOR | :PLENUMEND |
| :PLENUMPRESS | :PLENUMSTART | :PLENUMVOLUME |
| :POSTTRIGDLY | :PULSELENGTH | :PULSEMAX |
| :SAMPLERATE | :SHOTNUMBER | :TOTALFLUX |

Table B.1: List of nodes for **SPECTROSCOPY::TOP.DISH**

At the end of a shot, the node :DELTAPRESS holds plenum pressure change datum. TOTALFLUX holds the total number of neutral particles injected during the pulse. :FLUXRATE holds the neutral particle injection rate per second. These values are automatically saved in the auto mode. Once saving is complete in the auto mode the system gives an audible cue to indicate correct operation. This function can be disabled on the front panel of the vi by selecting the 'fart on' option to false. For this setting to be remembered at start up it must be saved as the new default value for this control. The :PLENUMVOLUME value is used to convert plenum pressure changes to particle flow measurements. Particle measurements are only calibrated if Helium is used in the plenum.

## B.4 Description of the nodes

The **SPECTROSCOPY::TOP.DISH** nodes can be grouped into two basic types: control nodes, and data nodes. A full description of each dish node follows.

### B.4.1 Control nodes

**AMPGAIN** (numeric) Amplifier gain. If the amplifier gain is changed this field needs to be modified. If AMPGAIN is not set correctly the piezo drive voltage will differ from the selected value.

**AUTO** (boolean) System mode. When set to True, the system is in automatic mode. That is, it arms, triggers, and saves data without the need for user input. When set to False, the system is in manual mode. In manual mode the system still uses the model shot to establish the DISHSETTINGS parameters.

**COMMENT** (string) Dish specific shot comment.

**MODDEPTH** (numeric) The percentage of maximum voltage used as a minimum piezo drive voltage in modulated beam experiments. The characterisation was performed at 30%.

**MODFREQ** (numeric) The modulation frequency used to modulate the drive voltage in Hertz.

**MONFACTOR** (numeric) The factor by which piezo amplifiers internal resistor network reduces the high voltage output for the monitor channel data recorded in the **.OPERATIONS:PUFF_135** node of the H-1 data structure.

**PLENUMPRESS** (numeric) The target plenum pressure for the shot. Due to hysteresis in the control of the plenum pressure, the system approaches the target pressure but does not exactly match it. If plenumpress is reduced between shots the system will bleed plenum gas into H-1. Scans of increasing pressure avoid this problem.

**PLENUMVOLUME** (numeric) The volume of the plenum and plumbing between the pneumatic valve outlet port, and the piezo valve.

**POSTTRIGDLY** (numeric) The time in milliseconds after the H-1 trigger the system waits before injecting particles.

**PULSELENGTH** (numeric) The duration in milliseconds of the pulse.

**PULSEMAX** (numeric) The maximum drive voltage to be applied to the piezo valve during the pulse. Excessive voltages may damage the valve. The suggested maximum is 150 Volts.

**SAMPLERATE** (numeric) The sample rate of the piezo drive voltage waveform in samples per second. 50000 is the recommended value.

### B.4.2 Data nodes

**DELTAPRESS** (numeric) The measured change of the plenum pressure over the shot in Torr.

**FLUXRATE** (numeric) The neutral particles injected per second during the pulse for helium.

**PLENUMEND** (numeric) The plenum pressure measured after the pulse in Torr.

**PLENUMSTART** (numeric) The plenum pressure measured before the pulse in Torr.

**TOTALFLUX** (numeric) The total number of particles injected during the shot for helium.

## B.5 The DISH.vi front panel

In addition to the DISHSETTINGS linked to the H-1 database there are controls that are only accessible from the DISH.vi's front panel. These can be considered to be advanced options. A brief description of these follows. For a comprehensive understanding of these controls it is recommended that the user familiarise themselves with the DISH.vi's wiring diagram.

**ABORT** (event) The system is disarmed and returned to standby. If the system is in auto mode it will re-arm.

**ARM** (event) The system is armed if currently in standby.

**INITIALISE** (event) The system is disconnected and then reconnected the the control database.

**STOP** (event) The system is stopped such that upon running it will re-initialize

**MDSCONNECT** (event) The system will attempt to MDSConnect to a remote MDSplus SERVER. If the connection is successful the MDSCONNECTED indicator will show true.

**MDSDISCONNECT** (event) The system will disconnect from the remote MDSplus server.

**CHANGE PLENUM** (event) The system has a single attempt at acquiring the plenum pressure set in the PLENUMPRESS setting.

**READ SHOT NUMBER** (setting) the desired shot to be manually displayed in the DISH DATA fields.

**READ** (event) If the system is in standby the READ SHOT NUMBER shot is loaded into the DISH DATA fields.

**WRITE SHOT NUMBER** (setting) the desired shot to manually write the cur-

rent settings and data to.

**WRITE** (event) If the system is in standby the WRITE SHOT NUMBER shot is written to. The remote access features of the H-1 data structure prevent the creation of new shots remotely.

**CURRENT SHOT** (indicator) displays the current shot returned from the database.

**UPDATE** (event) Updates the current shot data.

**NEXTSHOT** (indicator) applicable to auto mode and is controlled by the system.

**PLENUM FACTOR** (indicator) A pressure update weighting that reflects the accuracy of the pressure readings. Small values represent stable measurements and large values (approaching 1) indicate the reading is varying.

**SERVER** (setting) The server the system connects to when initialised or when a MDSCONNECT event occurs.

**DATABASE** (setting) The name of the database the system attempts to read and write to.

**UPDATERATE** (redundant)... I think! Set it to the same as **SAMPLERATE** just to be careful!

**CONTROL SHOT** (settting) The shot number to be used to load settings from. The default is -1, the model shot.

**LOCK COUNT** (indicator) This feature accounts for the slow time response of the plenum pressure gauge. In the post pulse phase of the shot the system does not record the final pressure until 3 consecutive pressure measurements are within a tolerance set internally in the DISH.vi. Lock count indicates the number of consecutively matching measurements. If for some reason the system fails to complete a pulse and hangs in the post pulse stage then it is likely to be a result of the system

failing to lock in a post pulse plenum pressure.

**LOCK SAFE** A failsafe for the plenum pressure measuring algorithm. Once the value reaches a threshold set internally in the DISH.vi the post pulse pressure is recorded without the LOCK COUNT criteria being satisfied. This feature was added as the slow leak from the plenum into H-1 prevented the system locking to a constant plenum pressure after shots with high plenum pressures.

**POLLCOUNT** (indicator) This value increments each time the system measures the plenum pressure. Once the value is larger than the POLLMODULO value, the count is reset and the database is interrogated to see if any settings have changed.

**POLLMODULO** (setting) The number of pressure measurements between database interrogations.

**PALPHA** (setting) A constant that relates to the plenum pressure surge during filling resulting from of the dead space between the needle valve and the pneumatic valve. This parameter approximates the 'instant' increase in plenum pressure that results from the fill valve opening.

**PS** (setting) A constant that relates to the source head pressure feeding into the needle valve.

**RNEED** (setting) A constant that relates to the flow rate through the needle valve. If the needle valve position is changed this value must be modified.

**RNOZZ** (setting) A constant that relates to the flow rate through the DISH jet during a plenum bleed. Changing the nozzle diameter or the bleed voltage will require this setting to be changed.

**FART ON** (toggle) Turns the audible confirmation in auto mode on and off.

**CHART ON** (toggle) Turns the plenum pressure chart on and off. Useful to speed

up VNC connections.

**PLENUM START HOLD[1,2,3]** A data delay line to reduce errors from magnetic induction when the H-1 magnetic field turns on. The induced voltage generates spurious pressure signals. A band aid solution.

**DISHDATA** (cluster) Indicates stored shot data after a manual read. During a shot this cluster indicates data as it is sequentially collected and at times may hold data from previous shots. A read command should be executed in standby to ensure all values relate to the shot in question.

**STATUS** (cluster) Indicates the current state of the system. When the vi is running this cannot be used to control the system. Instead try using elements in the CONTROL cluster.

**DISHSETTINGS** (cluster) Modifying any value in this cluster writes the entire cluster to the database. The cluster value is then read back from the database so that the indicated values are a representation of the values in the database. If the system is not connected to a database, an error is reported in the comment field.

# Appendix C

# Measuring the H-1 DISH plenum volume

The effective plenum volume on H-1 had not been accurately measured. Only estimates were available of the volume of the plumbing connecting the internal (inside the H-1 vacuum tank) plenum volume to the external (outside the H-1 vacuum tank) plenum filling hardware. The same software used to conduct experiment scans in the test tank was used to conduct an automated experiment on H-1. To measure the volume of the H-1 plenum $V_1$, 360 shots of 100ms duration with 150 Volt DC drive were performed without filling the plenum between shots. This series gave the values of $\Delta P_1$, the measured pressure change without the test volume installed. A known test-volume ($V_t$) was then added externally to the plenum volume, and a series of 500 shots performed as before. The second series gave values of $\Delta P_2$, the measured pressure change with the test-volume installed. $\Delta P_1$ and $\Delta P_2$ values were then selected so the average plenum pressure in each case was the same. Linear interpolation between recorded $\Delta P_2$ values allowed the average plenum pressures to be matched. The molecular beam source flow is linearly dependent on plenum pressure. By referencing the data to the average plenum pressure errors due to the

linear change in plenum pressure are removed from the volume calculation. The change in pressure for shots with the same piezo drive and average plenum pressure with and without the test volume installed allows the plenum volume without the test-volume to be estimated by:

$$V_1 = \frac{V_t}{\frac{\Delta P_1}{\Delta P_2} - 1} \tag{C.1}$$

$V_t$ was determined by using a 10mL syringe to inject ethanol into the test-volume. Each syringe measurement was considered to have an uncertainty of 0.1mL. The volume of ethanol required to fill the test volume was then 83.3mL ± 1mL.

A plot of $V_1$ verses plenum starting pressure is shown in figure C.1. Note that with low plenum pressures noise contaminates the measurement. To avoid this noise the volume calculation only involved measurements where the start plenum pressure exceeded 800 Torr. The error shown is based solely on the uncertainty in the plotted data in this range. Combining this uncertainty with that established for $V_t$ gives an absolute uncertainty around 2%. The H-1 effective plenum volume is then 123.9 ± 2.5 mL.

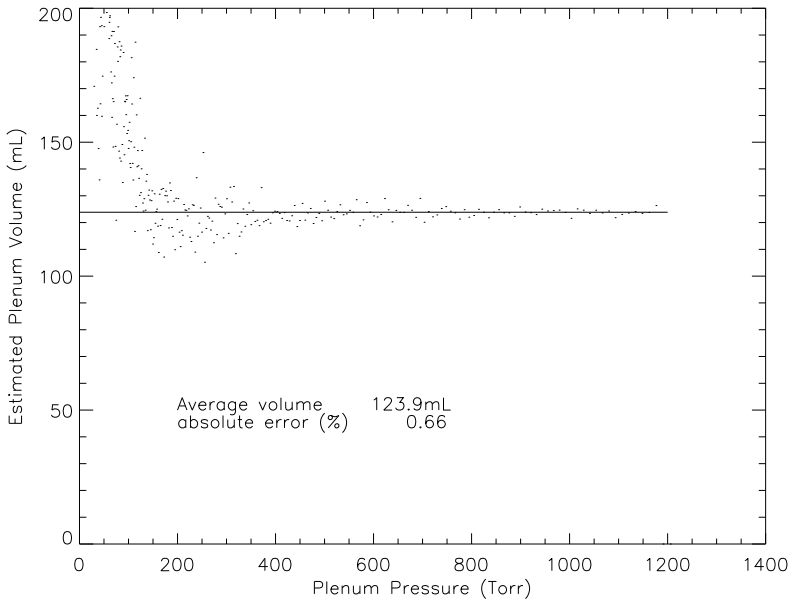


Figure C.1: Shown is a plot of the estimated plenum volume $V_1$ verses starting plenum pressure. The plenum volume estimation only included data for plenum pressures exceeding 800 Torr. The uncertainty shown does not include the uncertainty in the test-volume measurement.